Determining Brain Mechanical Properties and Presenting a New Computational Paradigm for Post-traumatic Cerebral Edema

Andrew Phillip Vasco Basilio

Submitted in partial fulfillment of the
requirements for the degree of
Doctor of Philosophy
under the Executive Committee
of the Graduate School of Arts and Sciences

COLUMBIA UNIVERSITY

2023

Abstract

Determining Brain Mechanical Properties and Presenting a New Computational Paradigm for Post-traumatic Cerebral Edema

Andrew Phillip Vasco Basilio

Traumatic brain injury (TBI) is a major problem with an estimated cost of $76 billion per year in the US alone. The Center for Disease Control and Prevention (CDC) documented 2.53 million TBI-related emergency department visits, with approximately 288,000 TBI-related hospitalizations and 56,800 TBI-related deaths in 2014 in the US. The lack of FDA-approved treatment strategies for TBI drives the need for novel therapeutic and preventative measures.

In a quest to reduce TBI-related injuries and deaths, automotive companies have focused their efforts to make safer cars for both occupants and pedestrians. Computational finite element (FE) models have been used to advance research efforts in automotive safety systems engineering in hopes of ameliorating the burden caused by TBI. The current use of FE models in the automotive industry focuses on predicting stresses and strains that occur during the accident itself to predict primary injury. However, contemporary models lack the appropriate mechanical properties required to make accurate predictions of brain tissue deformation after injury and lack the ability to model secondary injuries such as cerebral edema (brain swelling). With cerebral edema being a major cause of death and disability after TBI, and with the pattern and magnitude of cerebral edema being dependent on the initiating strain field in brain tissue during TBI, automotive safety systems could be further improved if 1) FE head models contained more accurate mechanical properties and 2) if FE models could simulate secondary injuries such as cerebral edema. Therefore, the driving purpose of this thesis is two-fold: 1) to determine the

mechanical properties of different regions of the brain and 2) to present a new computational methodology that allows for modeling of cerebral edema to better predict patient outcome following TBI.

The use of FE models requires appropriate constitutive formulations and associated parameters to accurately model and predict the initial mechanical response of the brain to injury loading conditions. Since patient outcome is dependent on the resulting strain field within brain tissue post-injury, accurate modeling of brain tissue deformation is important for testing the efficacy of engineered automotive safety systems using FE simulations. To address this need, the first aim of this thesis employed an inverse FE approach to characterize mechanical properties of the human hippocampus (CA1, CA3, dentate gyrus), cortex white matter, and cortex gray matter. Anatomical regions were significantly different in their mechanical properties. Although no sex dependency was observed, there were trends indicating that some male brain regions were generally stiffer than corresponding female regions. In addition, mechanical properties were not dependent on age within the examined age range (4-58 years old). Ultimately, this study provides a structure-specific description of fresh human brain tissue mechanical properties, which will be an important step toward explicitly modeling the heterogeneity of brain tissue deformation during TBI using FE modeling.

Fatal brain injuries may also result from physiological changes in the brain that occur after the primary injury that immediately occurs during head injury. Secondary injuries such as cerebral edema are associated with poor outcome. Despite the severe consequences of cerebral edema, its mechanism is not fully understood. The second aim of this thesis, therefore, was to elucidate the driving mechanism of cerebral edema by demonstrating that cleavage of intracellular fixed-charge density (FCD) reduces brain swelling pressure and to measure the FCD

content of rat and pig brain tissue. Thin brain samples were placed into a confined pressure chamber, and FCD content was calculated from measured swelling pressure and the Gibbs-Donnan equation. We observed that cleavage of FCD using enzymes reduced swelling pressure in rat brain tissue samples and determined that pig cortex gray matter contains more FCD than pig cortex white matter. These results demonstrate that cerebral edema may occur in accordance with principles of triphasic swelling biomechanics and demonstrates the plausibility of computationally modeling cerebral edema with triphasic material formulations.

Cerebral edema leads to increased intracranial pressure (ICP) as the brain swells within the fixed volume of the skull, and there is overwhelming evidence of ICP as a powerful predictor of patient outcome following TBI. Current industry standards of patient outcome evaluation use tissue-level metrics solely from primary injury such as maximum principal strain (MPS) or cumulative strain damage measure (CSDM), but these methods can be improved especially in regards to predicting mortality. Therefore, the third aim of this thesis was to develop a new FE head model and computational methodology incorporating triphasic swelling biomechanics to simulate brain swelling following impact to improve patient outcome predictions. Patient outcome was predicted by simulating swelling and calculating the resulting ICP, which is a strong indicator of patient mortality. Calculating ICP in addition to predicting primary injury metrics such as MPS and CSDM may allow automotive safety engineers to make better predictions of patient outcome following TBI so they can develop better safety systems.

Another common indicator of poor outcome following TBI is acute subdural hematoma (ASDH). ASDH is an intracranial bleed that often results from TBI because of stretching and tearing of the bridging veins which causes blood to collect in the innermost layer of the dura. Despite the poor prognosis associated with the presence of ASDH following TBI, the mechanism

as to why its presence is associated with a higher likelihood of death remains uncertain. Current state of the art FE head models used in automotive safety engineering efforts do not consider ASDH, which may drastically reduce their effectiveness in predicting patient outcome following TBI. Therefore, the fourth and final aim of this thesis was to incorporate ASDH into our FE head model of swelling and elucidate the underlying secondary brain injury mechanism of ASDH that contributes to increased mortality in hopes of increasing the efficacy of current FE models to predict patient outcome and ultimately design better safety systems. Using our novel FE head model and methodology from aim 3, we showed that the higher likelihood of death associated with the presence of ASDH may be caused by exacerbated ischemic injury which increases ICP, demonstrating that modeling of ASDH is necessary for accurately modeling patient outcome following TBI.

Despite decades of TBI research and FE head model improvements, more work is required to enhance the biofidelity of these models to better predict patient outcome. The work in this thesis is important, as it introduces a new tool that will allow automotive safety engineers to incorporate cerebral edema and ASDH, both of which may drastically influence patient outcome following TBI, into models of head injury to allow for better predictions of patient outcome. It is hoped that the work in this thesis lays the foundation for future work that aids in the design of improved automotive safety systems that will save countless human lives.

Table of Contents

List of Figures

List of Tables

List of Abbreviations

Abbreviation	Full Name
2DG	2-deoxyglucose
aCSF	Artificial cerebrospinal fluid
AIS	Abbreviated injury scale
ANOVA	Analysis of variance
ASDH	Acute subdural hematoma
ATP	Adenosine triphosphate
BBB	Blood-brain barrier
CA1	Cornu Ammonis 1
CA3	Cornu Ammonis 3
CDC	Center for Disease Control and Prevention
CIBIC	Convolution of impulse response for brain injury criterion
CIREN	Crash Injury Research and Engineering Network
CSDM	Cumulative strain damage measure
CSF	Cerebrospinal fluid
CT	Computerized tomography
CTE	Chronic traumatic encephalopathy
CtxG	Cortex gray matter
CtxW	Cortex white matter
DAI	Diffuse axonal injury
DG	Dentate gyrus
DMMB	1,9 dimethylmethylene blue
DNA	Deoxyribonucleic acid
ED	Emergency department
FCD	Fixed charge density
FE	Finite element
GAG	Glycosaminoglycan
GCS	Glasgow coma scale
GHBMC	Global Human Body Models Consortium
ICP	Intracranial pressure
MAIS	Maximum abbreviated injury scale
MPS	Maximum principal strain
MVC	Motor vehicle crash
Na^+/K^+	Sodium-potassium
NASS-CDS	National Automotive Sampling System – Crashworthiness Data System
NASS-PCDS	National Automotive Sampling System – Pedestrian Crash Data Study
QLV	Quasilinear viscoelastic
RMSE	Root mean square error
SEM	Standard error of the mean
SSE	Sum of squared error
TBI	Traumatic brain injury

Acknowledgments

I would like to acknowledge my advisor, Dr. Barclay Morrison III, for giving me the opportunity to conduct interesting cutting-edge research in his laboratory and whose work ethic, mentorship, and scientific guidance have inspired me to improve as a researcher, scientist, and engineer. I would like to acknowledge former members of the Neurotrauma and Repair Laboratory, Dr. Sowmya Sundaresh and Dr. Nevin Varghese, for introducing me to the laboratory, teaching me laboratory techniques unique to this lab, brainstorming new ideas with me, being a source of inspiration during difficult times, and providing guidance and mentorship over the past several years. I would like to acknowledge current members of the laboratory, Mary Kate Dwyer, Carolyn Kim, and Ehsan Alipourjeddi for their companionship, support, and helpful discussions over the past several years. I would like to acknowledge the undergraduate students that I mentored, Leanne Pichay and Olivia Hansen, for assisting me with hardware design, coding, and endless troubleshooting. I would like to acknowledge the graduate student I mentored and incoming PhD student in the lab, Delin (Stevie) Zeng, for assisting me greatly in everything during the last 1.5 years and for going above and beyond what I asked for. He is truly one of the best people I have ever worked with. I would like to acknowledge Dr. Gerard Ateshian of the Musculoskeletal Biomechanics Laboratory (MBL) at Columbia University and Dr. Steve Maas at the University of Utah for assisting me extensively with FEBio, helping me with extensive troubleshooting efforts, and for helpful discussions. I would also like to acknowledge previous and current members of the MBL for assisting me with my work as well. I would like to acknowledge the veterinarians at Columbia University, especially Alexander Romanov and Ellen Gunzel, as well as the veterinarian technicians for assisting with pig brain isolation procedures. I would like to acknowledge Joe Viola for being an excellent lab manager

and assisting with troubleshooting and procedures. I would like to acknowledge Tanya Tabachnik and Chaim Sallah for assisting with device designs and machining. I would like to acknowledge Steve Kernie for allowing us to use his lab space for pig brain procedures, and I would also like to acknowledge Abdu Abushaban and Ningning Guo, two members of Steve's lab, for introducing me to the lab, for their companionship, and for enjoyable talks during lunch break. I would like to also acknowledge the funding sources that made this work possible: Honda Motor Co., Ltd. and a grant from the Paul Allen Family Foundation. I would like to acknowledge the shared computing resources at Columbia University for assisting greatly with computational simulations. I would also like to acknowledge my friends from middle school, high school, college, and those I have met along the way during my time at Columbia University for their friendship. Finally, I would like to acknowledge my entire family, especially my parents, Dr. Ralph Basilio and Eleanor Basilio, for their constant support, prayers, encouragement, and inspiration throughout this difficult yet rewarding journey.

Chapter 1: Introduction

Traumatic brain injury (TBI) is the leading cause of death in disability in young people [1]. TBI is defined as either blunt or penetrating injury to the head that causes alterations in brain function [2]. From 1995 to 2001 in the United States alone, there were on average 1.4 million TBIs and about 80,000-90,000 people experiencing permanent disability from TBI every year [3]. In 2013, there were approximately 2.5 million TBI-related emergency department visits, approximately 282,000 TBI-related hospitalizations, and approximately 56,000 TBI-related deaths in the United States [4]. TBI costs are burdensome and generally high, with in-hospital treatment of patients with TBI ranging from $2,100 to $400,000 per patient [5]. According to the Center for Disease Control and Prevention (CDC), the estimated direct and indirect cost of TBI in 1995 was $56.3 billion, surpassing the cost of spinal cord injury and AIDS [6], and the average lifetime cost per survivor of TBI requiring hospitalization was $111,578, with the average cost per fatality being $454,717 [7]. Because of the widespread detrimental impact of TBI, much research has been conducted in an effort to ameliorate the consequences of TBI or to prevent the onset of TBI altogether. Unfortunately, all clinical trials in TBI have failed. Therefore, prevention remains the most important way to reduce the societal costs of TBI. Development of a computational FE head model that accurately predicts patient outcome following TBI and allows for testing of different automotive safety systems within a computational environment could facilitate the speedy development of efficacious safety systems in vehicles.

FE head models have been used in automotive safety engineering efforts to predict patient outcome after accidents, and accurate predictions require accurate mechanical properties

that dictate brain deformation during an accident. However, these FE head models may not contain appropriate mechanical properties, which would lead to inaccurate predictions of brain deformation. Therefore, the first goal of this thesis was to determine the mechanical properties of different regions of human brain tissue. Additionally, current FE head models used in the automotive industry predict patient outcome by solely assessing primary injury metrics such as stress and strain during the impact itself. However, secondary injuries such as cerebral edema (brain swelling) which occur after the injury itself may also greatly influence patient outcome. Therefore, the second goal of this thesis was to create a new computational methodology to simulate cerebral edema in FE models to allow for better predictions of patient outcome after TBI.

We modeled cerebral edema under the premise of a hypothesized mechanism that includes the cellular structures of the brain and the Gibbs-Donnan effect, which will be described in detail later. Brain tissue is composed of approximately 80% water and 20% solid matrix. The solid matrix inside cells consists of negatively charged materials (proteins, glycosaminoglycans, DNA, etc.), represented by the concept of a fixed charge density (FCD). The intracellular and extracellular space are separated by the plasma membrane and embedded within that plasma membrane are sodium-potassium (Na^+/K^+) pumps that use energy to remove net positive charges from the inside of the cell, which maintains a negative transmembrane potential. Under normal resting conditions, we hypothesize that the FCD is under-hydrated because of this charge imbalance, which has major implications for brain swelling after mechanical insult to the plasma membrane or failure of adequate Na^+/K^+ pump activity during ischemic injury.

The FE head model presented in this thesis was a finite element mesh created using FEBio (febio.org) based on the industry standard Global Human Body Models Consortium

(GHBMC) finite element model. Nodal displacements predicted from impact scenarios using the GHBMC model served as inputs to the swelling model implemented in FEBio to simulate the resulting post-traumatic cerebral swelling based upon the nodal displacements (primary injury) followed by secondary injury (ischemic tissue death). Maximum principal strain (MPS) for each element was related to damage (cell death) and damage was related to exposed FCD. Ischemic damage and its effects on brain swelling were also taken into account by relating compressed volume ratio for each element to damage (cell death), which was then related to exposed FCD. Using the results and methodology highlighted in this work, researchers and automotive safety engineers may be able to more accurately predict patient outcome following an automotive accident, providing an opportunity to better engineer TBI preventative measures and automotive safety systems during the research and development phase.

1.1 Biomechanical Modeling of Brain Tissue

Patients who experience TBI report a variety of symptoms such as depression, irritability, anxiety-related disorders, headaches, dizziness, loss of consciousness, and other cognitive dysfunctions [8]. In even more severe cases, TBI can lead to neurodegeneration, Parkinson's disease, Alzheimer's disease, motor neuron disease, and chronic traumatic encephalopathy (CTE) [9]. Damage to a particular part of the brain can lead to disruption of the normal function for which that part of the brain is responsible. This damage is due to deformations of the brain tissue, which can lead to certain pathologies such as diffuse axonal injury (DAI) in the white matter of the brain [9]. FE computational models have been used for many decades to predict brain tissue deformation and mechanical behavior during the impact event. Because the strain field of brain tissue during TBI depends on the mechanical properties of each part of the brain,

incorporating accurate mechanical properties for each part of the brain into computational models of TBI is a necessary prerequisite for biofidelic predictions.

Brain tissue can roughly be divided into gray and white matter. Gray matter consists of cell bodies, dendrites, and unmyelinated axons, while white matter mostly consists of myelinated axons [10]. Because white matter consists of tracks of myelinated axons, white matter may be more anisotropic than gray matter, therefore exhibiting more directional dependence when subjected to a load. However, there is ongoing debate regarding the actual differences in mechanical properties between gray and white matter. The wide discrepancy of mechanical property parameters in the literature for brain tissue could be dependent upon a variety of different factors such as time post-mortem prior to experimentation, experimentation on different species, use of different mechanical testing methodologies, range of tissue deformation during experimentation, and simplifying assumptions. Because of the lack of consensus in the literature regarding brain mechanical properties, conducting more studies to shed light upon the true mechanical properties of brain tissue is necessary.

One way that researchers study the mechanical properties of brain is by conducting indentation studies [10-12]. Indentation experiments with small probes have the advantage of high spatial resolution. An additional benefit of indentation testing, especially with relatively small indenters, is that they can be used to conduct tests on individual anatomical structures or even substructures, e.g. pyramidal subregions of the hippocampus. The force indentation data from these experiments can then be analyzed to extract mechanical properties.

1.2 Cerebral Edema and the Gibbs-Donnan Effect

Cerebral edema, otherwise known as brain swelling, is associated with unfavorable prognosis and is a leading causing of in-hospital mortality [13]. It is a major cause of death and disability following TBI because it leads to increased ICP as the brain swells within the fixed volume of the skull, which inhibits blood and oxygen perfusion to the brain. This lack of blood and oxygen to the brain causes subsequent ischemic damage [14]. Cerebral edema has classically been subdivided into two types: vasogenic and cytotoxic, but much research is still ongoing to elucidate its specific mechanism [15]. Cerebral edema is also a severe consequence of acute ischemic stroke in addition to TBI [16].

One of the most widely used treatments for cerebral edema is mannitol, but there is little supporting evidence for its usefulness in treating patients experiencing swelling following acute stroke [17] or TBI [18]. Determining the exact mechanism of cerebral edema may lead to better treatments and allow cerebral edema to be modeled using FE head models. Incorporating cerebral edema into FE head models would allow for calculation of ICP after a simulated TBI. This could enhance the capability of FE head models to better predict patient outcome following TBI and aid in the development of better safety systems because of the strong association between increased ICP and likelihood of death.

The forces responsible for driving water from the external environment into the viscoelastic matrix of brain tissue must be sufficient to cause sustained pathological levels of ICP as seen in the clinic. We hypothesize that water intake is caused by the Gibbs-Donnan effect due to the exposure of intracellular FCD, which could be demonstrated by modeling the brain as a triphasic material. A triphasic material consists of an interstitial fluid phase, a solid matrix phase consisting of fixed charges, and an ionic species within the fluid phase [19]. Because brain

tissue is comprised of cells, extracellular matrix, water, mobile ions, and fixed negative charges from macromolecules such as DNA and proteoglycans, it may behave like a triphasic material [20]. Triphasic materials can swell because exposure of negative fixed-charge densities (FCD) attached to the porous solid matrix attract positive ions to enter and increase the osmolarity of the space within the solid matrix. In turn, water rushes in and causes the porous solid matrix to expand to equalize the osmolarity between the external fluid phase and space within the solid matrix.

In a normal, healthy brain cell, Na^+/K^+ pumps use energy from ATP to pump cations out of the cell, thus leaving the FCD charged, underhydrated, and shrunken. The cellular membrane shields intracellular FCD from excess cations residing in the extracellular environment. However, when brain cells die due to ischemic damage or mechanical damage, the counteractive force of the Na^+/K^+ pumps cannot adequately pump out cations into the external environment, thus allowing these external cations to rush into the cell as they are attracted to the opposite charge of the FCD within the matrix of the cell, thereby increasing the osmolarity of the intracellular environment. Water then rushes into the cell due to the difference in osmolarity between the internal and external environment of the cell, causing the cell to swell. The resulting Gibbs-Donnan swelling pressure can be determined by Equation 1, where p is the interstitial fluid pressure, R is the universal gas constant, θ is the absolute temperature in the tissue and bath, and p_* and c_* respectively represent the ambient pressure and osmolarity of the external bath fluid.

Equation 1

$$p - p_* = R\theta(\sqrt{(C^F)^2 + c_*^2} - c_*)$$

Elkin *et al.* has provided evidence that cell death and subsequent exposure of intracellular FCD caused tissue swelling in vitro by showing that application of either Triton X-100 or cyanide + 2DG to brain tissue samples (to either increase porosity of cell membranes or reduce Na^+/K^+ pump activity, respectively) increased tissue volume [20]. Furthermore, Elkin *et al.* has provided additional evidence that triphasic swelling biomechanics is consistent with brain swelling by demonstrating decreases in brain tissue swelling when using various enzymes to cleave FCDs within the brain tissue *in vitro* [21].

1.3 Detrimental Effects of Hematoma Following TBI

The presence of a hematoma is one of the worst indicators of patient outcome following TBI. In nearly all significant cases of TBI, there is damage to the cerebral blood vessels, thus leading to the formation of a hemorrhage, which ultimately leads to formation of a hematoma [22]. Because of its prevalence in cases of severe TBI, much ongoing research seeks to determine the pathophysiology of death and disability due to hematoma.

Hematoma occurs when injury disrupts blood vessels, causing blood to leak within the skull [23]. Acute subdural hematomas (ASDH) are a particular type of hematoma in which bleeding occurs under the dura membrane, and some studies state that they are the most important cause of death in severely head injured patients [24] while other studies state that ASDH is associated with high mortality [25], with some sources indicating that mortality rate can range from 45% to 63% [26-31]. ASDH occurs when blood vessels, such as bridging veins, rupture. Bridging veins, which traverse through the dura, act as drains to pull blood away from brain tissue and return it to the heart for continued circulation. Mechanistically, during head impact, especially during occipital head impact, the brain lags behind the skull, causing a

longitudinal strain in the bridging veins which leads to tearing [32]. However, when injury occurs, these bridging veins can tear if they deform past their ultimate strain, causing blood to leak and pool under the dura [33].

Hematomas may be dangerous because of their space-occupying effect in which they compete with the volume of the brain within the limited fixed volume of the skull. A hematoma's presence, therefore, may compress and damage the brain tissue adjacent to it [34]. As a result, the compressed brain tissue beneath the hematoma could experience ischemia, defined as a lack of blood flow to that particular area of the brain due to compression of blood vessels within the tissue. If blood flow drops to 30% of control levels in a region of the brain, signs of brain swelling can occur [35]. Brain swelling may occur because decreased blood flow causes reduced oxygen and decreased ATP energy supplies in the ischemic region of the brain, leading to reduction of Na^+/K^+ pump activity. We hypothesize that reduction of Na^+/K^+ pump activity allows the influx of cations into the cell attracted by the underhydrated and negatively-charged FCD within the cell. The influx of cations into the FCD matrix increases the local osmolarity, generating an osmotic potential leading to a subsequent influx of water based on the mechanism described previously [36].

1.4 Significance of This Work

Over the decades, automobile manufacturers and automotive safety agencies have focused their safety research efforts on the prevention of TBI. Data shows that TBI is responsible for many deaths from car accidents. According to National Automotive Sampling System - Crashworthiness Data System (NASS-CDS) data from 2010 to 2015 and National Automotive Sampling System - Pedestrian Crash Data Study (PCDS) data from 1994 to 1998,

the head sustained the most life threatening injury in 33% and 46% in fatal accidents, respectively, indicating that head injury is the most frequent cause of death in both car and pedestrian accidents [37]. Although many research efforts in automotive safety have attempted to address TBI by predicting patient outcome following a car accident, current attempts to accurately predict patient outcome following automotive accidents are inadequate. Contemporary tissue-level injury predictors used to evaluate patient outcome following a car accident include parameters such as maximum principal strain (MPS) and cumulative strain damage measure (CSDM) [38]. Several studies have used these methods to compare the probability of predicted injury to observed injury rates for accident data from the Abbreviated Injury Scale (AIS) 2 to 4 (moderate to severe injuries), but not for fatal accidents [39-41]. Parameters such as MPS and CSDM only measure primary injury, but patient outcome following TBI can depend on the severity of both the primary and secondary injuries. Primary injury occurs as a result of initial injury forces that cause tissue distortion, deformation, and destruction at the time of the impact [42]. Secondary injury is defined as the biomolecular-, cellular-, and tissue-level changes that occur as a consequence of primary injury and can develop over minutes, hours, or days. Cerebral edema falls under the category of secondary injury and has a large effect on patient outcome because it leads to increased ICP. ICP is an important parameter that has been used to predict patient outcome, and some studies have shown that increased ICP leads to an increased probability of mortality [43, 44]. Since secondary injury such as cerebral edema and increased ICP can be such a powerful predictor of patient outcome following a car accident, we hypothesize that predicting the pattern and magnitude of brain swelling following primary injury could lead to more accurate predictive models of patient outcome following car accidents, and thus assist in the design and production of safer vehicles. Therefore, the work presented in

this thesis is significant because it addresses two issues that exist with current FE head models: the lack of accurate mechanical properties to predict the resulting accurate strain field in brain tissue after TBI and the inability of current FE head models to model cerebral edema and ASDH which can drastically affect patient outcome following TBI.

Chapter 2: Region-dependent Mechanical Properties of Human Brain Tissue Under Large Deformations Using Inverse Finite Element Modeling

2.1 Introduction

In the United States on an annual basis, about 2.5 million injury-related emergency department (ED) visits, hospitalizations, and deaths include traumatic brain injury (TBI) as the primary or secondary diagnosis [45]. TBI occurs when head acceleration causes large deformation of the brain tissue. Brain tissue mechanical properties may vary between anatomical structures. Under external load, heterogenous strain fields develop across anatomical structures, which could give rise to a broad spectrum of post-traumatic conditions including cognitive, behavioral, motor, and somatic symptoms [46-48]. To correctly predict the functional consequences of TBI, which may depend on the anatomical structure injured, finite element (FE) models have been used to calculate the distribution of stress and strain in the brain during a loading event. Recent advancements in neuroimaging tools help FE models achieve sufficient sophistication to explicitly represent different anatomical structures of the brain, and modern computational resources can more efficiently solve these anatomically detailed models. These computational models could offer helpful insights into the pathologies that arise from injury to different brain structures. However, the necessary mechanical properties to populate these models are lacking. The aim of this study was to utilize an inverse FE approach coupled with micro-indentation experiments on fresh human brain tissue to determine structure-specific mechanical properties.

Micro-indentation testing offers great spatial resolution in the measurement of tissue mechanical properties because the captured load-displacement data mostly depends on the small domain of the material adjacent to the tip of the indenter. Inspired by our previous work on rat [49-51], pig [52] , and human brain tissue [52, 53] using micro-indentation testing, herein, using an inverse FE approach, we reanalyzed previously collected data from human brain tissue samples resected during surgery. The use of fresh, post-operative tissue is highly advantageous as it avoids pitfalls of cadaveric tissue and allows data to be collected before degenerative processes alter mechanical properties [54].

A challenging aspect of TBI biomechanics is the modeling of the large strains that arise during head injury. Previous studies have modeled indentation using closed-form mathematical solutions under the assumption of small strain [52, 53]. However, the small strain assumption may be invalid at larger deformations that arise either during indentation testing or during moderate to severe TBI. In this study, an inverse FE modeling scheme for brain tissue indentation was employed to circumvent the limitation of the small strain assumption to extend the study to finite strain analysis.

2.2 Methods

2.2.a Tissue Preparation, Indentation Testing, and Data Processing

In this study, we reanalyzed the previously collected data from human brain tissue samples resected during surgery [52]. All patients provided informed consent, and protocols were approved by Columbia University's Institutional Review Board. The sex and age of sample donors are listed in Table 1. Sections of human non-sclerotic hippocampus and non-epileptic neocortex were taken from 11 patients of both sexes ranging in age from 4 to 58 years

during surgical procedures to resect underlying epileptic foci. 1 mm thick slices of tissue were cut using a vibratome (Vibratome 1000 plus, The Vibratome Company) and transported in Gey's solution containing 4.5 mg/mL glucose (Sigma). At the time of indentation testing, the slices were adhered to a Petri dish using a thin layer of cyanoacrylate glue and bathed in warmed CO_2 independent medium (Gibco) supplemented with 4.5 mg/ml glucose (Sigma). The testing was completed within 6 hours following resection [54].

To extract the mechanical properties from white and gray matter of the cortex as well as CA1, CA3, and dentate gyrus of the hippocampus, indentation testing was performed on a custom-designed micro-indentation device as previously described [53]. The Petri dish containing the sample slices was mounted on a 10 gram capacity load cell (GSO-10, Transducer Techniques). A cylindrical indenter with a 250 μm radius was mounted on a linear actuator (M-227.10, Physik Instrumente), and its displacement was monitored with a capacitive transducer (capaNCDT 6100, Micro-Epsilon). After a tare load of 1-2 mg was achieved, three consecutive indentations were performed on the tissue to displacements of 40, 80, and 120 μm. During each step, the tissue was indented by 40 μm in 70 ms, with a maximum shear Lagrange strain rate (mean ± standard error of the mean) of 3.57 s^{-1} ± 0.02 s^{-1} for the first indentation, 1.42 s^{-1} ± 0.04 s^{-1} for the second indentation, and 0.79 s^{-1} ± 0.02 s^{-1} for the third indentation, and held for 19.93 s to capture the stress relaxation response. Both displacement and load data were acquired with custom LabVIEW code (LabView 8.6, National Instruments) at 10 kHz. The collected data was de-noised by removing 60 Hz harmonics and down-sampled to provide equal weight between short-term and long-term viscoelastic behaviors. For each indentation step, the filtered data was reduced to 100 points for fitting with 50 points linearly distributed over the first 100 ms and another 50 points logarithmically distributed over the remaining 19.9 s stress relaxation period.

Table 1: Sex and age of sample donors. The regions examined were the cortex gray matter (CtxG), cortex white matter (CtxW), cornu ammonis 1 (CA1), cornu ammonis 3 (CA3), and dentate gyrus (DG).

Sample Number	Sex	Age	Region
1	Male	4	CA1, CA3, CtxW, CtxG, DG
2	Male	31	CtxW, CtxG
3	Male	43	CtxW, CtxG
4	Female	7	CA3, CtxW, CtxG, DG
5	Male	50	CA1, CA3, DG
6	Female	27	CtxW, CtxG
7	Male	12	CA1
8	Female	19	CtxW, CtxG
9	Unknown	Unknown	CtxW, CtxG
10	Male	58	CA1, CA3, CtxW, CtxG
11	Female	35	CA1, DG

2.2.b Finite Element Model and Simulation

A finite element model was created in FEBio (febio.org) to simulate the indentation experiments [55, 56]. The cylindrical indenter was modeled as a rigid body with a radius of 250 μm. The outer edge of the indenter was modeled with a rounded fillet radius of 20 μm, which matched that of the indenter used in the experiment. The brain tissue was modeled as a nearly-incompressible viscoelastic material using an uncoupled strain energy formulation for either an Ogden, Neo-Hookean, or Mooney-Rivlin constitutive model, all of which are isotropic. The tissue model had a thickness of 1 mm and a radius 10 times larger than the radius of the indenter to avoid edge-effects. The relaxation function was expressed as the following Prony series:

Equation 2

$$G(t) = G_0 + \sum_{i=1}^{N} G_i \, e^{-\frac{t}{\tau_i}}$$

where G_i are viscoelastic coefficients and τ_i are relaxation times. Viscoelastic coefficient G_0 was set to 1 by default in FEBio. The strain energy density function for each constitutive formulation

is listed in Table 2. For Ogden, c_i and m_i are mechanical parameters, $\tilde{\lambda}_1$, $\tilde{\lambda}_2$, and $\tilde{\lambda}_3$ are eigenvalues of the deviatoric right-stretch tensor, J is the determinant of the deformation gradient tensor, and $U(J)$ is the dilatational energy in the simulation of nearly-incompressible behavior. For Mooney-Rivlin and neo-Hookean materials, C_1 and C_2 are mechanical parameters, $\tilde{I}_1$ and $\tilde{I}_2$ are the first and second invariants of the deviatoric right Cauchy-Green deformation tensor, and the coefficient K is the bulk modulus associated with the function $U(J)$. K was set to a high enough value to ensure mesh elements changed in volume by no more than 1% during simulations ($0.99 \leq J \leq 1.01$).

The tissue model was meshed with 3D quadratic hexahedral and pentahedral elements. Given the geometry of the experimental indentation configuration, an axisymmetric approach was used to minimize computation time and simplify the geometry as a 3° wedge (Figure 1) with appropriate boundary conditions (symmetry planes defined on wedge faces). A tied-elastic interface was employed between the inner and outer wedge domains, to accommodate disparate meshing. Simulating the experimental condition of using cyanoacrylate to adhere the tissue to the Petri dish, the nodes at the bottom surface of the mesh were fixed. A z-direction displacement was prescribed to the indenter to match the experimental indentation displacement profile. A frictionless sliding elastic contact interface simulated the interaction between the indenter and the upper surface of the tissue, and the interface between the two non-conforming surfaces in the mesh representing the tissue was defined as a tied-elastic interface. The mesh was biased in both x and z direction such that the smallest elements in the mesh occupied the region underneath the indentation contact.

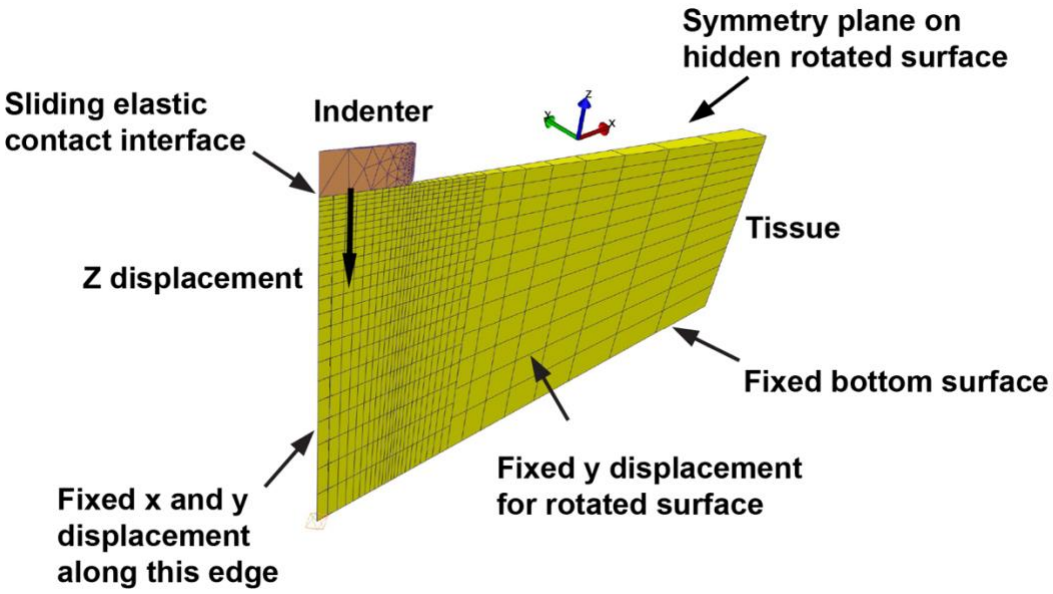

Figure 1: The finite element model. The meshes of the indenter and tissue are labeled.

2.2.c Mesh Convergence Study

Prior to creating the mesh in Figure 1, a mesh convergence study was performed. A mesh convergence study is necessary to ensure that the elements are small enough to accurately represent the spatial gradients within the mesh without introducing numerical artifacts, like artificially stiffening the response of the mesh. A competing criterion is that a mesh with fewer elements is advantageous because it shortens computational time. However, the disadvantage is that solutions may be artificially stiff. Conducting a mesh convergence study is necessary to find the appropriate balance between computational time and solution accuracy.

A mesh convergence study was conducted by creating meshes ranging from fewer elements to many elements (Figure 2). Mesh a had 1,152 brain tissue elements with a minimum element size of 7.5 μm, Mesh b had 4,608 brain tissue elements with a minimum element size of 4.4 μm, and Mesh c had 10,368 brain tissue elements with a minimum element size of 4.1 μm.

All meshes used quadratic elements (as opposed to linear elements) because we found that running simulations with fewer quadratic elements yielded solutions that matched meshes with many more linear elements but that took much longer to run.

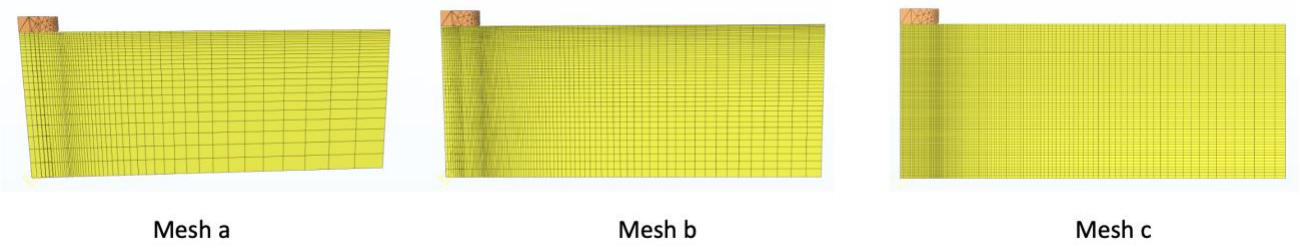

Figure 2: Meshes used in mesh convergence study.

The same indenter displacement profiles and external mesh geometries were applied to each mesh, and indenter z-forces were compared since this is the output parameter used for optimization in the inverse FE cycle.

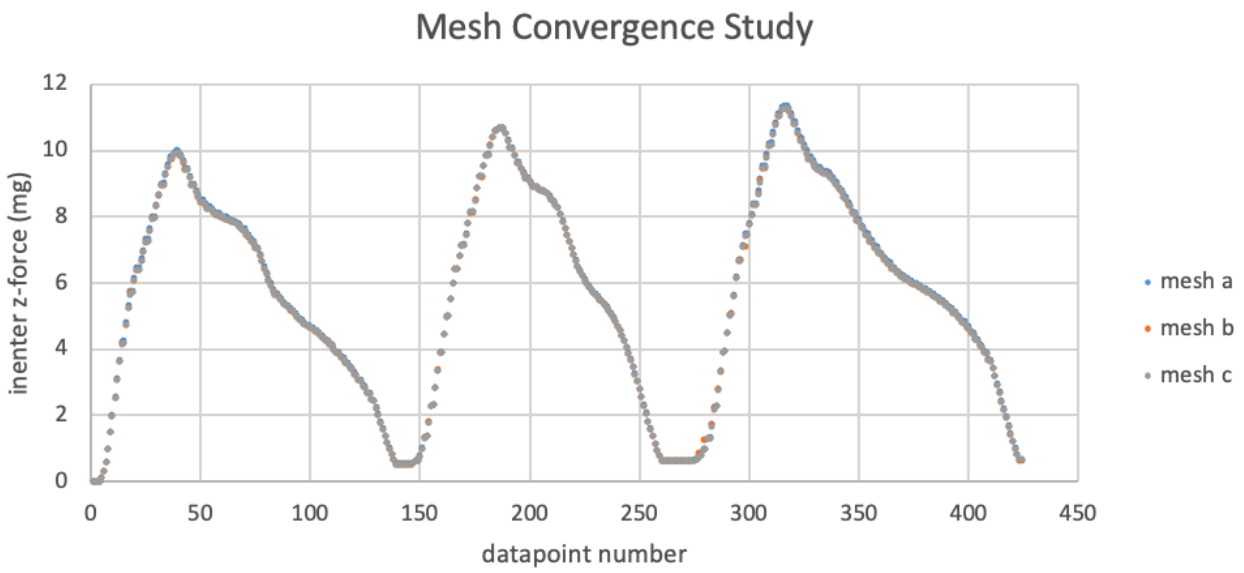

Figure 3: Plot showing indenter z-forces for all meshes shown in Figure 2.

Visually, the forces among all three meshes appear almost identical, but the difference in forces between meshes b and c are smaller than the already small force differences between mesh a and b, despite the significantly larger number of elements in mesh c (Figure 3). The RMSE between mesh a and b was 0.049 mg with a peak percent difference of 5.2%, and the RMSE between mesh b and mesh c forces was 0.027 mg with a peak percent difference of 4.4%. We concluded that the mesh we use to run inverse FE simulations should match the forces from mesh c as closely as possible. In other words, we considered mesh c to produce the ground truth simulation.

Next, we created a mesh that produced forces close enough to the ground truth mesh but could also be simulated quickly enough so that iterative inverse FE procedures would not be computationally burdensome and time-consuming. After testing several iterations of meshes, we settled on the mesh in Figure 1. This mesh has smaller elements under the indenter and larger elements everywhere else. The intent was to ensure that deformations (and gradients) were as

accurate as possible near the indenter by creating smaller elements underneath the indenter, but that the overall mesh had as few elements as possible to speed up run time. Forces from this "mismatched nodes" mesh (Figure 1) were compared to our ground truth mesh (Figure 2, mesh c) for the Ogden formulation. Herein, we present data from meshes using elements with an Ogden material formulation because it fit the data better than Mooney-Rivlin or Neo-Hookean formulations.

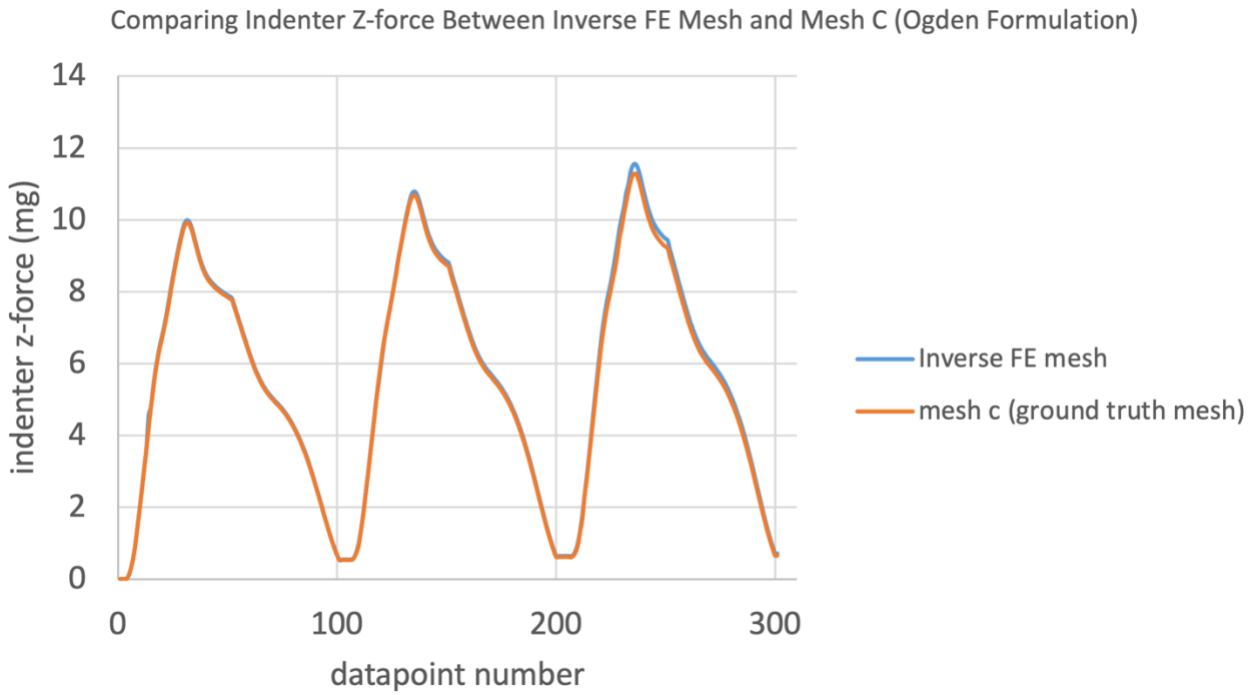

Figure 4: Comparing indenter z-forces between our currently used mesh in inverse FE simulations (see Figure 1) and the ground truth mesh (Figure 2, mesh c) with the Ogden material formulations. Note that the indenter force is plotted for each data point and not as a function of time. This representation gives equal visual weight to both the rapid and long-term response of the simulation for each of the three indentation steps.

As presented in Figure 4, there is a close overlap (RMSE = 0.12 mg) between the chosen inverse FE mesh and the ground truth mesh (Figure 2, mesh c) with a maximum percent

difference of 3.6%. Overlap was also close when we simulated material parameters in both meshes that produced higher forces where the third indentation peak was between 40-50 mg. Therefore, we concluded that the mesh in Figure 1 could be used to determine material properties of brain using inverse FE methods.

In summary, a study of meshes with minimum element dimensions of 4.1 (Figure 2, mesh c), 4.4 (Figure 2, mesh b), 7.5 (Figure 2, mesh a), and 10.9 μm confirmed that the mesh converged when the minimum element dimension was 10.9 μm; this mesh was used for all subsequent simulations (Figure 1).

Table 2: Strain energy density function for each constitutive model, where $U(J) = \frac{1}{2}K(\ln J)^2$.

Constitutive formulation	Strain energy density function
Ogden	$\Psi = \sum_{i=1}^{N} \frac{c_i}{m_i^2}\left(\tilde{\lambda}_1^{m_i} + \tilde{\lambda}_2^{m_i} + \tilde{\lambda}_3^{m_i} - 3\right) + \frac{K}{2}(J-1)$
Neo Hookean	$\Psi = C_1\,(\tilde{I}_1 - 3) + U(J)$
Mooney Rivlin	$\Psi = C_1\,(\tilde{I}_1 - 3) + C_2(\tilde{I}_2 - 3) + U(J)$

2.2.d Inverse Finite Element Method

Inverse FE simulations were conducted in FEBio [55, 56] to determine the mechanical parameters that minimized the objective function:

Equation 3

$$f(a) = \sum_{i=1}^{n} [y_i - y(x_i; a)]^2$$

where (y_i, x_i) were pairs of experimental force-displacement data and $y(x_i; a)$ was the corresponding reaction force output, which was the reaction force of the rigid indenter, from a FE simulation with mechanical parameters a. The FEBio solver implemented the constrained Levenberg-Marquardt method which solved the nonlinear squares problem with a combination of steepest gradient descent and Gauss-Newton's method [57].

Force displacement curves of 73 individual samples including cortex gray matter, cortex white matter, CA1, CA3, and dentate gyrus were collected from the indentation testing [52]. The force-displacement curves within each region were averaged. To determine which constitutive model provided the overall optimal fit, inverse FE simulations were conducted using Ogden, Mooney-Rivlin, and Neo-Hookean constitutive formulations to fit averaged regional force-displacement curves. The sum of squared error (SSE) was calculated against each averaged regional response. The formulation with the lowest SSE was chosen as the optimal model and used for all subsequent analysis. In addition, to determine the effect of sex, age, and region on mechanical behavior, the inverse FE simulations were performed on individual sample data to extract corresponding mechanical parameters.

2.2.e Virtual Indentation

To assess differences in brain tissue response as a function of sex, age, or location, we used optimized parameters from inverse FE simulations from each of the 73 individual experimental samples to conduct virtual indentations under a single large deformation, as opposed to relying on detecting statistical differences between material constants because different combinations of hyperelastic and viscoelastic parameters could produce similar load results. A virtual z-displacement vector was created for the indenter to simulate the experiment

as a single indentation of 120 μm in 70 ms with a trapezoidal motion profile and held at that position for a total of 20 s. Based on optimized mechanical parameters extracted from individual samples through inverse FE simulations, the virtual indentation was simulated, and the load at 70 ms was extracted from each simulation for comparison.

2.2.f Statistical Analysis

Two-term, three-term, and four-term Prony series were tested for the viscoelastic model in Equation 2. The optimal number of terms needed in the Prony series was determined by the F-statistic [49, 51] using the equation:

Equation 4

$$F = \frac{(SSE_S - SSE_L)/(K_L - K_S)}{SSE_L/(N - K_L - 1)}$$

where SSE_L is the sum of the squared error of the larger Prony fit, SSE_S is the sum of squared error of the smaller Prony fit with one fewer term, K_L is the number of parameters in the larger Prony fit, K_S is the number of parameters in the smaller Prony fit and N is the number of data points analyzed for each fit. However, if the magnitude of the 95% confidence interval was larger than the corresponding fitted parameters, the reduced model was accepted. Two-way ANOVA followed by a Bonferroni *post hoc* test was performed on the simulated loads from virtual indentations to determine the effects of region and sex. T-tests were conducted to determine the effect of sex within each region. The effect of age was assessed using linear regression. Significance was set as $p < 0.05$.

2.3 Results

2.3.a Ideal Constitutive Model and Optimized Mechanical Parameters

Based on the averaged SSE across all averaged regional responses for each constitutive model, the Ogden constitutive formulation provided the best fit to the experimental data (Table 3).

Table 3: The average summed squared error (SSE) of all constitutive formulations when fitting to the averaged experimental load-displacement curve for all anatomical regions.

Constitutive Model	Averaged SSE (mg^2)
Ogden	45.85
Mooney-Rivlin	266.08
Neo-Hookean	516.05

An example comparing the fit of each constitutive model for the averaged dentate gyrus experimental load data is shown in Figure 5. The best fit parameters along with their 95% confidence intervals for each averaged regional response are displayed in Table 4. As determined by the F-statistic, a two-term Prony series best fit the data for cortex white and cortex gray matter whereas a four-term Prony series best fit the data for the subregions (CA1, CA3, DG) within the hippocampus. Sorted by region, the fittings for all individual samples were averaged and shown in Figure 6.

Table 4: Best fit parameters using an Ogden constitutive model for different regions of human brain tissue with +/- 95% confidence interval. The bulk modulus for all simulations was 10^6 Pa to ensure that the brain tissue mesh was nearly-incompressible.

	G_1	G_2	G_3	G_4	τ_1(s)	τ_2(s)	τ_3(s)	τ_4(s)	c_1 (Pa)	m_1
CA1	874.4 ± 71.3	261.3 ± 39.3	199.4 ± 32.9	271.1 ± 16.7	0.0125 ± 0.0026	0.1439 ± 0.05	1.3 ± 0.4	41.5 ± 5.3	2.5 ± 0.01	16.4 ± 0.4
CA3	315.3 ± 0.015	90.1 ± 11.0	66.9 ± 11.2	98.3 ± 11.7	0.0115 ± 0.0024	0.1633 ± 0.05	2.0 ± 0.6	56.8 ± 11.0	7.2 ± 0.7	18.4 ± 0.4

DG	1932.2 ± 43.2	357.2 ± 99.1	237.8 ± 81.6	340.3 ± 107.8	0.0047 ± 0.0021	0.0842 ± 0.03	1.1 ± 0.3	47.4 ± 7.7	2.6 ± 0.8	21.9 ± 0.5
Cortex Gray	235.9 ± 35.2	124.5 ± 14.6			0.0515 ± 0.0056	26.9 ± 2.3			4.8 ± 0.500	15.0 ± 0.8
Cortex White	227.9 ± 12.0	90.2 ± 3.8			0.0445 ± 0.0043	21.3 ± 2.1			9.6 ± 0.002	18.1 ± 0.8

2.3.b Dependence of Mechanical Properties on Region, Sex, and Age

As determined by two-way ANOVA, brain region significantly affected mechanical behavior ($p < 0.05$). The load in the cortex white matter was significantly greater than that of the cortex gray matter; the load in the CA1 was significantly greater than that of the cortex gray matter; the load in the dentate gyrus was significantly greater than that of the cortex gray matter ($p < 0.05$) (Figure 7a). There was no significant effect of sex on brain tissue mechanical behavior. Although the average load of cortex gray matter, cortex white matter, CA1, and dentate gyrus in male was larger than those in female, there was no statistically significant sex-dependent difference in the load within each region (Figure 7b). Additionally, there was no age-dependent difference in the load within each region or for all samples (Figure 7c).

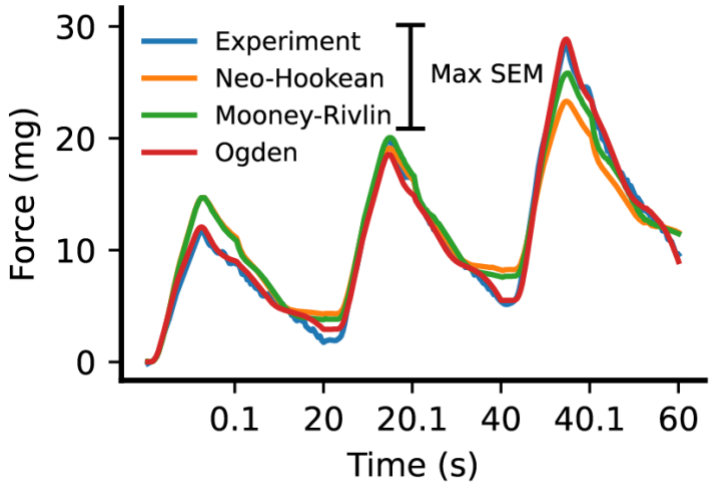

Figure 5: Inverse FE simulation using different constitutive models compared to the experimental load for averaged DG. The Ogden formulation fit the experimental data best. Data is plotted by down-sampled time point to highlight the fast indentation component of each step. Error bar represents the standard error of the mean.

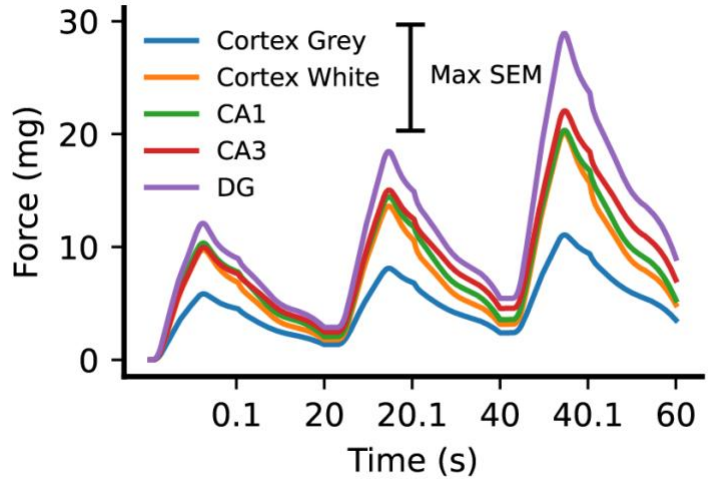

Figure 6: Simulated load curves using optimized parameters of different regions in the human brain. Data is plotted by down-sampled time point to highlight the fast indentation component of each step. Error bar represents the standard error of the mean.

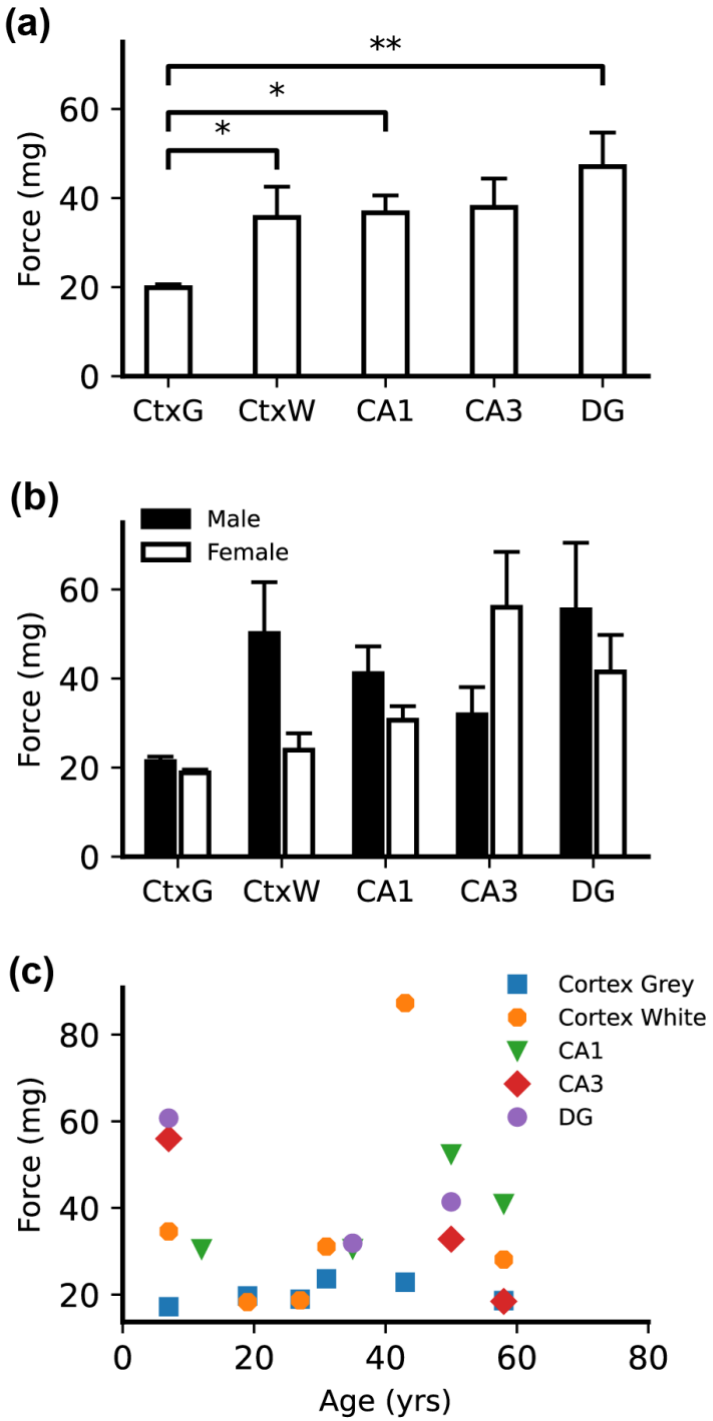

Figure 7: Load at 70 milliseconds of a single virtual 120 μm indentation step comparing the (a) effect of anatomical regions, (b) male versus female, and (c) age. In figure (b), there was no statistically significant difference between male and female load within any region. In figure (c), load was not dependent on age. * $p < 0.05$, mean ± SEM

2.4 Discussion

Compared to earlier work that conducted indentation experiments on cadaveric tissue followed by inverse FE analysis [58], our micro-indentation experiments conducted on fresh, post-operative human brain tissue in our previous study are highly advantageous as the mechanical properties were measured before postmortem changes could take place [54]. To our knowledge, our work is the first to use inverse FE methodology on multistep micro-indentation experiments on fresh, post-operative human brain tissue as opposed to cadaveric material, to generate highly localized measurements within human cortex gray matter, white matter, and hippocampus [53].

Using an inverse FE approach to reanalyze the data from our previous work [52], tissue mechanical properties differed significantly by anatomical regional. Specifically, cortex white matter was stiffer than cortex gray matter, which supports our previous study that was limited because of the small strain assumption [52]. Regional differences are further supported by another study reporting that human corona radiata was stiffer than gray matter [59]. These consistent results could be explained by structural differences between white and gray matter. White matter is comprised of highly oriented axonal tracks while gray matter is comprised of mainly dendrites, cell bodies, and glia in a random orientation [60]. However, other studies have reported that gray matter was stiffer than white matter [61, 62]. One of these studies used scanning force microscopy with indentations of only 3 μm, which may be too small of an indentation depth to apply to the large deformations typical of TBI [61]. Additionally, that study was conducted on rat brain tissue, which may have different properties than human brain tissue. In another study, the authors used non-invasive magnetic resonance elastography to compare the stiffness between human gray matter and white matter [62]. However, their methodology was

sensitive to noise due to the use of third-order derivative calculations, which may have affected their results [62]. A different study used magnetic resonance elastography to measure the stiffness of hippocampal subfields (subiculum, CA1, CA2, CA3, dentate gyrus) in human male subjects between 18 to 33 years old and found no significant regional differences [63], which also supports our finding that hippocampal stiffness is homogenous. Overall, we report regional variations in the mechanical properties of human brain, providing evidence that the heterogeneity of brain tissue may lead to regional disparities in injury susceptibility.

Due to the lack of a large strain analytical solution for cylindrical indentation of a viscoelastic layer, previously we reported mechanical properties of human brain tissue using a linear viscoelastic model assuming small strain [51]. However, nonlinear mechanical behavior of brain tissue has been observed for strains over 15% [50, 64]. In a more recent study, a quasilinear viscoelastic (QLV) model was adapted to characterize mechanical behavior of brain tissue under large strain [53]. To calculate load for a given strain in the QLV model, the authors used Equation 5 to define the nominal uniaxial compressive strain underneath the indenter where ϵ is strain, R is the radius of the indenter, and δ is the indentation depth.

Equation 5

$$\epsilon = \frac{2\delta}{\pi R}$$

However, in that study, the fitting of the QLV model was less optimal than the fitting of the linear viscoelastic model. A prerequisite for using Equation 5 is that it is only valid for "small strains", but it was used because it provided a definitive solution of the strain calculation for a given indentation depth and indenter radius. This equation, however, may not be valid for the larger strains induced during the tissue indentation experiments. The use of the strain approximation in Equation 5 also assumes that the strain field under the indenter is homogenous

and isotropic under uniaxial compression. Our FE models of indentation show that the strain field is indeed not homogenous, which could explain why the strains calculated using Equation 5 may not be valid for calculating load. In the current study, using an inverse FE approach and an FE solver for large nonlinear deformations, avoided the challenge of relying on the small strain assumption, allowing the constitutive model to more accurately capture the mechanical properties of brain tissue under large deformation.

In our inverse FE simulations, the Ogden constitutive formulation was found to be the optimal model, among those tested, for capturing the non-linear behavior of brain tissue. More specifically, this formulation was able to better capture the peaks in load corresponding to the 40, 80 and 120 μm indentation depths than the Mooney-Rivlin and neo-Hookean constitutive formulations. Our results support the use of QLV with an Ogden constitutive formulation for modeling the nonlinear mechanical behavior of human brain tissue. Other studies have also supported the use of QLV for brain tissue. Laksari *et al.* conducted uniaxial compression tests on cylindrical samples of bovine brain tissue and derived two isochronous curves (stress values at different strain-levels but at the same time interval after the peak stress during the compression experiment) [65]. They demonstrated that the ratio of two isochronous stress data at two different timepoints following the instantaneous jump in the displacement curve were not dependent on strain level, demonstrating the validity of the QLV assumption for strain levels up to 35%. In a study by Prange *et al.*, porcine brain tissue white matter (corona radiata and corpus callosum) and gray matter (thalamus) samples were tested in shear and unconfined compression in different directions to determine their mechanical behavior [66]. The Ogden constitutive model, modified to include dissipation, fit the constitutive relationships for all regions and directions well. In addition to modeling brain tissue, the Ogden constitutive formulation has also

been used to model the non-linear mechanical behavior of other soft tissues such as liver, for nominal compression up to 30%, fitting better than a Mooney-Rivlin formulation [67]. Another study found that the Ogden model better simulated rat brain and fat tissue than the neo-Hookean, Mooney-Rivlin, Fung, or Gent models [68].[31] These results on various soft tissues support our finding that an Ogden constitutive model is appropriate for human brain tissue.

In the limit of small strains, the material properties of the Ogden elastic solid (Table 2) reduce to those of a linear isotropic elastic material (Hooke's law), with equivalent Lamé constants $\lambda = K$ and $2\mu = \sum_{i=1}^{N} c_i$, where μ is the shear modulus ($2\mu = c_1$ here). Thus, in that limit, the equilibrium Young modulus of nearly-incompressible brain tissue is $E \approx \frac{3}{2} c_1$, with c_1 given in Table 4.

There was no significant difference in simulated load within an anatomical brain region between males and females. However, our small sample size limited the power of our statistics to an average of 0.34, requiring at least 12 additional samples for a power of 0.8. Despite the lack of statistical significance, trends in our data suggest that male cortex white matter may be stiffer than female cortex white matter. The difference in stiffness could help explain the difference in TBI outcomes between males and females with females experiencing greater neurological deficits. Because female cortical white matter may be softer, it may experience larger deformations during head acceleration, leading to greater tissue damage for the same macroscopic acceleration. In addition to other physiological factors, studies have also reported that females have higher gray matter percentage while males have more white matter [69-71]. Combined with the trend observed in our study that cortex white matter is stiffer than cortex gray matter, the difference in gray and white matter percentage could further contribute to female

susceptibility to TBI. Given that most finite element models of brain are independent of sex, it may be critical to build models with appropriate sex-specific mechanical properties.

An advantage of testing samples resected from surgery is access to brain samples from patients over a wide range of ages. In this study, the age of donors ranged from 4 to 58 years, however, age did not affect mechanical properties. Our result is in agreement with a previous report in humans ranging in age from 45 to 94 years old [59]. However, a significant increase in brain tissue stiffness between 5 months and 22 months was observed in another study [72]. Additionally, in contrast to our study, animal studies revealed a different pattern of age-dependent mechanical properties. In rats, brain shear moduli of different anatomical regions were greater in adult rats than in postnatal day 17 rats [73]. In pigs, infant brain tissue was softer than that of adult brain tissue [74]. Collectively, these studies suggested that human brain tissue may mature mechanically earlier in neurodevelopment. Although human brain mechanical properties may remain consistent throughout most of life, it is still important to take into account the geometry and size of the brain which varies by age. One study examining the cerebral volumes of 100 men and women between age 25 and 83 found that the cerebral volume of men tended to decrease by approximately 5 mL/year, whereas cerebral volume in women did not [75]. Therefore, it may be possible to use the same mechanical parameters for different ages provided the model incorporates age-specific size and geometry.

Despite the advantages of our study, there were some limitations. Due to the difficulties of procuring human brain tissue, the observations made in this study were confined to a small sample size such that the statistical tests may have been under-powered. Moreover, although the virtual indentation provided an indication of how the regions would respond to a single large deformation, future experimental validation is needed to determine the validity of extrapolating

from three smaller cumulative indentations to a single large indentation. We also assumed that the tissue under the indenter was isotropic, which may be a concern because white matter may be anisotropic. One study reported that white matter was stiffer in the direction parallel to the axons [76]. Although that study was conducted using bovine brain tissue, human white matter may behave similarly, given its structural similarity. Anisotropy of white matter due to axon orientation could be important in determining patient outcome following TBI, especially because serious pathologies, such as diffuse axonal injury (DAI), are caused by axonal strain. For example, one study proposed that the brain injury tolerance limit for a 50% risk of DAI was 14.65% axonal strain [77]. Therefore, the orientation of white matter during injury will affect the induced strain and the resulting damage.

The applicability of our results to severe or penetrating TBI could be limited due to the strain rate of our indentation testing. In our study, the indenter was displaced at an averaged maximum Lagrange shear strain rate of 0.79 s^{-1} to 3.57 s^{-1} depending on the indentation step. However, previous studies using physical and computational models suggested that strain rates operant during acceleration-driven TBI are on the order of 10 s^{-1} [72, 78-81]. Although strain rates in our indentation paradigm were lower than those thought to arise during severe impact TBI, they are larger than strain rates applied in some other studies measuring brain mechanical properties [82-86]. Furthermore, the shortest time constants across all regions in our study were on the order of tens of milliseconds (Table 4). TBI usually occurs within time scales < 100 ms [73], indicating that our results captured the short-term mechanical behavior of brain appropriate for modeling TBI.

In conclusion, we have identified that the mechanical properties of fresh human brain tissue are region-dependent, but neither sex- nor age-dependent within the statistical power of

our sample size. The mechanical behavior of brain tissue under large deformation was accurately modeled using an Ogden constitutive formulation in FEBio without relying on a small strain approximation. Our study characterized human brain tissue mechanics and provided mechanical properties to improve brain finite element models to predict a more biofidelic response, which furthers our understanding of TBI pathology and can be applied to the development of more effective safety systems.

Chapter 3: Fixed Charge Density Measurements of Brain Tissue Using Confined Swelling Pressure Methodology

3.1 Introduction

Traumatic brain injury (TBI) is a leading cause of death and disability in the United States [87]. In 2003, there were an estimated 1,565,000 TBIs in the United States: 1,224,000 emergency department visits, 290,000 hospitalizations, and 51,000 deaths [88]. TBI can occur from many types of trauma including motor vehicle accidents, falls, and crush injuries. TBIs are also typically classified into primary injury and secondary injury, where primary injury is caused by mechanical forces acting on the brain, and secondary injury is caused by biomolecular and physiological changes that occur in the brain following primary injury [42]. Secondary injuries, which significantly contribute to the prognosis of patients suffering from TBI [89], include processes such as ischemia, swelling, and alterations of endogenous neurochemical mechanisms [90]. One of the worst types of secondary injury resulting from TBI is cerebral edema, also known as brain swelling. Cerebral edema is associated with unfavorable prognosis and is a leading causing of in-hospital mortality [13], increasing mortality rates by up to 80% in severe cases [91] of cerebral edema, and responsible for up to half of all mortality and morbidity in younger victims of TBI [92].

Cerebral edema is a major cause of death and disability following TBI because it leads to increased intracranial pressure (ICP) [93]. ICP increases because the brain swells within the fixed volume of the skull. This swelling within the fixed volume of the skull causes certain regions of the brain parenchyma to be compressed, which in turn compresses brain tissue vasculature. Compressed vasculature increased the resistance and therefore lowers the cerebral

blood flow (CBF) to the affected brain tissue, and this lack of blood and oxygen to the brain causes subsequent ischemic damage [14], killing the brain tissue. Despite high mortality rates associated with cerebral edema following head injury, the underlying mechanism causing swelling is not fully understood.

There are currently several procedures used to clinically treat cerebral edema: administration of hypertonic saline, administration of mannitol, and decompressive craniectomy. Hypertonic saline is administered into the blood stream and lowers ICP by establishing an osmotic gradient between the intracellular and intravascular space [94]. There is also evidence that hypertonic saline also optimizes blood viscosity and cerebral blood flow, allowing compensatory vasoconstriction mechanisms to cause a reduction in cerebral blood volume to lower ICP [94]. However, there are also potential complications that may arise with the use of hypertonic saline such as renal failure, osmotic demyelination syndrome, a rebound increase in ICP, coagulopathies, volume overload, and electrolyte abnormalities [95]. Mannitol is also widely used, and there are currently two theories that potentially explain how it may decrease ICP. One theory argues that mannitol lowers ICP by reducing cerebral blood volume, either by raising blood pressure or by reducing blood viscosity, which induces reflex vasoconstriction; the other theory argues that mannitol acts to reduce brain water content by drawing water from the cerebral extracellular space into the vasculature though establishment of an osmotic gradient between plasma and brain cells [96, 97]. Despite mannitol's widespread use, there is little supporting evidence for its usefulness in treating patients experiencing swelling following acute stroke [17] or TBI [18]. The use of mannitol can also lead to complications such as electrolyte abnormalities, hypotension, and congestive heart failure with pulmonary edema [98]. Post-traumatic cerebral edema is also treated by decompressive craniectomy, a practice in which a

large bone flap along with the underlying dura is removed to allow swelling to occur but without an increase in ICP so as to maintain blood flow [99]. However, decompressive craniectomy leads to many potential complications such as high rates of infection, development of subdural hygromas and hydrocephalus, and many other cognitive, psychological, and neurological deficits [100]. The high mortality rate associated with cerebral edema and the complications associated with using hypertonic saline, mannitol, or decompressive craniectomy warrants a new type of treatment that is safer and more effective. Creating a new treatment, however, necessitates a better understanding of the mechanism of cerebral edema.

Traditionally, cerebral edema has been divided into three main categories: vasogenic, cytotoxic, and interstitial edema. Vasogenic edema occurs when there is breakdown of the tight endothelial junctions of the blood-brain barrier (BBB), leading to extravasation of intravascular protein and fluid into the interstitial space of the brain [101]; cytotoxic edema occurs when water moves into the intracellular compartment of brain cells [102], and interstitial edema occurs due to obstructions of cerebrospinal fluid outflow [14]. Some studies have characterized the type of edema following TBI to be mainly cytotoxic in nature [103, 104]. Therefore, determining the mechanism of post-traumatic cytotoxic edema would be paramount in facilitating efforts to discover new treatments.

The forces responsible for driving water from the external environment into the viscoelastic matrix of brain tissue must be sufficient to cause sustained pathological levels of ICP as seen in the clinic. Other studies have attempted to deduce the molecular mechanism for cytotoxic edema, with some stating that influx of sodium, cause by failure of Na^+/K^+ pumps due to ischemic damage, followed by an influx of chloride ions causes obligated water to flow into the interior of the cell [102, 105]. However, these mechanisms may not reveal the entire truth,

since ions can also flow outwards from the inside of the cell to the external environment, thus counteracting the influx of water. A component of the mechanism must be responsible for keeping ions within the intracellular environment of the brain cell to ensure a subsequent influx of water.

We hypothesize that exposure of intracellular FCD caused by cell death is one of the main drivers responsible for causing water to flow into the intracellular environment leading to brain swelling. Therefore, modeling the brain as a triphasic material which could help represent intracellular FCD exposure during cell death may aid in the modeling of cerebral edema within FE head models. A triphasic material consists of an interstitial fluid phase, a solid matrix phase consisting of fixed charges, and a counter-ionic species within the fluid phase [19]. Because brain tissue is comprised of cells, extracellular matrix, water, mobile ions, and fixed negative charges from macromolecules such as DNA and proteoglycans, it may behave like a triphasic material. Triphasic materials can swell because exposure of negative fixed-charge densities (FCD) attached to the porous solid matrix attract positive ions and increase the osmolarity of the space within the solid matrix. In a normal, healthy brain cell, Na^+/K^+ pumps use energy from ATP to pump cations out of the cell, thus leaving the FCD without counter ions. In effect, the FCD inside a healthy cell is, underhydrated and shrunken. The plasma membrane shields intracellular FCD from excess cations in the external environment. However, when brain cells die due to ischemic damage or mechanical damage, the counteractive force of the Na^+/K^+ pumps cannot adequately pump out cations to the external environment, thus allowing these external cations to rush into the cell as they are attracted to the opposite charge of the FCD within the matrix of the cell, thereby increasing the osmolarity of the intracellular environment. Water then rushes into the cell due to the difference in osmolarity between the internal and external

environment of the cell, causing the matrix of the interior of the cell to swell. The resulting Gibbs-Donnan swelling pressure can be determined by Equation 1, where p is the interstitial fluid pressure, R is the universal gas constant, θ is the absolute temperature in the tissue and bath, and p_* and c_* respectively represent the ambient pressure and osmolarity of the external bath fluid. Cartilage has been shown to swell in accordance with triphasic mixture theory [19], so brain swelling during cytotoxic edema may follow the same mechanism.

Elkin *et al.* has provided evidence that cell death and subsequent exposure of intracellular FCD may cause brain swelling by showing that application of either Triton X-100 or cyanide + 2DG to brain tissue (to either increase porosity of cell membranes or reduce Na^+/K^+ pump activity, respectively) increased brain tissue volume [20]. This same study also showed that adequate oxygenation of slices in aCSF supplemented with glucose drastically mitigated swelling compared to dying slices, providing evidence that the degree of FCD exposure was proportional to the amount of cell death and that the FCD responsible for swelling (when exposed to the extracellular environment) was intracellular. Furthermore, Elkin *et al.* has provided additional evidence that triphasic swelling biomechanics is responsible for water intake into the brain cell internal environment by demonstrating decreases in brain tissue swelling when using various enzymes to cleave FCDs within the brain tissue *in vitro* [21].

Although these two studies conducted by Elkin et al. have demonstrated that cellular FCD exposure during brain cell death is responsible for brain swelling, no study to our knowledge has provided direct evidence that FCD exposure due to cell death leads to increased brain swelling pressure, and no study to our knowledge has calculated FCD content of brain tissue by measuring confined swelling pressure of brain. In this study, a custom device was constructed to measure the confined swelling pressure of rat brain samples to calculate its FCD

content and show that the application of FCD-cleaving enzymes, which may act as a future therapeutic for brain swelling, reduces swelling pressure. We also measured the FCD content of cortex white matter and cortex gray matter of pig brain tissue to determine if FCD content differs between the two regions. Knowing the true FCD content of brain tissue may aid in computational modeling of cerebral edema by predicting the pattern and magnitude of brain swelling using principles from triphasic swelling biomechanics.

3.2 Methods

3.2.a Confined Swelling Pressure Device Construction and Data Processing

A custom device (Figure 8) was built to measure the confined swelling pressure of brain tissue to calculate FCD content. The purpose of the device was to measure the swelling pressure of a brain tissue sample under confined conditions, while still allowing exchange of water and ions between the tissue sample and external bath, so that FCD could be calculated without interference of volume change as the solid matrix deforms. A stainless steel cylindrical confined chamber (Figure 9) with a diameter of 4.79 mm and depth of 1.6 mm was machined to hold the brain sample. The confined chamber containing the brain sample was placed inside a reservoir and fully submerged in Gey's solution (Sigma-Aldrich, catalog number G9779-6X500ML) of known osmolarity. The reservoir was placed on an aluminum platform that sat on top of a 250 gram miniature load cell (Honeywell, model 31 Low, range code AN) which gathered load data and sent it to a signal conditioner/display (Honeywell, Model GM) which then sent the data to an A/D board (National Instruments, USB-6210) that was visualized and read on a custom LabVIEW VI at 5 Hz. A digital step drive (Geckodrive, catalog number G213V) was controlled using a custom LabVIEW virtual instrument (VI) to control a stepper motor (Anaheim

Automation, catalog number 23Y004D-LW8) powered using a power supply (Acopian, part number B24G170) to move a linear actuator (Deltron, catalog number L-RSA3-75-B02-EH-NPN-1-X) which lowered a sintered, porous indenter (diameter of 4.77 mm) from the top of the confined chamber until it was flush with the brain sample inside. The porous indenter allowed for transport of water and ions between the tissue sample and the external bath in the reservoir while constraining the volume of the brain sample. An LVDT (Harold G. Schaevitz Industries, The Sensor Connection, part number T-812-A-100) was used to ensure that the porous indenter was not displaced during the duration of the experiment as the brain sample attempted to swell within the confined chamber. Data from the LVDT was entered into a signal conditioner (TE Connectivity, part number ATA-2001) which then sent the processed data into the A/D board (National Instruments, USB-6210) that was visualized using a custom LabVIEW VI. To eliminate high-frequency noise, a low-pass filter (with a cutoff frequency of 0.15 Hz) was applied with zero-phase shift. The filtered data was then subjected to a moving average calculation over a window of 300 data points. Finally, the data was down-sampled every 600 data points to obtain the final trace of swelling. Our data processing technique, which sampled one data point every two minutes, provided sufficient resolution to capture the swelling pressure profile over time.

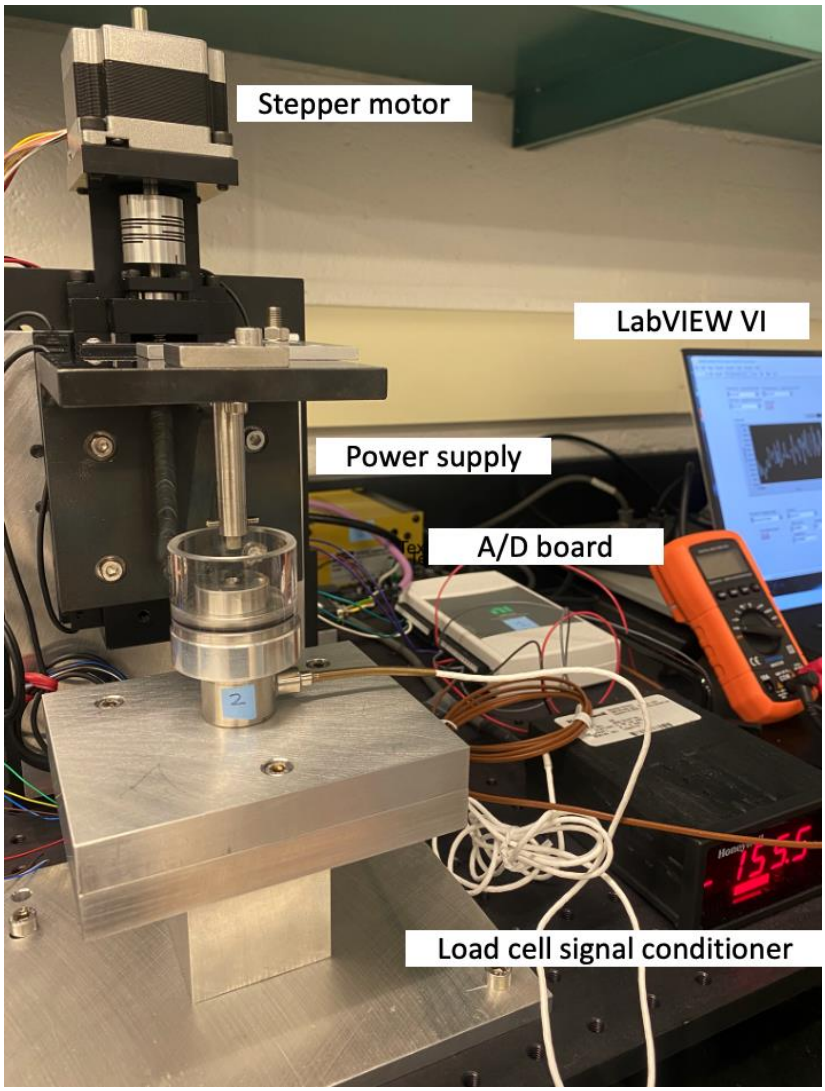

Figure 8: Assembly of our device's mechanical parts.

3.2.b Brain Isolation Procedures

All animal procedures were approved by the Institutional Animal Care and Use Committee (IACUC) of Columbia University. Rat experiments were conducted to test the efficacy of using FCD-cleaving enzymes in reducing swelling pressure to substantiate the role of the FCD. Adult Sprague-Dawley rats (Taconic) were deeply anesthetized with isoflurane, decapitated, and the brain removed as quickly as possible. Pig experiments were conducted to

determine the difference in FCD between white matter and gray matter of the cortex. Yorkshire pigs (Animal Biotech Industries) between 40-50 kg were sedated with telazol followed by propafol, then euthanized with euthasol. The skull was rapidly removed, the brain removed, and coarsely blocked into samples approximately 5-10 mm thick.

After this stage, samples of either rat of pig brain were treated identically. The bottom of the tissue sample was superglued to a Petri dish, and ice-cold artificial cerebrospinal fluid (aCSF, 125 mM NaCl, 3.5 mM KCl, 26 mM $NaHCO_3$, 1.2 mM KH_2PO_4, 1.3 mM $MgCl_2 \cdot 6H_2O$, 2.4 mM $CaCl_2$, 10mM HEPES, 4.5% glucose) equilibrated with 95% O_2 / 5% CO_2 submerged the tissue. 500 μm sections were cut with a vibratome (Series 1000 Classic). A 5 mm diameter biopsy punch (Miltex, model 33-35) was used to cut cylindrical samples of tissue, which were then placed into a stainless steel confined chamber (Figure 9).

3.2.c Measuring FCD

After the tissue sample was placed into the pressure chamber, the chamber was placed into the reservoir shown in the experimental device (Figure 9). 9 mL of oxygenated Gey's solution (Thermo Fisher Scientific, catalog number J67569-K2) supplemented with 4.5% glucose was placed into the reservoir, submerging the confined tissue. The load served as the baseline reading for calculating swelling pressure and therefore FCD. The porous indenter was aligned with the pressure chamber and lowered until a load of at least 20 grams was achieved, indicating that the indenter was in good contact with the tissue. By doing so, the tissue sample was fully constrained, and the porous indenter was completely engaged with the tissue. Stress-relaxation was allowed to occur for 10 minutes after which 1 mL of Gey's solution with Triton X-100 was added to a final concentration of 0.5%. Triton X-100 accelerated cell death and maximized

exposure of the intracellular FCD. The temperature of the solution in the bowl was measured with a thermocouple. The sample was left for 16 hours and swelling pressure was monitored for the entire duration.

Swelling pressure was measured as the difference between the maximum swelling load minus the weight of the set-up prior to the tare load (we assumed the tare load relaxed to 0 grams in each case) divided by the cross-sectional area of the porous indenter. With known values of swelling pressure, temperature, and concentration of counter ions in the external solution, the FCD was calculated using Equation 1.

To test whether brain swelling was due to gradual intracellular FCD exposure as the tissue died, some samples of rat brain tissue were placed in the confined chamber which was fully submerged in Gey's solution, supplemented either with or without glucose, with 0.5% Triton X-100 for at least two hours in an effort the completely kill the tissue. The swelling pressure of these intentionally poisoned samples were then measured and compared to the control group.

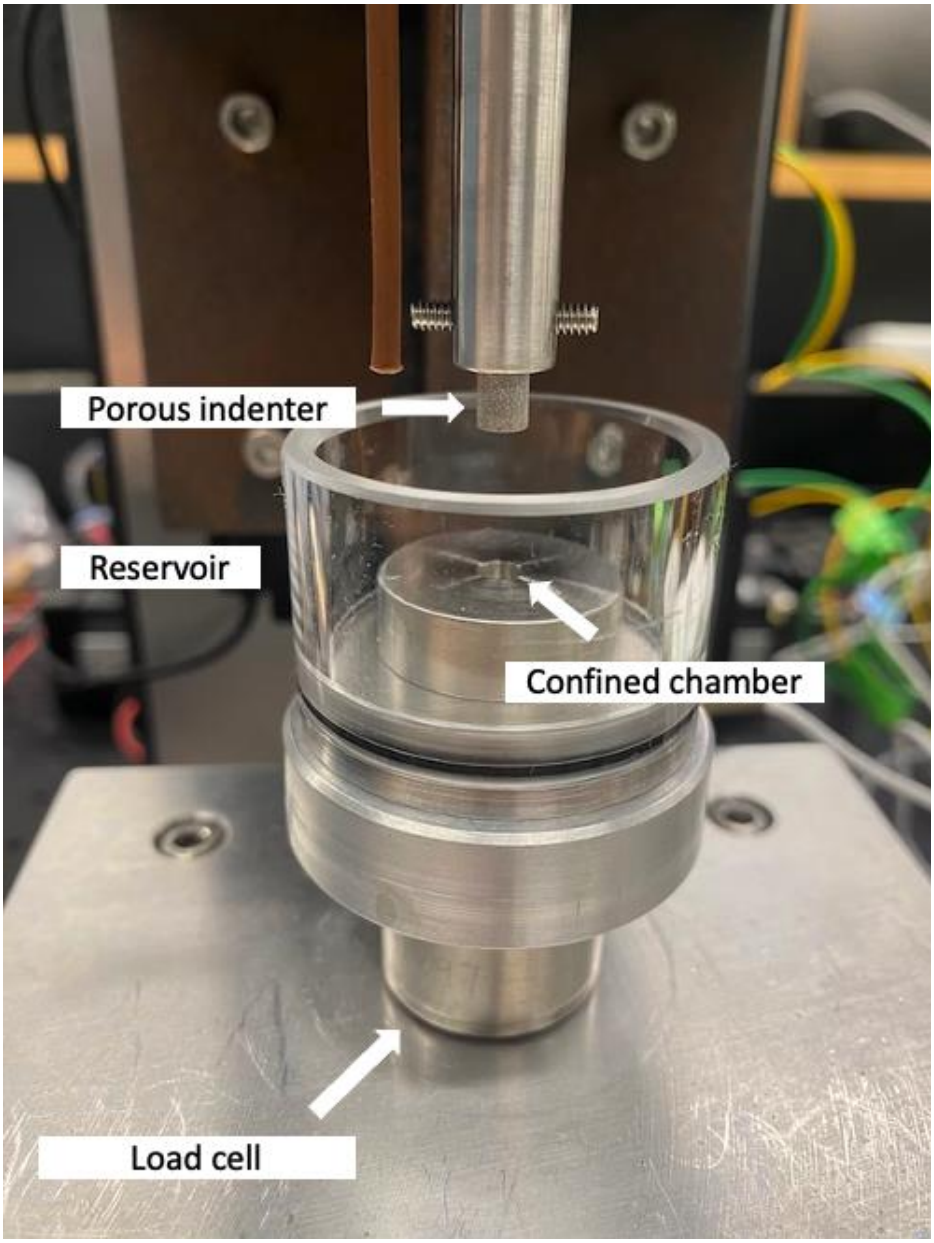

Figure 9: Description of vital parts of experimental set-up. The sample of brain sits inside the confined chamber and the reservoir is filled with Gey's solution. A porous indenter is slowly lowered until it contacts the brain tissue. As the tissue swells, the load is measured by the load cell underneath.

3.2.d FCD-cleaving Enzymes

FCD-cleaving enzymes were added to a subset of rat brain samples prepared identically as the control group, with the addition of a cocktail of four enzymes: DNase (Sigma-Aldrich,

catalog number 10104159001), heparinase I (Sigma-Aldrich, catalog number H2519-50UN), heparinase III (Sigma-Aldrich, catalog number H8891-10UN), and chondroitinase ABC (Sigma-Aldrich, catalog number C3667-10UN) at concentrations of 1.5 mg/mL, 0.2 units/mL, 0.2 units/mL, and 0.2 units/mL, respectively, to digest the FCD and reduce the swelling pressure. The enzymes were mixed with the 9 mL of Gey's solution that was added immediately into the external reservoir to submerge the confined chamber containing the brain tissue sample prior to application of the tare load using the porous indenter.

3.2.e FCD Measurements as a Function of Post-mortem Time

Brain samples from Sprague-Dawley rats were removed and samples were isolated in the same fashion described previously, but using 1 mm thick samples. Samples were placed in oxygenated Gey's solution (Sigma-Aldrich, catalog number G9779-6X500ML) at room temperature for various amounts of time following dissection. Swelling pressure and FCD were measured as described previously. Either Triton X-100 at 0.5% concentration or 5mM sodium cyanide + 10 mM 2-deoxyglusose (2DG) were used to poison the tissue.

3.3 Results

3.3.a FCD Content of Rat Brain

Maximum FCD was calculated using the measured maximum swelling pressure of the tissue sample. The maximum FCD value for rat brain in the control group was 42.6 ± 2.7 mEq/L and the maximum FCD value for rat brain tissue treated with the enzyme cocktail was 40.5 ± 2.5 mEq/L (Figure 10). The maximum FCD value was not statistically significant between groups.

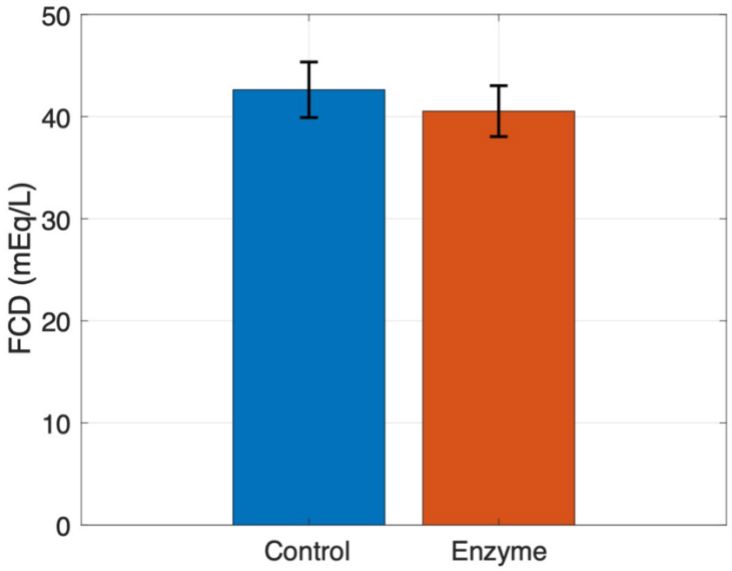

Figure 10: Comparison of maximum FCD between the control group and enzyme treated group. N = 9 for both groups. The maximum FCD between the two groups was not statistically different ($p > 0.05$). Mean ± standard error of the mean (SEM).

3.3.b Effect of FCD-cleaving Enzymes

In Figure 11, FCD content over time is presented for the control and enzyme treated groups. The swelling pressure in the treated group decreased faster after reaching its peak compared to the control group. The faster reduction of swelling pressure, and hence FCD, in the enzyme-treated group lead to significantly lower measurements of FCD content at 16 hours post-dissection when compared to the control group (Figure 12).

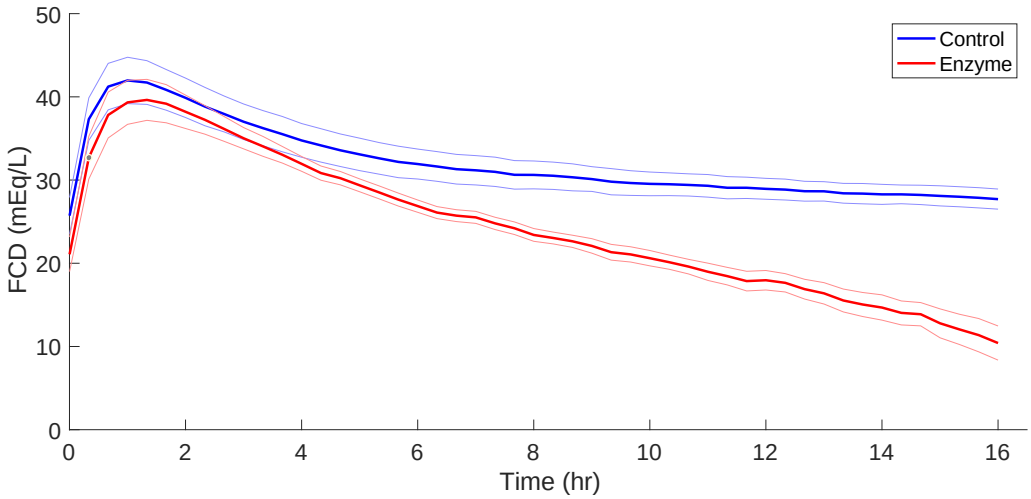

Figure 11: Comparison of FCD as a function of time between the control group (Gey's solution + Triton X-100) and the enzyme treated group (Gey's solution + Triton X-100 + enzyme cocktail). N = 9 for both groups. The load and FCD of the group treated with an enzyme cocktail was reduced compared to the untreated group at 16 hours. The corridors designate ± SEM.

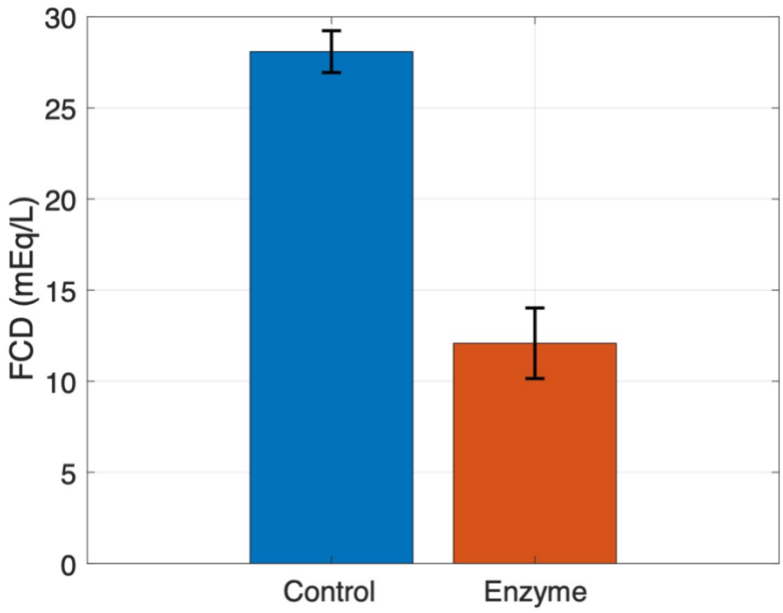

Figure 12: The FCD was significantly lower in the enzyme treated group compared to the control group after 16 hours ($p < 0.05$). Mean ± SEM.

3.3.c FCD Content of Pig Brain

The total FCD of pig cortex gray matter was 36.5 ± 1.7 mEq/L while the total FCD of pig cortex white matter was 16.0 ± 2.5 mEq/L (Figure 13). The difference in total FCD between white and gray matter was statistically significant ($p < 0.01$).

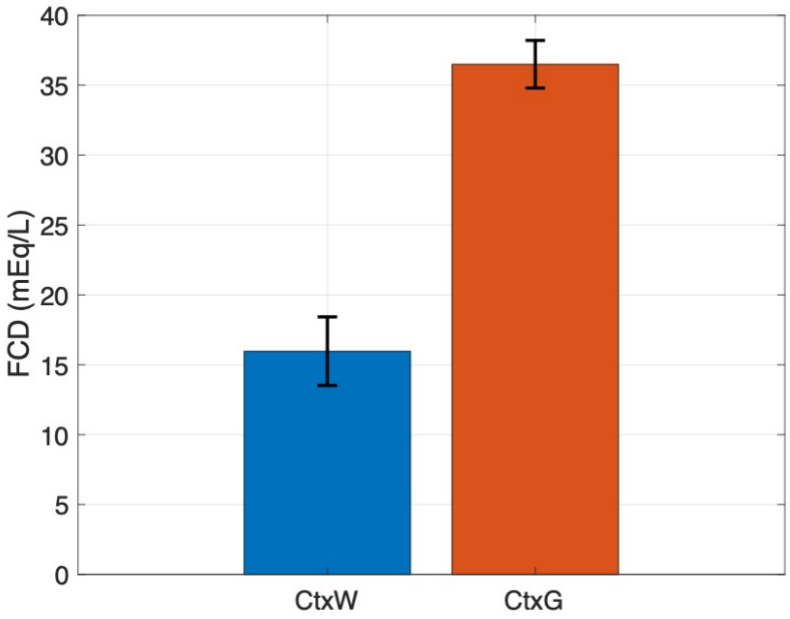

Figure 13: Comparing total FCD between cortex white matter (CtxW) and cortex gray matter (CtxG). N = 6 for both groups. Total FCD of cortex gray matter was significantly greater than that of the cortex white matter ($p < 0.01$).

3.3.d Relationship Between FCD and Post-mortem Time

Figure 14 and Figure 15 show the relationship between FCD and time post-mortem of brain tissue samples incubated in oxygenated aCSF at room temperature, when Triton X-100 or Cyanide + 2DG were used to kill the tissue, respectively. FCD content decreased between 15 minutes post-dissection and 1 hour post-dissection, but FCD content between 1 hour and 6 hours post-dissection was not significantly different.

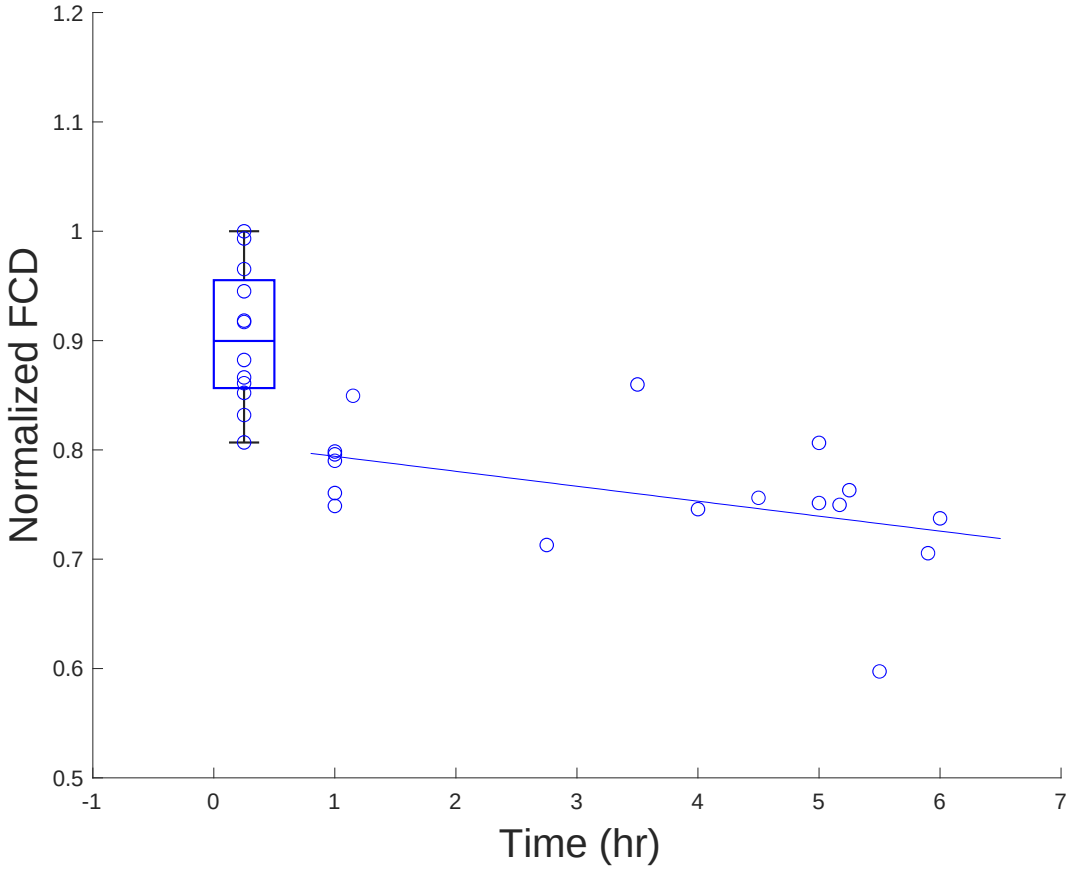

Figure 14: FCD as a function of post-mortem time. Brain slices sitting in oxygenated aCSF at room temperature produced less swelling pressure at longer post-mortem times compared to samples tested immediately post-mortem due to lesser amounts of FCD leftover to be exposed as the tissue died gradually over time. Triton X-100 was used to kill tissue.

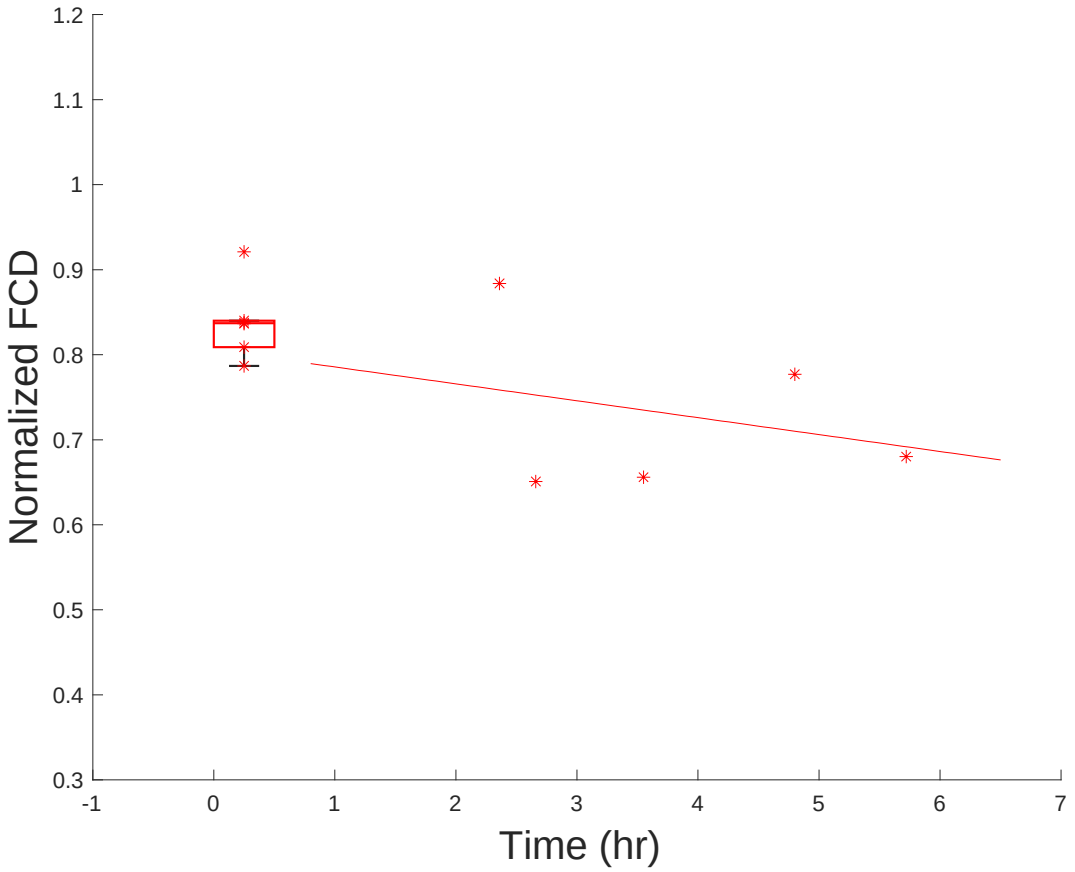

Figure 15: FCD as a function of post-mortem time. Brain slices sitting in oxygenated aCSF at room temperature produced less swelling pressure at longer post-mortem times compared to samples tested immediately post-mortem due to lesser amounts of FCD leftover to be exposed as the tissue died gradually over time. Cyanide + 2DG was used to kill tissue.

Figure 16 shows a comparison of swelling pressure of the control group and experimental group treated with a cocktail of FCD-cleaving enzymes to a separate group of tissue samples designated as the "dead tissue" group that were intentionally poisoned in Gey's solution with 0.5% Triton X-100 prior to testing using our device. Using Gey's solution either with or without supplemented glucose had no noticeable effect on measured swelling pressure in the "dead tissue" group. The lack of any increase in swelling pressure in the "dead tissue" group indicates

that the tissues were dead and had exposed all of their intracellular FCD prior to being tested using our device.

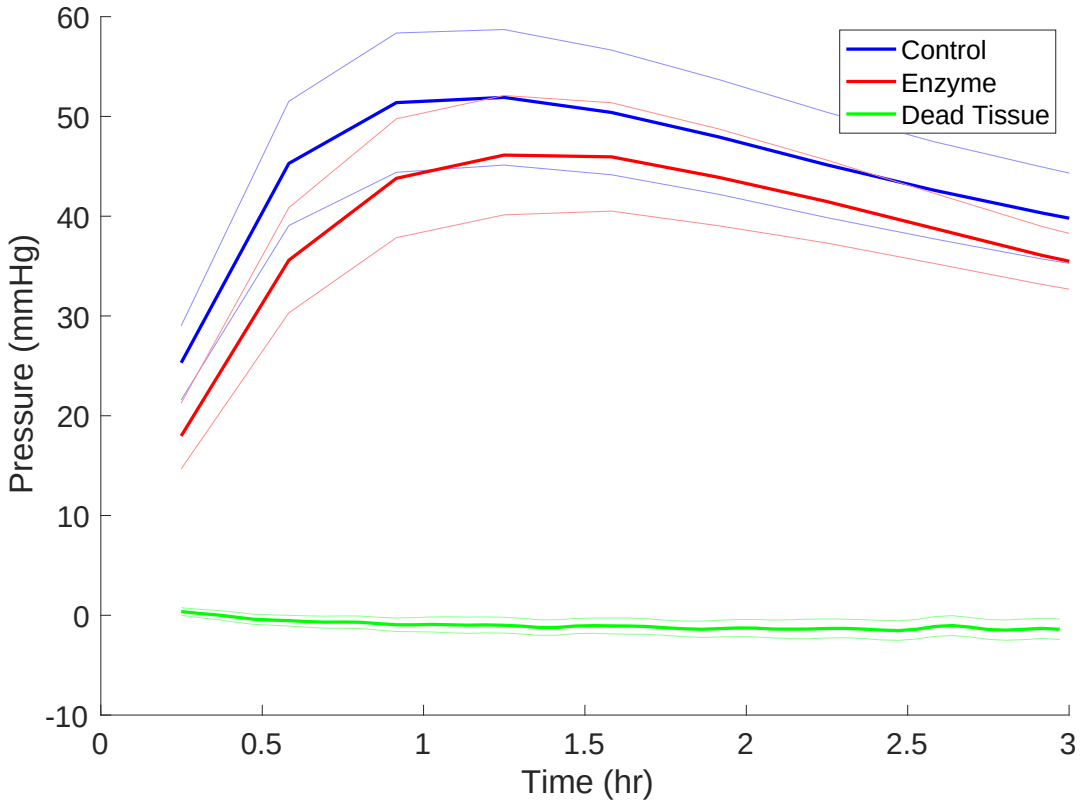

Figure 16: Rat tissue samples that were placed in the confined chamber and submerged in Gey's solution (supplemented with or without glucose) with 0.5% Triton X-100 for at least 2 hours prior to testing with our device showed no increase in swelling pressure, indicating that slices were dead and fully swollen prior to being tested. Sample sizes are n = 9 for both the control and enzyme groups, while n = 10 for the dead tissue group. Data is plotted starting at 15 minutes following tare load.

3.4 Discussion

Cerebral edema is one of the worst consequences following TBI and is responsible for many deaths and disabilities following head injury. There is no current consensus as to what the exact mechanism for cerebral edema is. Current clinical treatments lack significant efficacy and may lead to various complications. Therefore, the purpose of this study was to propose a

potential mechanism for cerebral edema, offer a potential treatment option that may be clinically viable in the future, and differentiate the amount of FCD between cortex white matter and cortex gray matter of the brain.

In this study, we calculated the FCD value of rat brain tissue using the Gibbs-Donnan equation (Equation 1). Maximum swelling pressure occurred within 1-2 hours. After reaching maximum swelling pressure, the pressure slowly began to decrease, reflected in the reduction of calculated FCD over time (Figure 11). The rise in swelling pressure, and thus the rise in measured FCD exposure, may have been due to a combination of two factors: 1) the relatively quick FCD exposure due to cell death from brain cells that were already damaged on the tissue sample due to cutting from the Vibratome and 2) the quick FCD exposure due to brain cells lysing due to contact with Triton X-100. In a study conducted by Elkin *et al.*, brain tissue slices in Gey's solution with 0.5% Triton X-100 experienced a significant increase in volume compared to brain tissue slices in Gey's solution without Triton X-100 when observed 30 minutes following dissection, indicating that Triton X-100 had already diffused through the tissue to kill enough cells to significantly increase the rate of swelling within that 30 minutes. The slices used in our study were 500 μm instead of 350 μm used in Elkin's study, but should have been thin enough where diffusion of Triton X-100 through our samples would accelerate the rate of cell death, maximizing FCD exposure within the first 1-2 hours. The subsequent decrease in swelling pressure and calculated FCD content in the control group following peak swelling pressure may have been due to a variety of factors, one being diffusion of FCD from the tissue sample into the external bath as endogenous proteases may cleave FCD as brain cells die.

The average calculated FCD of rat brain tissue in this study was higher than the FCD content of brain (5.88 mEq/L) measured by Elkin *et al.* in which a standard 1,9

dimethylmethylene blue (DMMB) assay was used to measure glycosaminoglycan (GAG) content [20]. One limitation of using a DMMB assay is that it binds to sulphated GAGs and can therefore only be used to measure sulphated GAGs that contribute to the FCD content of the brain. However, FCD content can also come from other contributions such as DNA, proteins, and other matrix molecules [20] which may not be detected using a DMMB assay. The advantage of our experimental set-up is that it allows for calculation of FCD content regardless of the constituents of the total FCD within the brain sample. One possible reason that the FCD content of rat brain tissue calculated in this study is higher than the FCD content measured by Elkin *et al.* is that rat brain tissue might have significantly higher levels of FCD that are not GAGs, so using a DMMB assay to measure FCD may severely underestimate the true amount of FCD content within tissue. Although the DMMB assay has be used to successfully measure FCD values for comparison to FCD predictions in tissues modeled as triphasic mixture materials [20, 106, 107], this may be because GAGs make up a large percentage of the FCD constituents in cartilage and aorta, which may be different for brain tissue. An FCD measurement of 5.88 mEq/L as measured in the study by Elkin *et al.* would generate confined swelling pressures much less than what was observed in this current study.

When comparing the swelling pressure over time between the control group and experimental group treated with FCD-cleaving enzymes, the experimental group experienced a significantly faster rate of decrease. The addition of enzymes to digest likely constituents of the FCD significantly lowered the swelling pressure in rat tissue, providing evidence that brain swelling is caused by exposure of intracellular FCD. The motivation for using enzymes to cleave FCD was to reduce the c^F (FCD) term in Equation 1 to reduce the Gibbs-Donnan osmotic pressure responsible for driving water intracellularly. A reduction in the Gibbs-Donnan osmotic

pressure reduced the magnitude of the pressure gradient responsible for driving water into the cells, thus reducing the measured swelling pressure. DNase, heparinase I, heparinase III, and chondroitinase ABC were chosen for our experiment because these enzymes caused a reduction in brain swelling volume in a study conducted by Elkin *et al.* [21]. DNase digests DNA which contain negatively charged phosphate ester groups [108, 109]; heparinase I and III digest heparin sulfate proteoglycans which contain an arrangement of negatively charged sulfate groups [110], and chondroitinase ABC digests chondroitin sulfate proteoglycans which also contain an arrangement of negatively charged sulfate groups [111]. Brain samples in both the control group and enzyme treated group experienced swelling followed by shrinking. Pressure in the control group began to decrease after ~1-2 hours following loading of the sample into our test device, perhaps indicating that endogenous processes were degrading FCD causing them to diffuse into the external bath. However, pressure generated by samples in the enzyme treated group decreased at a faster rate compared to the control group, providing strong evidence that cleavage of FCDs was responsible for accelerating the decrease in swelling pressure. This study, which shows a reduction in swelling pressure after application of FCD-cleaving enzymes, in conjunction with a study conducted by Elkin *et al.* which showed a decrease in swelling volume of swollen brain slices after application of the same FCD-cleaving enzymes, provides strong evidence that FCD exposure during cell death is the driving force of cerebral edema.

Interestingly, despite the decrease in swelling pressure and calculated FCD content within the control group, the FCD content did not drop to zero. One possible explanation is that the breakdown of FCD due to endogenous enzymes created large fragments of negatively charged molecules that leached out of the tissue and into the external bath, but over time, the porosity of the solid matrix of the brain decreased as these fragments accumulated within the pores of the

solid matrix. The reduction in porosity would prevent the leaching out of additional large fragments of negatively charge molecules into the external bath, which would maintain the osmotic gradient necessary to sustain swelling pressure at a non-zero value. The reduction in porosity could also affect hydraulic permeability, as small variations in porosity have been shown to cause significant changes in hydraulic permeability in cartilage [112], which could also significantly inhibit water movement from the inside of the brain tissue sample into the external bath, thus reducing the rate of swelling pressure decrease. Another possible explanation as to why swelling pressure and FCD did not decrease to zero in the control group is because some FCD were not cleaved by endogenous enzymes and remained attached to the solid matrix of the brain, thus contributing to the osmotic gradient required to sustain pressure. Swelling pressure and calculated FCD content in the enzyme-treated group, however, seemed to continually decrease. The enzyme-treated group was treated with a cocktail of four different enzymes targeting DNA, chondroitin sulfate proteoglycans, and heparin sulfate proteoglycans, which may have caused a majority of the total FCD content within the samples to break down. This cocktail of enzymes may have cleaved large, macromolecular FCD (either from the solid matrix itself or from residual large molecular fragments accumulating within the pores of the solid matrix due to activity of endogenous enzymes) into much smaller molecules which would allow them to diffuse out from the sample and into the external bath easier. Chondroitinase ABC is a bacterial enzyme that degrades chondroitin sulfate proteoglycans by cleaving glycosaminoglycan chains into disaccharides or tetrasaccharides [113], and heparinases cleave polysaccharides into disaccharides and oligosaccharides [114], all of which may be able to easily diffuse into the external bath due to their relatively small sizes.

The maximum swelling pressure, and thus maximum FCD value, were not significantly different between the control group and the enzyme treated group (Figure 10). One possible explanation is that the enzymes in the experimental group required more time to diffuse through the porous indenter and throughout the thickness of the sample than the time required for the tissue sample to reach maximum swelling pressure. Cations and water are substantially smaller than these enzymes (chondroitinase ABC is ~120 kDa, heparinase I is ~43 kDa, heparinase III is ~73.5 kDa, and DNase is ~ 30 kDa) and are able to diffuse much faster through the porous indenter and the brain tissue sample, which may be the reason why the maximum swelling pressures for both groups were not significantly different. Therefore, it was necessary to wait for several hours after maximum swelling pressure was reached for the enzymes to diffuse through the porous indenter and into the tissue sample before a difference in swelling load was observed.

The measured maximum FCD value for pig brain gray matter tissue was lower than that of rat perhaps because it took longer, on average, to extract pig brain and obtain a sample to test in our device compared to rat brain. Brain isolation procedures for pigs took longer than for rats because pig skulls were difficult to cut, extending the time required for removing the brain. Pig brain tissue was also more difficult to manipulate than rat brain tissue using the vibratome, causing more time to elapse before it could be placed inside the confined chamber. There is some evidence that pig gray matter may have more FCD than rat gray matter [21] and that neuronal density might scale with brain mass [115] indicating that pigs might have higher neuronal density and FCD than rats, so the extra time needed to obtain brain samples from pig may have caused a greater degree of cell death, and hence FCD exposure, prior to testing, which would have lowered the measured maximum FCD value for pig compared to rat.

When comparing the swelling pressure of pig cortex gray matter to pig cortex white matter, pig brain gray matter swelled more, indicating higher levels of exposed FCD over time. Brain FCD consists of molecules such as chondroitin sulfate proteoglycans, heparin sulfate proteoglycans, and DNA, with chondroitin sulfate proteoglycans and heparin sulfate proteoglycans especially present predominantly within the cell cytoplasm [21]. Because gray matter is comprised mainly of neuronal cell bodies, dendrites, and glia while white matter is comprised of mostly myelin and highly oriented axon tracts [53], there may be larger amounts of cellular cytoplasm in gray matter, indicating larger amounts of FCD in gray matter compared to white matter. Myelin, a constituent of the brain that is only present in white matter, has little to no chondroitin sulfate while neuronal cell bodies, axons, and astrocytes contain significant amounts [116, 117]. In rodents, astrocytes in white matter have small cell bodies while astrocytes in the gray matter are typically larger [118], meaning that there might be more cellular biomass of astrocytes in gray matter than white matter. This difference in morphology may also be present in pigs and humans. Since astrocytes contain large amounts of chondroitin sulfate, and perhaps other sulfate proteoglycans, FCD content may be more abundant in gray matter compared to white matter.

Figure 14 and Figure 15 show FCD as a function of post-mortem time. Brain samples placed in room temperature oxygenated aCSF for longer periods of time (>1 hour) produced lower swelling pressures than brain samples that were tested as soon as possible post-mortem (~15 minutes post-dissection) and thus contained less leftover FCD to be exposed, since cells that were dying while sitting in the aCSF were already swelling due to exposure of the FCD which was neutralized by cations in the surrounding bath. After one hour post-dissection, measured FCD already decreased noticeably compared to samples tested approximately 15

minutes post-dissection, despite attempting to keep tissue alive by placing it in oxygenated aCSF, indicating that testing the tissue sample immediately following dissection was necessary.

To demonstrate that swelling pressure and FCD content were dependent on cell viability, we measured the swelling pressure of rat brain tissue samples that were intentionally poisoned for at least 2 hours in Gey's solution with 0.5% Triton X-100 prior to testing. Swelling pressure was nearly non-existent in this experimental group, indicating that all FCD had already been exposed and that the tissues had already fully swelled, as opposed to the samples in the control group that were tested immediately post-dissection and still contained FCD which had not been fully exposed yet (Figure 16). This result, coupled with data from Elkin *et al.* which showed that 350 μm thick rat brain samples given sufficient oxygen and energy supply swelled minimally for 2 hours post-dissection, supports that FCD exposure and subsequent brain swelling is caused by the cell death process.

Our study did have some limitations. The calculated total FCD value for rat brain tissue (Figure 10) may not be the total FCD within the tissue. As cells in brain tissue die, they begin to expose the intracellular FCD, leading to swelling [20]. Immediately after euthanizing the rat, brain cells may begin to die because the heart is no longer pumping oxygen and nutrients to the brain. The process of extracting the brain, obtaining an adequately-sized test sample, placing the sample into the pressure chamber, and lowering the porous indenter onto the sample could only be achieved, at best, within 15 minutes. This time frame may be long enough for some brain cells to die and expose their FCD prior to the start of the experiment, causing premature swelling of the tissue sample, and leaving some FCD undetectable by our experimental paradigm. A study by Elkin *et al.* demonstrated that samples of rat brain cortex 350 μm thick experienced a slight change in volume 15 minutes following dissection, indicating that some brain cells may

have been dying even within 15 minutes after euthanasia. Indeed, cerebral ischemia has been shown to trigger neuronal death within as little as 5 minutes [119], compared with a substantially longer period of 20-40 minutes for cardiac monocytes or kidney cells [120]. If brain cells within the tissue sample began to die prior to the start of measurement by our device, the true total FCD content of the sample may be higher than what we reported experimentally.

Another factor to note when interpreting the total FCD content is that the FCD may be digested by endogenous enzymes, allowing it to diffuse out of the tissue and into the external bath. The brain tissue samples used in our experiments died from a combination of ischemic injury due to lack of oxygenation of the external bath and application of Triton X-100 to destroy cell membranes. Ischemia has been shown to induce catabolic necrosis in brain tissue in as little as 5 minutes after a complete lack of oxygen and glucose [121]. Necrosis due to ischemic injury leads to the degradation and fragmentation of DNA by various proteases and endonucleases [122]. These DNA fragments, which contain a negative charge per nucleotide base at its sugar-phosphate backbone [123], could diffuse out of the tissue and into the external bath, decreasing the total amount of calculated FCD within the tissue sample as the tissue dies. The premature digestion of the FCD by endogenous enzymes prior to the death of all cells within the tested tissue sample may underestimate the true FCD content of the tissue sample by reducing the peak pressure obtained during the experiment. One way to possibly circumvent this issue is to apply a cocktail of enzyme inhibitors to the sample in future experiments to slow the rate of natural, endogenous processes that break down the FCD or to use a heated external bath to denature any endogenous enzymes within the tissue sample.

In summary, this study demonstrated that exposure of intracellular FCD during cell death caused brain swelling, and that application of FCD-cleaving enzymes reduced brain swelling

pressure, which could aid in the development of novel therapies to treat cerebral edema in the future. This study also distinguished differences in FCD content between pig cortex gray matter and cortex white matter, which is important if cerebral edema is to be modeled within FE head models that simulate swelling based on triphasic swelling biomechanics such as that demonstrated in a study by Basilio *et al* [124]. Coupled with data from Elkin *et al.,* the results in this study provide additional evidence that exposure of intracellular FCD during cell death is a potential driving mechanism of cerebral edema. Despite the interesting findings in this study, the total FCD content of human brain tissue remains unknown. The difference in FCD content between cortex gray matter and cortex white matter in pig reveals that FCD content in the human brain may also vary by region. Future work should therefore be conducted to measure the FCD content of freshly procured different regions of the human brain.

Chapter 4: Simulating Cerebral Edema and Delayed Fatality After Traumatic Brain Injury Using Triphasic Swelling Biomechanics[1]

4.1 Introduction

Traumatic brain injury (TBI) is a major contributor of mortality and morbidity after motor vehicle crashes (MVCs). Between 1995-2001, 20% of annual TBI-related emergency department visits, hospitalizations, and deaths were attributed to MVCs [125]. In 2013, 21.5% of TBI-related hospitalizations were attributed to MVCs [4]. In the quest to reduce the societal costs of MVCs, finite element (FE) models have contributed to our understanding of injury causation as well as aided in the design of improved safety systems for both occupants and vulnerable road users. A family of FE models has been developed by the Global Human Body Models Consortium (GHBMC) that includes structures of the entire human body, including a detailed mesh of the head and brain. The GHBMC model has been validated at both the component and whole-model levels to support its biofidelic, dynamic response [126, 127]. The current use of FE models in the automotive industry focuses on predicting stress and strain during the accident itself to predict primary injury; contemporary models have not been used to simulate delayed brain swelling from edema that occurs after the impact on the time-scale of hours to days. Over 70% of severe TBI patients (GCS $\leq$ 8) experience cerebral edema leading to increased intracranial pressure (ICP), and elevated ICP is highly associated with poor outcome

[1] A modified version of this chapter was previously published and is reproduced here with permission: Basilio, A. V, Xu, P., Takahashi, Y., Yanaoka, T., Sugaya, H., Ateshian, G. A., Morrison III, B. (2019). Simulating Cerebral Edema and Delayed Fatality After Traumatic Brain Injury Using Triphasic Swelling Biomechanics. *Traffic Inj. Prev.*

and increased mortality [128]. By simulating cerebral edema, it may be possible to improve prediction of mortality during this sub-acute phase to inform the design of novel safety systems.

Brain tissue, like most biological tissue, is composed of approximately 80% water and 20% solid matrix. The solid matrix within cells is comprised of material with an inherent negative charge (proteins, glycosaminoglycans, DNA, etc.), represented by the concept of a fixed charge density (FCD). The intracellular and extracellular space are separated by the plasma membrane. Embedded within that plasma membrane are sodium-potassium pumps that, under homeostatic conditions, expend significant energy to remove net positive charges from the inside of the cell, maintaining a negative transmembrane potential. Under resting conditions, we hypothesize that the FCD is under-hydrated because of this charge imbalance, which has major implications for brain swelling after injury.

When cerebral blood supply is reduced such that the ion pumps no longer function or when the plasma membrane becomes compromised due to a mechanical insult, the intracellular FCD becomes exposed to the extracellular environment. Because these fixed charges are integral to the structural components of the cell, they are not free to diffuse. Rather, the FCD attracts positive ions, leading to a higher osmolarity in the matrix relative to the fluid phase [20, 21]. The resulting osmotic potential attracts water, thereby swelling the matrix, according to the Gibbs-Donnan theory.

We hypothesize that the degree of FCD exposure is related to cell death and that cell death is dependent on the maximum principal strain (MPS) experienced by tissue during impact, as is often assumed in FE modeling [77, 129-132]. As cells die, we hypothesize that the FCD is exposed, and tissue swells. Because the skull is rigid, areas of the brain that experience swelling compress adjacent regions. In turn, the vasculature is also compressed, thus decreasing cerebral

blood flow (CBF) to that area [133]. If CBF is reduced sufficiently, the lack of energy supply compromises the function of sodium-potassium pumps or leads to ischemic cell death, exposing additional FCD and leading to additional swelling [134]. Taking this approach to simulate post-traumatic swelling in FEBio, we predicted a clinically relevant increase in ICP in a reconstruction of a fatal pedestrian MVC. With this capability to predict the degree of swelling after an injury, we believe there is potential to make cars safer by incorporating delayed mortality when testing safety systems *in silico* during the design and development phase.

4.2 Methods

4.2.a Triphasic Theory

Triphasic theory models a biological tissue as a mixture of a porous deformable solid matrix whose pore space is filled with an interstitial fluid consisting of water and two monovalent counter-ions (such as Na^+ and Cl^-). Each of these constituents is assumed to be intrinsically incompressible, although the porous solid matrix may gain or lose volume due to fluid transport into or out of the pore space (conceptually similar to a sponge). Thus, to account for pore volume variability, the porous solid matrix is modeled as a compressible hyperelastic material; the Cauchy stress tensor produced by the deformation of this solid matrix is denoted by $\boldsymbol{\sigma}^e$. The deformation gradient of the solid matrix is denoted by $\boldsymbol{F}$, and its determinant, $J = \det \boldsymbol{F}$, represents the solid matrix volume ratio (the ratio of solid matrix volume in the current and reference configurations). Recall that $J = 1$ in the reference configuration. The pore volume fraction in the reference configuration is denoted by φ_r^w. As the solid matrix deforms, this pore volume may increase or decrease; the value of the pore volume fraction in the current configuration is denoted by φ^w and related to φ_r^w via the axiom of mass balance

Equation 6

$$\varphi^w = \frac{J - 1 + \varphi_r^w}{J}$$

This relation shows that the smallest possible value of the solid matrix volume ratio is

Equation 7

$$J = 1 - \varphi_r^w$$

which occurs when the pores have completely closed and the interstitial fluid has completely exuded ($\varphi^w = 0$).

The interstitial fluid pressure is denoted by p, which is positive in compression, so that the total (or *mixture*) stress is

Equation 8

$$\boldsymbol{\sigma} = -p\boldsymbol{I} + \boldsymbol{\sigma}^e$$

This pressure represents the combination of osmotic and hydraulic effects. The molar concentrations of the monovalent counter-ions are denoted by c^+ and c^-. These molar concentrations are evaluated as moles of ion per interstitial fluid volume. In the triphasic theory, electrically charged molecular species may be bound to the solid matrix, imparting a fixed-charge density (FCD) to the solid. The FCD concentration in the reference configuration is denoted by c_r^F; it is evaluated with units of equivalent mole of a monovalent ion per volume of interstitial fluid, and its value is either negative or positive. As the pore volume changes with tissue deformation, the charge density changes accordingly, such that its value in the current configuration is given by the axiom of mass balance as

Equation 9

$$c^F = \frac{\varphi_r^w c_r^F}{J - 1 + \varphi_r^w}$$

This relation implies that complete pore closure ($\varphi^w \to 0$) is a limiting condition for which $|c^F| \to \infty$.

Since electroneutrality must be satisfied at every point in the mixture, the concentrations of ions inside the mixture are affected by the FCD, such that they differ from those in the surrounding fluid bath. The imbalance of ion concentrations between the interstitial and external fluids is called the Gibbs-Donnan effect; it produces an osmotic pressure difference between the interstitial fluid and external bath, called the Gibbs-Donnan pressure [135, 136]. Under steady-state conditions, when the fluxes of interstitial fluid and ions have subsided, the hydraulic pressure reduces to zero so that the only contribution to the interstitial fluid pressure p is the Gibbs-Donnan osmotic pressure, given by Equation 1 described previously where R is the universal gas constant, θ is the absolute temperature in the tissue and bath, and p_* and c_* respectively represent the ambient pressure and osmolarity of the external bath fluid. This expression was derived under the assumption of ideal physico-chemical conditions for mixtures containing two monovalent counter-ions. It is common to set $p_* = 0$, so that p represents the gage pressure.

The FEBio software can perform a triphasic analysis under transient or steady-state conditions [56]. Transient analyses can evaluate the time-dependent responses of the solid matrix deformation gradient $\boldsymbol{F}$, fluid pressure p, ion concentrations c^+ and c^-, as well as interstitial fluid and ion fluxes. However, only steady-state analyses were employed in the current study, thus producing steady-state solutions for $\boldsymbol{F}$, p, c^+ and c^-, based on the equations presented above as well as additional relations for the mixture momentum balance and boundary conditions for the ion electro-chemical potentials.

4.2.b Simulating Impact

A fatal vehicle-to-pedestrian impact was simulated from the Crash Injury Research & Engineering Network (CIREN), load case ID 06-053-P-1 with impact speed of 46 km/h. For a non-injury case, a time history (case number LX1507) was obtained from the NHTSA Biomechanics Test Database of head acceleration data from lateral sled tests (50-70 m/s^2) of human volunteers [137]. Details of the simulations using the GHBMC human model are given in [37] with the six-degree-of-freedom acceleration histories for the fatal case shown in Figures A2 and A3 in Basilio *et al* [124] (Figure 17 and Figure 18 in this thesis). The element deformation histories then served as inputs for the FEBio swelling simulations.

4.2.c FEBio Mesh

Because we were only interested in analyzing brain swelling, we extracted the skull and brain elements from the GHBMC model and imported them into FEBio (febio.org) [55, 56]. The FEBio model contained 24 brain parts; Table 5 lists the structures, material type, and material properties. Swelling elements were redefined as being triphasic ('multiphasic-fcd') in FEBio, while matching their original GHBMC Kelvin-Maxwell viscoelastic mechanical properties. To match the properties in FEBio, we used a multiphasic-fcd material with neo-Hookean properties for the solid fraction with a Poisson's ratio (ν) of 0 making the mixture compressible due to fluid movement. The Young's modulus (E) was matched to the original long-term shear modulus (G) with Equation 10. The long-time shear modulus was used because swelling is a slow phenomenon.

Equation 10

$$E = 2G(1 + v)$$

Table 5: Material properties of structures in the FEBio model.

Structure	Material	Density	Young's Modulus (kPa)	Poisson's Ratio	Beta
HE_OR_Cerebellum_3D	multiphasic-fcd	1060	2.4	0	
HE_OR_Cerebrum-Gray-Lower_3D	multiphasic-fcd	1060	2.4	0	
HE_OR_Cerebrum-Gray-Upper_3D	multiphasic-fcd	1060	2.4	0	
HE_OR_CorpusCallosum_3D	multiphasic-fcd	1060	3	0	
HE_OR_Thalamus_3D	multiphasic-fcd	1060	2.4	0	
HE_OR_Brainstem-Midbrain_3D	multiphasic-fcd	1060	4.8	0	
HE_OR_Brainstem_3D	multiphasic-fcd	1060	4.8	0	
HE_OR_BasalGanglia_3D	multiphasic-fcd	1060	2.4	0	
HE_OR_Cerebrum-White_3D	multiphasic-fcd	1060	3	0	
HE_MG_Pia_2D	neo-Hookean	1100	12500	0.35	
HE_MG_Tentorium_2D	neo-Hookean	1100	31500	0.3	
HE_MG_Arachnoid-Cerebrum_2D	neo-Hookean	1100	12000	0.35	
HE_MG_Arachnoid-Cerebellum_2D	neo-Hookean	1100	12000	0.35	
HE_MG_Falx_2D	neo-Hookean	1100	12500	0.35	
HE_VS_Sagittal-Sinus_3D	neo-Hookean	1040	0.2	0	
HE_VS_Sagittal-Sinus-Anterior_3D	neo-Hookean	1040	0.2	0	
HE_VS_Sinus-Dural_2D	neo-Hookean	1100	31500	0.35	
HE_MG_Dura_2D	neo-Hookean	1100	31500	0.35	
HE_Spinal-Cap_2D	neo-Hookean	1100	31500	0.315	
HE_BC_Skull-Outer-Inner-Diploe_3D	rigid body				
HE_CF_Ventricle-Lateral_3D	Holmes-Mow	1060	0.2	0	4
HE_CF_Ventricle-Third_3D	Holmes-Mow	1060	0.2	0	4
HE_CF_CSF_Cerebrum_3D	Holmes-Mow	1060	0.2	0	4
HE_CF_CSF_Cerebellum_3D	Holmes-Mow	1060	0.2	0	4

We followed this same method when transferring the material properties of HE_VS-Sagittal-Sinus_3D and HE_VS_Sagittal-Sinus-Anterior-3D from GHBMC to FEBio. All shell (2D) brain

domains in FEBio were assigned identical material properties and thickness as in LS-DYNA. These material properties were not tuned to match a desired output.

We tested two different representations for the CSF-containing regions of the mesh (ventricles and CSF surrounding the brain) to simulate their compaction as the brain swelled. In one strategy, the CSF containing elements were removed (represented by empty space), and contact definitions applied to the surrounding interacting surfaces. In a second scenario, CSF regions were represented by material elements with low moduli, similar to the strategy in the GHBMC model. Given the extreme deformations due to swelling, the CSF was represented by a Holmes-Mow material that exhibit mild strain stiffening to prevent element inversions.

4.2.d Simulating Swelling

The displacement histories at 1 millisecond intervals for each node from the GHBMC simulations were read into FEBio. Figure 17 and Figure 18 show the linear translational accelerations and rotational accelerations used as input to the GHBMC model; Figure 19 shows the resulting first principal strain histories of representative elements from five different parts of the brain. A common strategy to predict tissue injury in TBI simulations is based on tracking the maximum principal strain (MPS) experienced by an element [130, 132, 138].

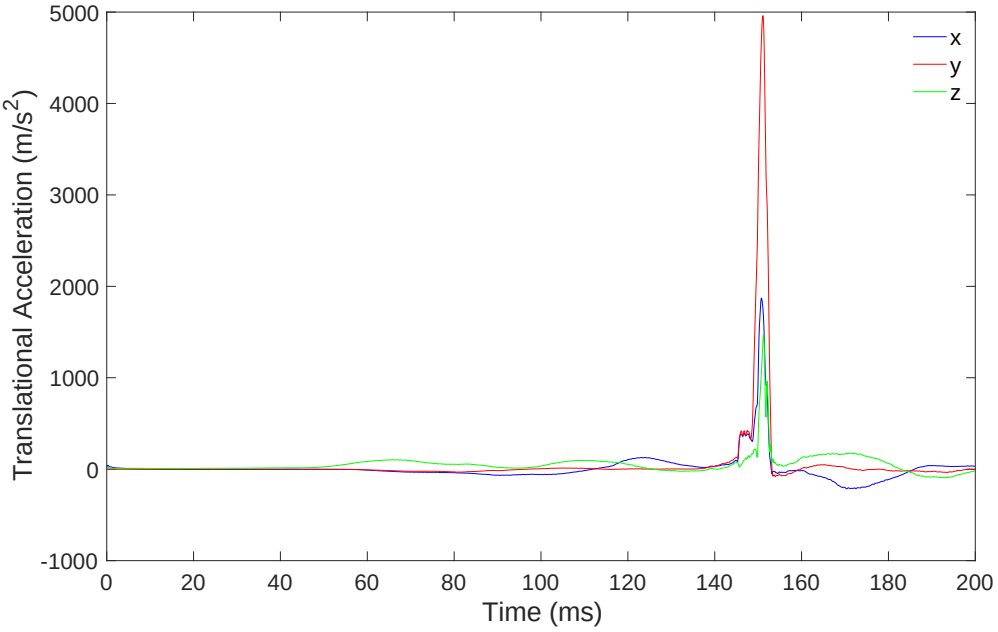

Figure 17: Linear translational accelerations used as input to the GHBMC model to simulate initial brain deformation during the reconstructed fatal pedestrian crash scenario.

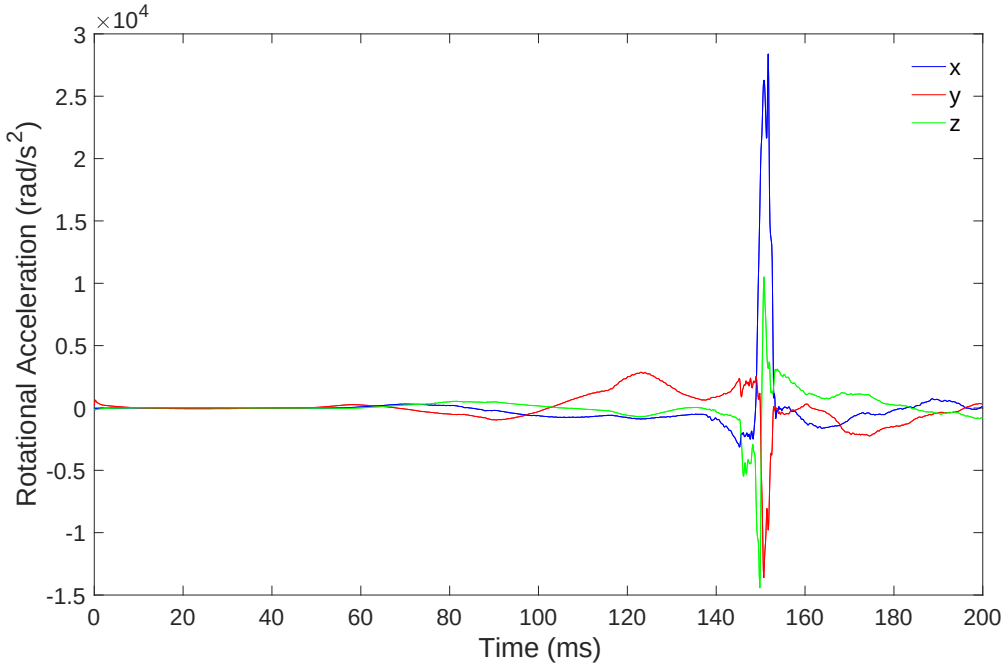

Figure 18: Rotational accelerations used as input to the GHBMC model to simulate initial brain deformation during the reconstructed fatal pedestrian crash scenario.

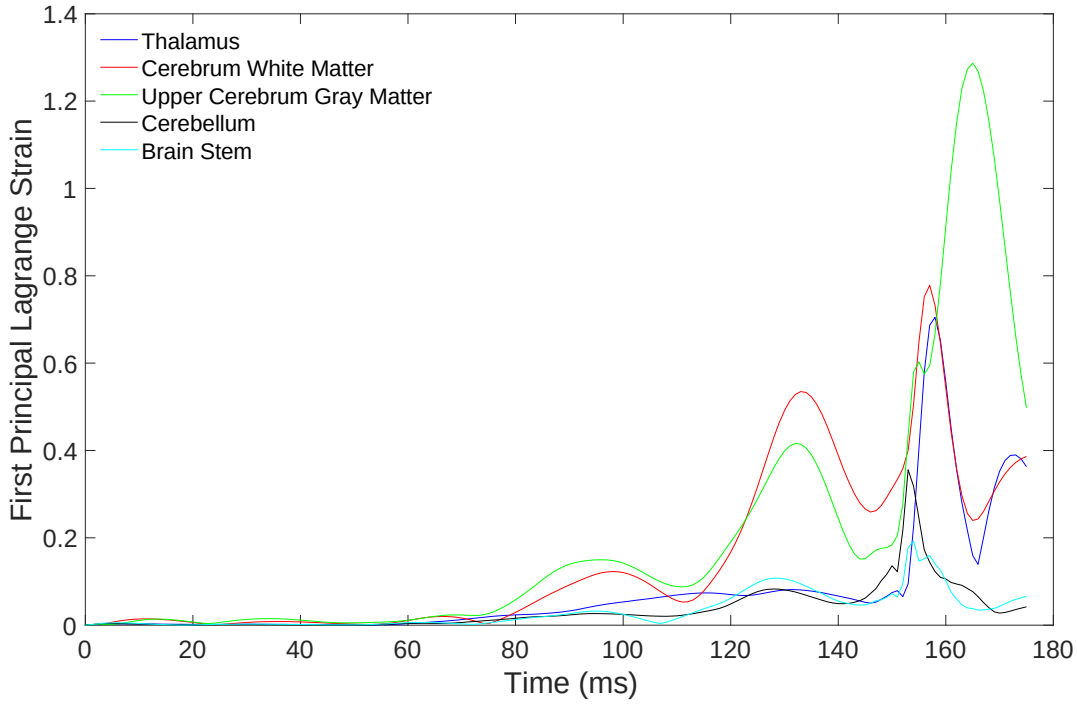

Figure 19: First principal strain histories of representative elements from indicated brain structures during the reconstructed fatal pedestrian crash scenario in response to the 6 degree of freedom accelerations represented in Figure 17 and Figure 18.

We adopted a similar strategy using the feature of reactive damage mechanics in FEBio that allows for individualized relationships between an input parameter driving damage and the subsequently altered material property.

The amount of damage that an element experienced was assumed to obey a log-normal cumulative distribution function:

Equation 11

$$D = \frac{1}{2} erfc[-\frac{(ln\frac{x}{\mu})}{\sigma\sqrt{2}}]$$

where D is damage (ranging from 0 to 1), x is the material input parameter (MPS in this case), and μ and σ are parameters to define the midpoint and spread of the cumulative distribution

function. This distribution was chosen for its simplicity because it can be specified with only 2 parameters.

In our case, we used the damage metric as a surrogate to represent cell death. Intuitively, the log-normal distribution represents the expected relationship between strain and cell death: at low strains, cell death is zero; as strain increases, cell death increases; as strain increases further, cell death saturates as all cells die. Based on experimental studies in the literature that have characterized the relationship between strain and cell death, we set $\mu = 0.35$ and $\sigma = 0.25$ (Figure 20) [139-152]. The choice of a particular distribution function (e.g. log-normal vs. Weibull) does not affect the predictions as long as the chosen distribution accurately represents the literature.

We assumed that the exposure of the FCD was proportional to the damage metric, i.e. cell death, with the maximum tissue FCD set to -60 mEq/L. The choice of -60 mEq/l was based on several studies reporting tissue osmolarity driving edema ranging from a low of -56 mEq/l [153] to a high of -92 mEq/l [154] with an average of -70 ±14 mEq/l [155]. A choice of -60 mEq/l seemed reasonable. Therefore, to simulate cell death and initiate swelling, each multiphasic element was assigned a referential FCD, c_r^F, based on its MPS according to Equation 11 multiplied by the maximum FCD.

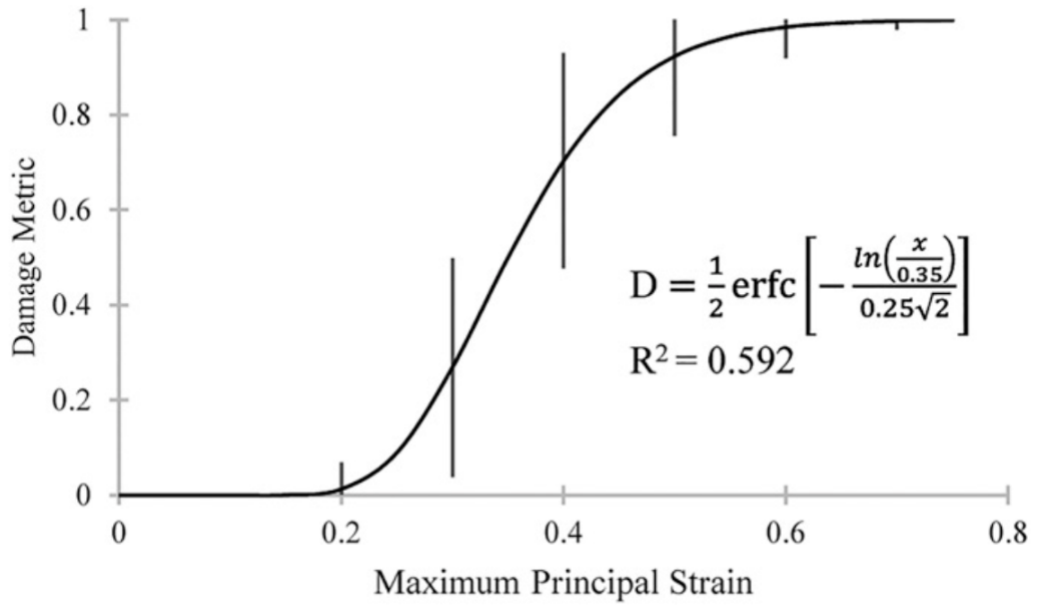

Figure 20: Relationship between maximum principal strain (MPS) and damage leading to strain-induced exposure of FCD based on a review of the experimental literature.

4.2.e Simulating Ischemic Swelling

As brain tissue swells, nearby tissue undergoes compression. We reasoned that this adjacent compression leads to constriction of blood vessels and subsequent reduction of blood flow. If blood flow is reduced sufficiently, additional brain cells die due to ischemia in those compressed regions, exposing additional FCD, causing further secondary swelling. The relative volume was related to damage using Equation 11 again but this time with $x = 1 - J$, $\mu = 0.3$ and $\sigma = 0.1$. Healthy brain begins to die when blood flow dips below 40-50% of normal levels, whereas the threshold for compromised or stressed tissue is higher [156]. Therefore, for traumatically injured brain, we reasoned that cells begin to die when blood flow is reduced to 70% of normal and assumed that blood flow was related to tissue volume. We reasoned that blood flow was proportional to the pore area fraction (e.g. cross sectional area open for blood flow) and that pore cross sectional area was the same as pore volume fraction, φ^w (Equation 6),

according to Delesse's law for porous materials. The resulting damage, a value between 0 and 1, was multiplied by the maximum FCD, and another round of swelling was simulated, representing both causes of cell death: MPS during impact and ischemia.

4.2.f Predicting Mortality

After the swelling simulation, ICP was calculated as the volume averaged minimal principal stress of the swelling (brain tissue) elements. The minimum principal stress, which is the least tensile (most compressive) stress, was chosen to represent ICP because that is closest to what is measured clinically with an intracranial pressure probe placed into the brain parenchyma, Indeed, if we assume that the contact between the probe and brain parenchyma is frictionless, then the minimum principal stress is exactly equal to the contact stress (whether the probe is touching fluid or porous tissue matter), which is the parameter measured clinically. Based on clinical results from Balestreri et al. that reported mortality as a function of ICP after TBI, we parameterized their results using Equation 11 with $x =$ ICP as the input parameter, μ = 30 mmHg, and σ = 0.1 (Figure 21) [43].

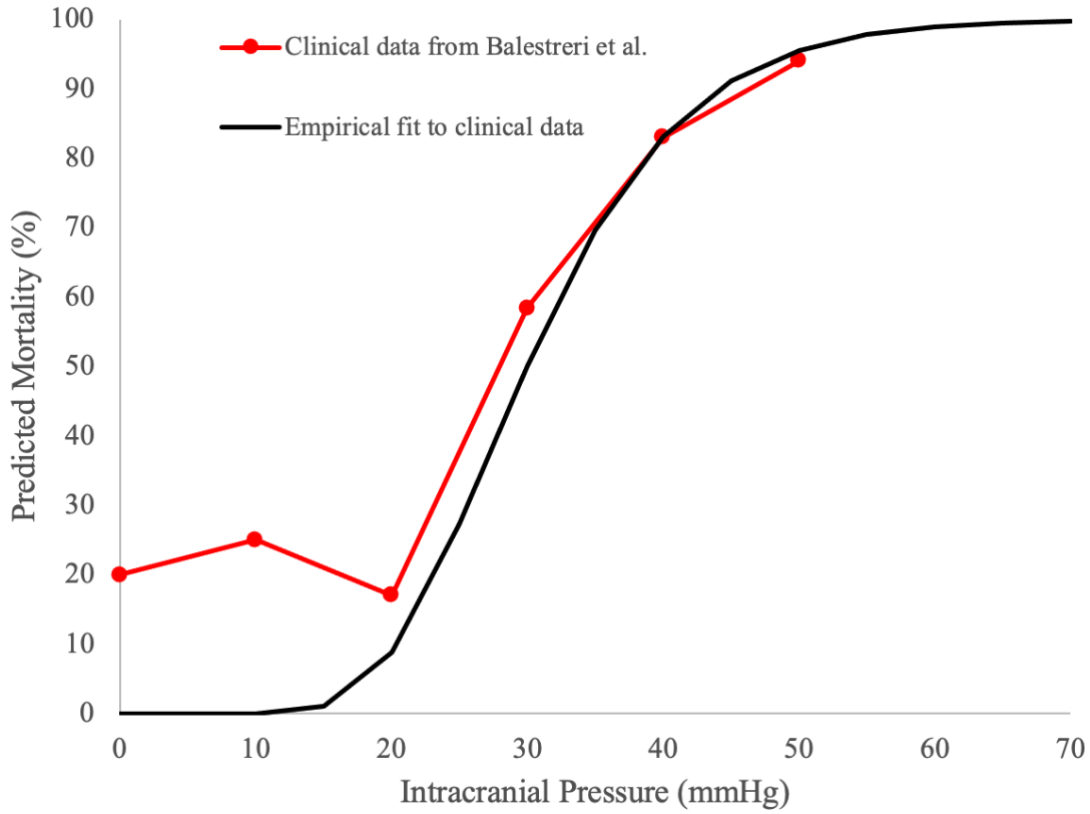

Figure 21: Relationship between predicted mortality and ICP based on clinical data from Balestreri *et al.* [43] in red. The empirical fit to the clinical data in the literature provided a continuous relationship to predict mortality from the simulated ICP from the FEBio modeling described herein. The empirical fit was not tuned to our FEBio model output.

To summarize, all relationships and parameters were not tuned for a desired FEBio model outcome, but were set *a priori* by a review of the literature. The mechanical response of the GHBMC was not tuned from the stock model.

4.3 Results

4.3.a Mesh Visualization Following Swelling

In initial simulations, CSF was modeled as empty space allowing the brain to swell into them, simulating the clinical experience. The geometry of the GHBMC mesh was not originally

conceived for this purpose, and the boundary between the CSF containing regions and surrounding structures can be quite irregular. Because the contact conditions were ill-defined, some simulations failed due to large deformations as more FCD was exposed.

Therefore, we used a second strategy to represent the CSF-containing regions similar to that used in the GHBMC mesh, representing CSF as a low modulus material. In this case, a Holmes-Mow material was used, specified by: Young's modulus and a non-linear parameter β. We varied Young's modulus from a low of 0.2 kPa (the same as in the GHBMC model) to a high of 10 kPa and β from a low of 3.5 to a high of 8 to show that predicted ICP was insensitive to the specific values chosen. For the fatal side impact, ICP varied by only 7.6% over this range, supporting that ICP was not overly sensitive to the properties of the CSF. Mild strain stiffening was required to prevent the CSF mesh from deforming to the point that the simulation failed. A Young's modulus of 0.2 kPa and a β of 4 was chosen for subsequent simulations.

For the fatal pedestrian impact, exposure of FCD due to the initial mechanical deformation caused the tissue to swell in damaged regions, while compressing tissue in adjacent regions. The ICP after this initial swelling was predicted to be 3.2 kPa (39.1 mmHg), which carried an 81% chance of death (Figure 22b). The mesh visibly deforms due to the initial swelling with the ventricles being compacted and the brain expanding into the surrounding CSF space. After ischemic swelling, predicted ICP rose to 8.6 kPa (64.1 mmHg), which carried a 99% chance of death (Figure 22c). The mesh further deformed during this second round of ischemic swelling. Predicted ICP for the volunteer case remained at 0 kPa.

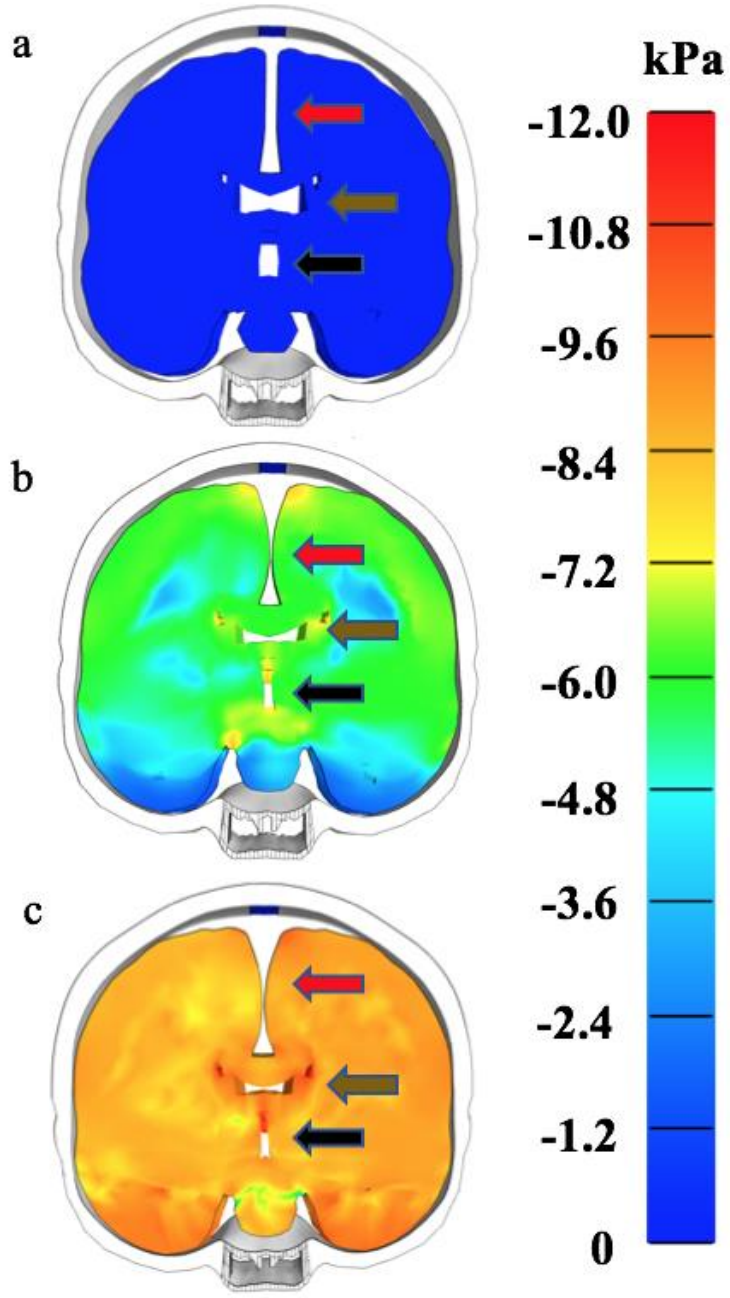

Figure 22: Simulation results of the fatal pedestrian impact case presenting the minimal principal stress (pressure). A) The undeformed mesh. B) The deformed mesh after the initial round of swelling in response to exposure of FCD due to mechanical injury of brain tissue. The mesh visibly deforms due to the initial swelling with the ventricles being compacted (black and brown arrows) and the brain expanding into the surrounding CSF space (magenta arrow), increasing ICP to 5.21 kPa (39.1 mmHg). C) After ischemic swelling, the mesh further deformed, increasing ICP to 8.55 kPa (64.1 mmHg).

4.3.b Effects of Initial Swelling and Ischemic Swelling

To show the progression of the simulation in more detail, for brain tissue elements, histograms of the element FCD in the reference configuration, c_r^F, volume ratio J, and minimum principal stress of $\boldsymbol{\sigma}$ after the initial swelling and ischemic swelling steps are shown in Figure 23, Figure 24, and Figure 25, respectively. Note how the initial distributions change from the first to the second round of swelling, driven by the exposure of the FCD.

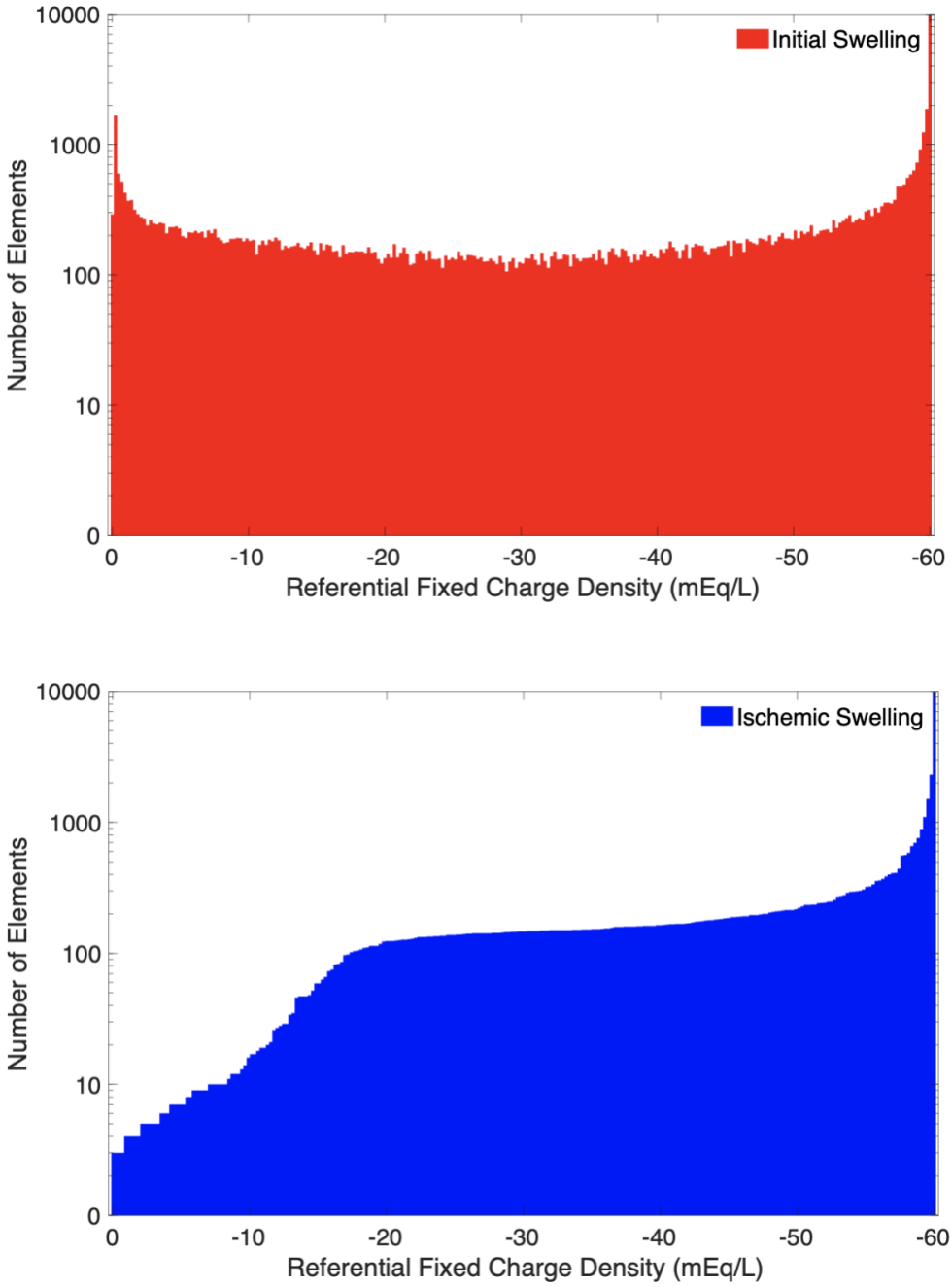

Figure 23: Histogram of the FCD in the reference configuration, c_r^F, per element of brain tissue for the fatal case. The FCD driving the initial swelling (red) due to the impact and driving swelling due to ischemia (blue) due to the combination of MPS and compression are shown. Note how the shape of the histogram changes between the phases of the simulation with a rightward shift.

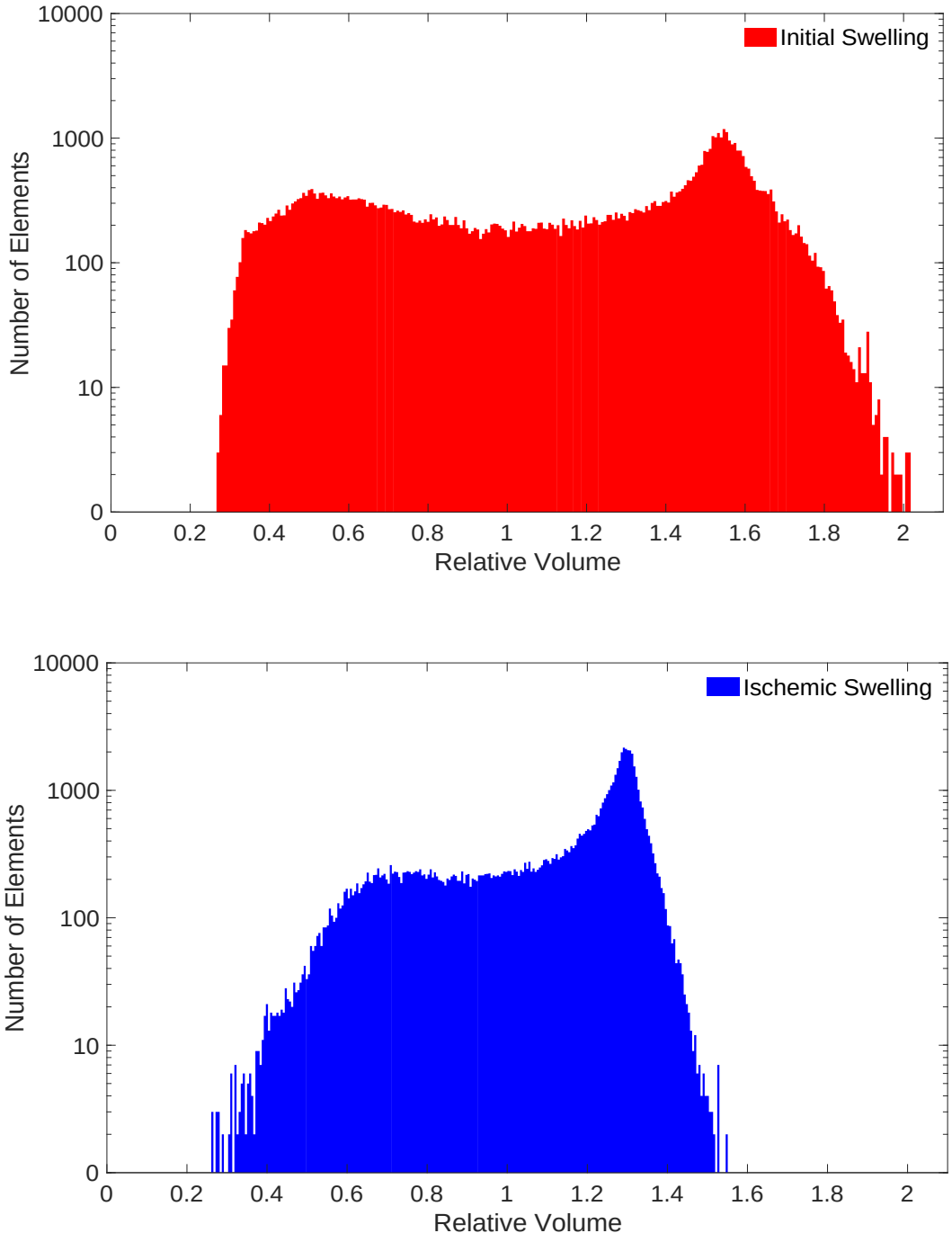

Figure 24: Histogram of brain tissue relative element volume in the fatal pedestrian case after the initial swelling (red) due to the impact and after ischemia (blue). Note how the shape of the histogram changes in the ischemic phase as more elements swell, thereby increasing ICP. Interestingly, the histogram of ischemic swelling shows far fewer compacted elements when compared to the histogram of initial swelling. The peak of the histogram of ischemic swelling is also shifted to the left when compared to the peak of the histogram of initial

swelling because although more elements swell in the ischemic simulation, they are still confined within the fixed volume of the rigid skull, forcing each of these elements, on average, to occupy a smaller amount of accessible volume, while driving pressure up.

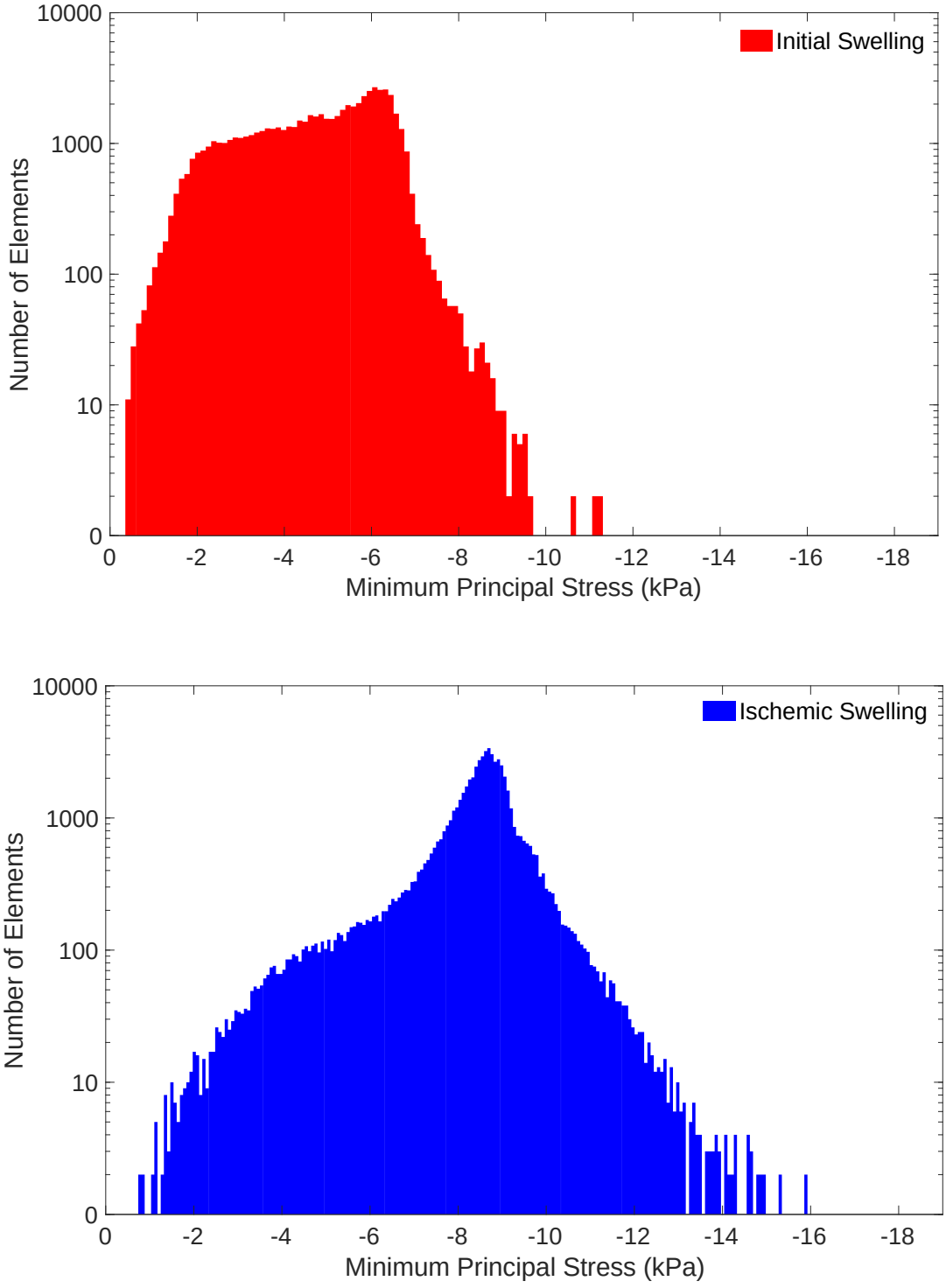

Figure 25: Histogram of brain tissue minimum principal stress (negative in compression) in the fatal pedestrian case after the initial swelling (red) due to the impact and after ischemia (blue). Note how the shape of the histogram significantly shifts to the right in both instances, thereby increasing ICP throughout the brain.

4.4 Discussion

Our study is the first to predict brain swelling and the subsequent increase in ICP after an injurious deformation. Swelling was modeled using triphasic mechanics driven by deformation-based exposure of FCD. Furthermore, ischemia-induced cell death and swelling were taken into account when calculating ICP and predicting outcome (mortality).

Previous studies have used FE modeling to predict injury severity after TBI. Zhang et al. used FE modeling to simulate the biomechanical differences between frontal and lateral impact [157]. Although they examined ICP, it was the instantaneous ICP during the impact. Because they did not simulate swelling, this ICP is not the same as seen clinically after TBI where a sustained elevated ICP affects outcome. Yao et al. studied vehicle-pedestrian impacts using multi-body system pedestrian and car models in which the estimated head impact conditions were used as inputs for their FE head model [158]. Just like the study conducted by Zhang et al., this study only looked at transient ICP.

Other groups have attempted to predict injury severity or death based on MPS. Takahashi and Yanaoka hypothesized that peak MPS values correlated with the probability of brain injuries and developed a new injury criterion called CIBIC (Convolution of Impulse response for Brain Injury Criterion) [159]. However, relying on MPS as a measure to predict injury outcome can be misleading as it is often measured from a single element only. It is possible for a single element to experience large deformations yet have negligible effect on the brain as a whole. Furthermore, brain edema is a complex phenomenon encompassing the whole brain, requiring more than a single MPS to simulate it. When we modeled sustained ICP from edema, we considered each element's strain, thus providing different swelling scenarios depending on the type of impact. Swelling is inhomogeneous, as is the induced strain field, and

therefore requires consideration of all elements in the brain. Although the initial damage is deterministic based upon the distribution described by Equation 11, the subsequent swelling, ischemic cell death, and ICP increase are not linear nor can they be inferred directly from the deformation field. Equation 1 shows that osmotic pressure varies nonlinearly with fixed charge density and Equation 9 shows that fixed charge density varies nonlinearly with the volume ratio J. Furthermore, relying on the crash-induced MPS to calculate final ICP cannot sufficiently describe additional complexities such as the fact that ICP rises drastically after the brain has occupied all remaining space (CSF elements) within the skull.

In a study conducted by Kleiven, a motorcycle accident was reconstructed with an FE model [130]. MPS was found to predict the injuries seen in CT images with correlation between the hematoma location in CT images and the location of MPS in the FE model. Because of the increased mortality rate due to hematomas and hemorrhages, analyzing MPS may be advantageous when analyzing risk of death following TBI. However, relying solely on MPS from FE models only captures the strain and potential injury during the moment of the deformation; post-impact brain edema and the resulting injuries remain beyond their scope. One advantage of our model is that we extract MPS from each element as others do, but we use it as a predictive parameter in determining the pattern and magnitude of brain edema after impact. This ultimately allows us to predict ICP resulting from sustained brain edema for each case and relate it to clinical outcome.

Our model, however, does have limitations. The first step in our strategy to predict mortality based on ICP relies on the MPS values calculated from the output of the GHBMC model. As such, any uncertainties in reconstructing a crash-scenario associated with the accelerations used as input to the GHBMC model will affect the fidelity of our predictions.

Furthermore, any limitations associated with the performance of the GHBMC model to accurately predict brain strain, i.e. the degree to which GHBMC has been validated (or any other FE model), must be taken into account when interpreting our predictions. It should be noted that the relationship between strain and cell death (exposure of FCD), the relationship between pressure and ischemic cell death, and the relationship between ICP and mortality were not tuned for a desired FEBio model outcome, but were set *a priori* by a review of the literature. Furthermore, the parameters within the GHBMC model to simulate the mechanical response during the crash-scenario were not altered from the stock model supplied by Elemance and were not tuned in the current study. However, these relationships may require adjustment as more validation data is reported in the literature in the future.

During TBI, hemorrhage can occur due to tearing of blood vessels. Brain cells surrounding a blood clot can die [160] due to blood toxicity leading to further damage and more swelling. Our model currently does not incorporate hemorrhage. Another limitation is that the relationship between ischemia and resulting infarct volume from damage needs to be validated with more experimental data. In the future, we hope to incorporate mechanical failure of the bridging veins to model hemorrhage and resulting cell death and swelling. Additional experimental data regarding the relationship between cerebral blood flow and infarct volume is needed to better model cell death and swelling resulting from ischemia. Ultimately, our model is currently not validated at this stage given the very limited set of simulations run; rather this study is a demonstration of the feasibility of predicting sub-acute and life-threatening pathology of increased ICP after TBI.

Chapter 5: Simulating Cerebral Edema and Ischemia After Traumatic Acute Subdural Hematoma Using Triphasic Swelling Biomechanics

5.1 Introduction

Acute subdural hematoma (ASDH) is an intracranial bleed often resulting from traumatic brain injury (TBI) [161-164]. Between 12% to 29% of patients with severe TBI have ASDH. Stretching and tearing of the bridging veins and cortical arteries by head trauma cause collection of blood in the innermost layer of the dura [161, 165]. The most common convexity ASDH is typically found in the supratentorial regions of the brain and is diagnosed on computed tomography as an extra-axial, hyperdense, crescent-shaped lesion between the dura and brain parenchyma [165, 166]. Another type of lesion, the interhemispheric ASDH, which is characterized by symptoms such as contralateral monoparesis or hemiparesis, also known as falx syndrome [167, 168], appears as a hyperdense lesion along the interhemispheric fissure [169]. Despite advancements in medical care and intensive treatment, ASDH still carries one of the worst clinical outcomes following head injury, with a reported mortality rate up to 90% [162, 170-174]. Unfavorable outcomes following ASDH have been partially attributed to the damage to brain tissue during impact (primary injury) [26, 162] but have also been associated with secondary injuries including cerebral edema and ischemia [161, 162, 175, 176]. Clinical studies have shown that the initial increase in intracranial pressure (ICP) caused by the mass occupying effect of the blood clot produces secondary brain injury [175-177]. A greater midline shift compared to hematoma thickness is often a sign of secondary brain injury [161, 162, 171], which

could contribute to a further increase in ICP and worse clinical outcomes [162, 178]. In this study, we have tried to further elucidate the underlying secondary brain injury mechanism of traumatic ASDH that contributes to elevated ICP and high mortality rate.

As a secondary injury, ischemia is the most important neuropathological finding in fatal cases of ASDH [179]. The common presence of ischemic brain damage suggests that the mass occupying effect of the ASDH compresses brain tissue, leading to ischemic damage by constricting vasculature and decreasing cerebral blood flow to the affected region [133, 156]. Studies have shown that timely evacuation of hematomas increases the likelihood of recovery, suggesting that quick evacuation may mitigate ischemic damage otherwise caused by the presence of the ASDH. For example, evacuation of the traumatic ASDH within 4 hours of injury reduced mortality rates to as low as 30% and improved functional survival rates as high as 65% [26]. Another study demonstrated a 30% mortality in patients with ASDH surgically treated within 4 hours after injury and a 90% mortality in those surgically treated more than 4 hours after injury [180]. Furthermore, as we have previously hypothesized, ischemic cell death leads to exposure of the fixed charge density (FCD) within cells and causes brain swelling [156]. The inherent negatively charged molecules that are immobile within the cell such as proteins, glycosaminoglycans, and DNA comprise the intracellular FCD. When a cell loses its metabolic function or membrane integrity after death, extracellular cations flow into the cell to neutralize the fixed negative charges, increasing the osmolarity within the brain tissue relative to its fluid domains (blood and cerebrospinal fluid). The difference in osmolarity between these compartments produces an osmotic pressure gradient that drives water into the brain, leading to brain swelling. Over time, the FCD associated with dead cells undergoes proteolytic breakdown,

becoming solubilized and diffusing out, eventually reducing brain swelling. This study focuses only on the swelling, injurious stage of this process.

In our previous studies, we demonstrated that ischemic damage caused samples of brain tissue to swell and identified the FCD as the driving force of brain swelling [20, 21]. Because ischemic cell death causes brain swelling, the swollen tissue compresses its adjacent regions. As a result, more brain regions may experience ischemia, which leads to additional cell death, brain swelling, and elevated ICP. Therefore, we hypothesize that the increased likelihood of death associated with ASDH is due to the mass occupying effect of the blood clot that exacerbates ischemic damage, which in turn leads to more brain swelling and higher ICP due to increased FCD exposure as a consequence of the ischemic tissue death.

A computational pipeline was developed in this study to simulate ischemia, with and without ASDH, using a previously established finite element model that simulates cerebral edema following motor vehicle crashes [37, 124]. The computational pipeline consists of consecutive brain swelling simulations and predicts the resulting increase in ICP as ischemia progresses. Brain swelling was modeled using triphasic swelling biomechanics [19], driven by the exposure of the FCD and the Gibbs-Donnan effect. Two common convexity ASDH with different intracranial locations and an interhemispheric ASDH were modeled. This study aims to predict a dynamic range of increased ICP for ASDH by incorporating the progression of secondary brain injuries after impact, using a novel computational approach. With this model, it may be possible to improve the prediction of mortality rate for patients with ASDH and aid safety system design for the prevention of head injury.

5.2 Methods

5.2.a Brain Swelling and Triphasic Swelling Biomechanics

Brain tissue is about 80% water and 20% solid matter. As described in our previous study [124], brain tissue was modeled as a mixture of a porous solid matrix and an interstitial fluid containing two monovalent counter-ions (Na^+ and Cl^-). The solid matrix within brain cells contains negatively charged molecular species, such as proteins, glycosaminoglycans, and DNA, that contribute a FCD in the intracellular space, which is separated by the plasma membrane from the extracellular space. Under homeostatic conditions, the negative transmembrane potential (resulting from ionic imbalance) is maintained by the sodium-potassium pump as it counters the role of leak channels and other processes that use the potential energy of the transmembrane potential. When blood flow is reduced or the plasma membrane is damaged, the pumps can no longer counteract the thermodynamic gradient as the intracellular FCD is exposed to the extracellular environment. The exposed FCD attracts counter-ions (Na^+) leading to a higher concentration of ions in the brain tissue relative to the surrounding fluid compartments, creating an osmotic pressure difference according to the Gibbs-Donnan effect, which draws water into the brain. A triphasic analysis under steady-state conditions was performed in FEBio to predict brain swelling in response to localized and evolving cell death [56].

5.2.b Simulating Primary Injury and Initial Brain Swelling

Details of the pedestrian-to-vehicle impact cases with six-degree-of-freedom acceleration histories of the head using the GHBMC human model were given in a previous study [37]. Eight pedestrian impact cases corresponding to different injury severities were selected from the National Automotive Sampling System - Pedestrian Crash Data Study (NASS - PCDS), Crash

Injury Research and Engineering Network database (CIREN) [37]. The four severe impact cases were chosen such that the Maximum Abbreviated Injury Scale (MAIS) injury was sustained by the head, resulting in a brain injury with an Abbreviated Injury Scale (AIS) rating of 3 or 4. The other four impact cases were fatal impacts chosen such that the brain injury was the cause of death. Using the same strategy as in the previous study, impact simulations were performed first, to predict peak localized tissue strains as predictors of cell death. The maximum principal strain (MPS) experienced by an element of brain tissue was tracked during the impact simulation and converted to percent cell death based on Equation 11 presented in the previous chapter where D is fractional cell death (ranging from 0 to 1), x represents MPS, and μ and σ are parameters that define the midpoint and spread of the function. In this formula, the range of x is 0 to ∞, but in practice there is a finite value for x beyond which all cells die (D = 1). Based on experimental studies in the literature that have established a relationship between strain and cell death, μ was set to 0.27 and σ was set to 0.51 [139-152]. These parameters have been updated from chapter 4 due to better fitting to more data points in the literature. Figure 26 shows the new fit and updated μ and σ values compared to the original fit and resulting parameters from chapter 4.

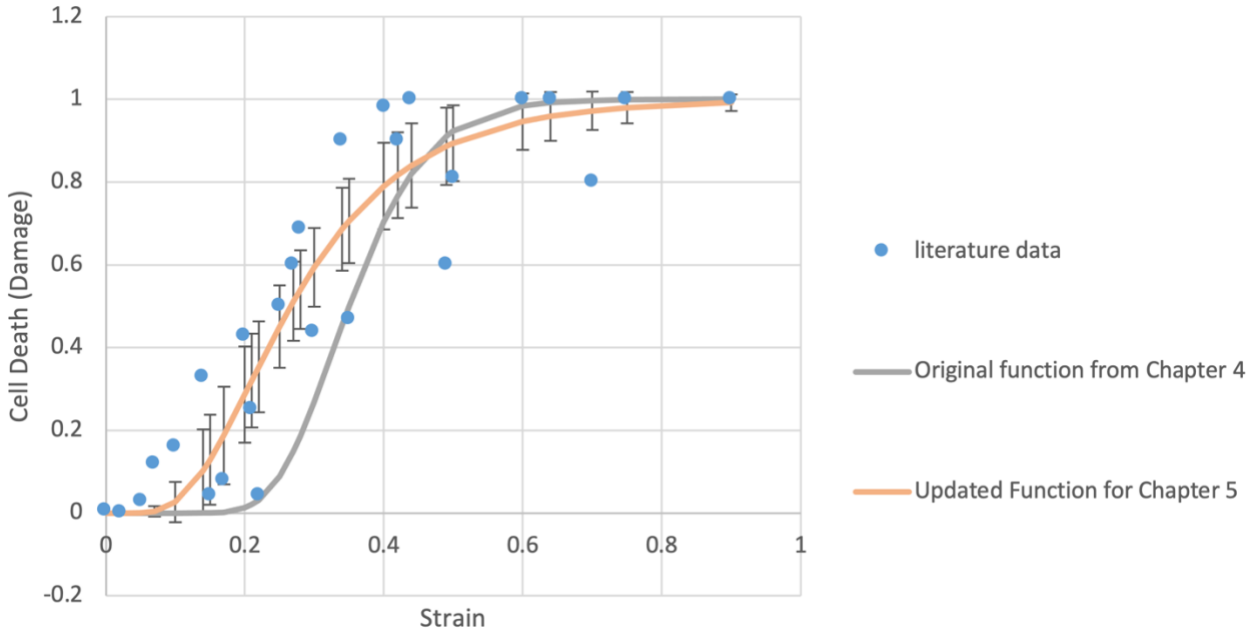

Figure 26: Relationship between brain cell death and strain – comparing fit between chapters 4 (TIP Function) and 5 (MATLAB Fit).

To simulate brain swelling from cell death, it was assumed that FCD exposure was proportional to cell death. The maximum FCD was set to -60 mEq/l based on experimental studies in the literature [154, 155]. Each swelling element was assigned a referential FCD equal to the fractional cell death D multiplied by the maximum FCD.

5.3.c Simulating Ischemia and Ischemic Brain Swelling

When localized regions of brain tissue swells, the surrounding tissue regions are compressed, causing constriction of blood vessels and a decrease in cerebral blood flow. Ischemic cell death occurs when blood flow is sufficiently reduced. To simulate ischemic cell death, tissue relative volume was used as a proxy for blood flow. Modeling brain tissue as a porous material, we assumed that the percent of normal cerebral blood flow is equivalent to the

normalized pore volume fraction $\frac{\varphi^f}{\varphi_r^f}$, which evolves with J according to $\frac{\varphi^f}{\varphi_r^f} = \frac{1-\frac{\varphi_r^s}{J}}{\varphi_r^f}$, where $\varphi_r^s = 0.2$ is the initial solid volume fraction of brain matter (20%) and $\varphi_r^f = 0.8$ is the initial fluid volume fraction of brain matter (80%). The smallest possible value for J is φ_r^s, which represents the limit when all interstitial fluid has been squeezed out of the pore space of brain tissue ($\frac{\varphi^f}{\varphi_r^f} = 0$) and no blood can flow. Thus, we reasoned that 100% cell death occurs when there is no cerebral blood flow ($J = 0.2$), and no cell death occurs when cerebral blood flow is at its normal level ($J = 1$). Additionally, hypoperfusion of blood flow within the brain leads to ischemic tissue damage in the form of three distinct regions: an infarct core, penumbral tissue, and oligemic tissue [181]. The infarct core consists of irreversibly damaged tissue [182] surrounded by penumbral tissue that is also ischemically affected but to a lesser degree than the infarct core [183]. Oligemic tissue, which consists of relatively mildly hypoperfused tissue, surrounds both the penumbra and infarct core [184]. This pattern of injury during ischemia has been seen in humans [185] and animals such as rats [186]. Although oligemia refers to an episode of low blood flow that causes molecular changes, it does not produce an infarct or cell death [187]. Within the oligemic region, there is electrical dysfunction but cellular integrity is maintained [188]. The penumbra, however, barely receives enough blood flow to keep neurons alive and is associated with delayed death of neurons and apoptotic neuronal death [189]. Cell death is known to ensue when blood flow decreases to 80% of control levels [190]. We therefore reasoned that penumbra development begins when cerebral blood flow drops to 80% of its normal level. Tissue in the penumbra is also known to progressively develop into the ischemic core if blood supply is not restored in a timely manner [156, 191, 192]. One study found that within the infarct core of rat brain, approximately 15% of cells remained healthy while the

remaining approximately 85% of cells were either dead or damaged [193, 194]. Assuming the same pattern of cell death within the infarct core of rat and human brain, we therefore reasoned that at the onset of penumbra development, 85% of cells would eventually die assuming that blood supply would not be restored. Thus, we deduced that 85% of ischemic cell death occurs when cerebral blood flow drops to 80% of normal blood flow ($\frac{\varphi^f}{\varphi_r^f} = 0.80$), with corresponding J = 0.55. By hypothesizing that all cells die without blood flow (J = 0.2), that 85% cell death occurs when cerebral blood flow drops to 80% of normal levels (J = 0.55), and that no cell death occurs when cerebral blood flow is at normal levels (J = 1), ischemic cell death was approximated by fitting a relationship between these three points using Equation 11 but with x = 1-J. The resulting μ and σ are 0.305 and 0. 428, respectively.

Throughout the ischemic brain swelling simulations, the computational pipeline recorded the highest cell death percent in each swelling element and used it as the initial condition for the next simulation. ICP was extracted at the end of each simulation, calculated as the volume averaged minimum principal stress of the entire brain parenchyma, which corresponds to what is measured clinically with an ICP probe placed into the brain parenchyma. The simulations were terminated when the simulated ICP stopped increasing. A flowchart of the computational pipeline we developed in C++ is shown in Figure 27.

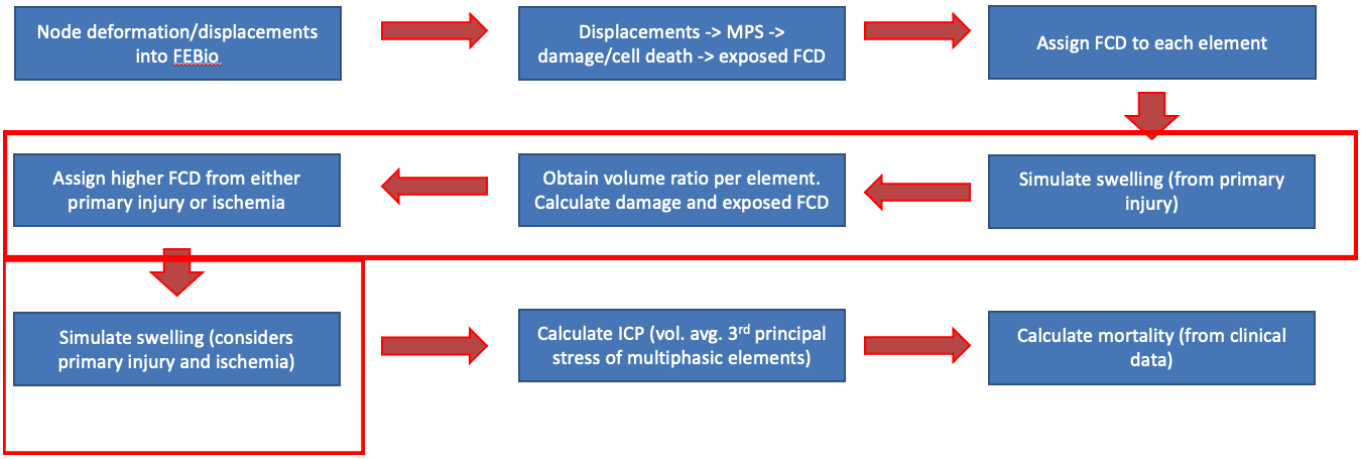

Figure 27: Automated computational pipeline coded using C++. Steps highlighted in red signify portions of the pipeline that were repeatedly simulated until ICP stopped increasing.

5.2.d FEBio Mesh

As in our previous study [124], the skull and brain meshes from the Global Human Body Models Consortium (GHBMC) model were extracted and imported into FEBio Studio (febio.org) [55, 56], The elements of the brain parenchyma that are subject to swelling were redefined as triphasic in FEBio. The material properties of all the elements were imported from GHBMC to FEBio using the same method as in the previous study [124]. However, unlike in the previous study in which the elements representing cerebrospinal fluid were modeled as a Holmes-Mow material (Figure 28), in the current study those elements were removed from the mesh (Figure 29) to better represent resorption of fluid over the time course of brain swelling.

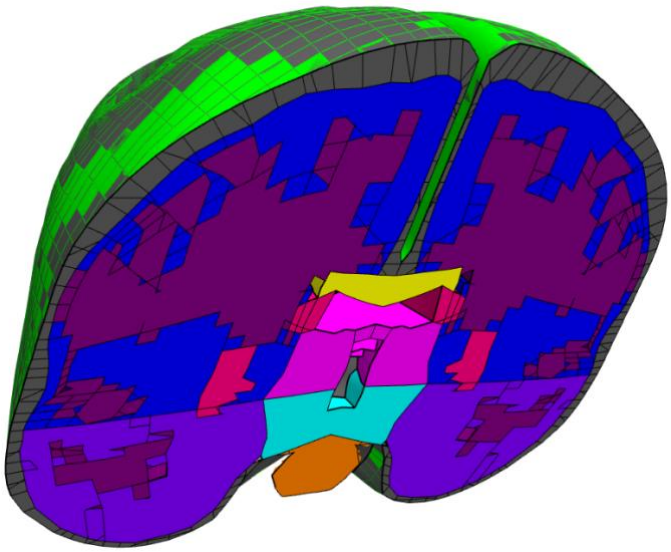

Figure 28: Cerebrum CSF (gray) lies between the cerebrum arachnoid shell layer (green) and pia shell layer (not visible) which lies on top of the upper cerebrum (blue). In earlier versions of the FEBio swelling model, the CSF was represented by solid elements as it is in the original GHBMC model.

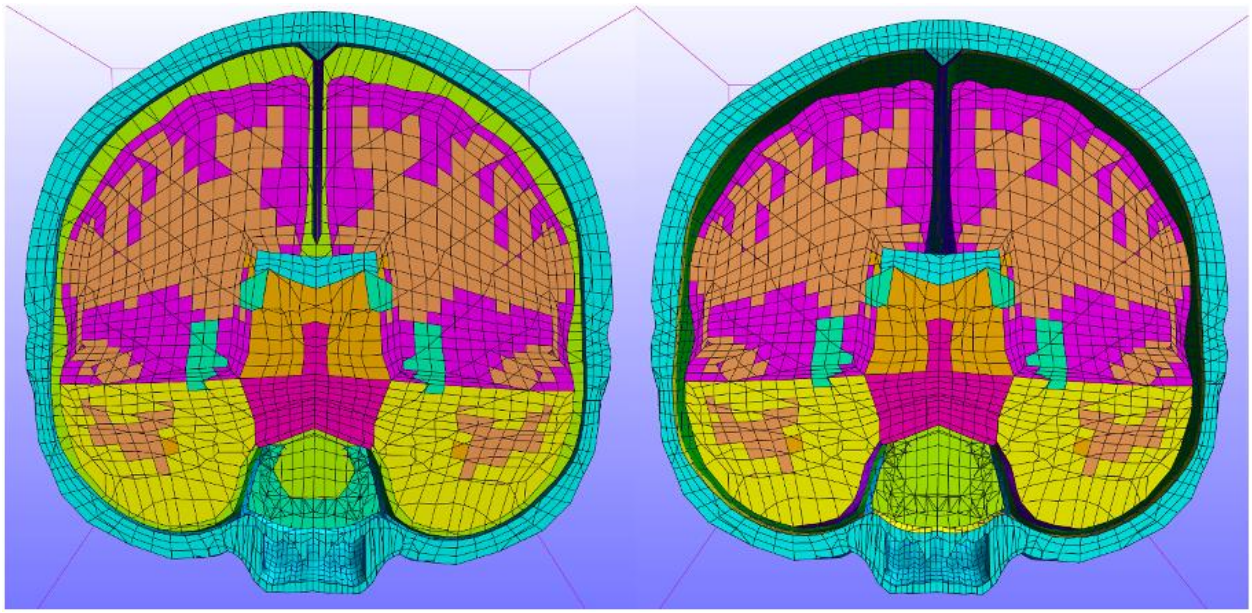

Figure 29: Left figure shows the old brain model with CSF present while the right figure shows the current modified brain model with CSF represented as an open space.

Contact definitions were added to the surrounding interacting surfaces to simulate the compaction of this space as the brain deformed. Figure 30 demonstrates how establishment of contact between the pia and cerebrum arachnoid prevented penetration of both parts during the swelling simulation.

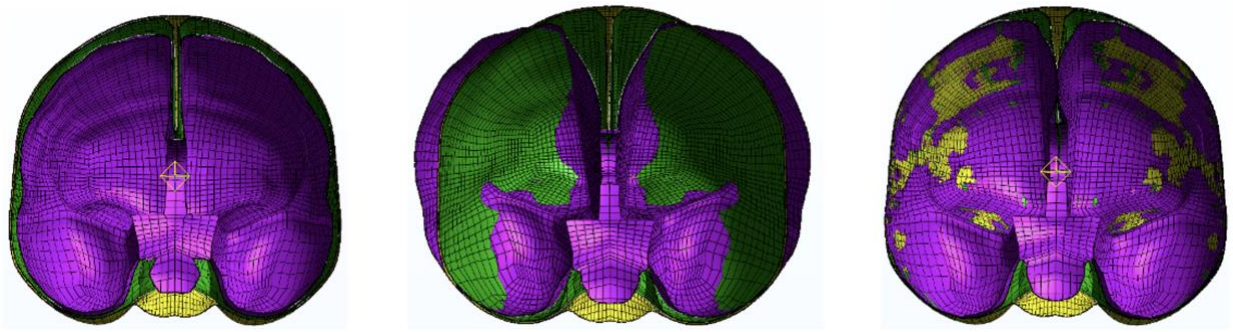

Figure 30: Pia (magenta), cerebrum-arachnoid (green), and dura (yellow) prior to brain swelling (left), after brain swelling but without contacts (middle), and after brain swelling with established contacts (right). Note the lack of penetration between the pia, cerebrum-arachnoid, and dura as the parenchyma (not shown) swells.

5.2.e Modeling ASDH

Two common types of convexity ASDH with different intracranial locations were modeled. To maintain the crescent shape of a convexity ASDH, boundary conditions were applied to prescribe displacements on the selected surface of the 2D shell structure that represents the arachnoid. As shown in Figure 31, Type 1 convexity ASDH, which is typically caused by bridging vein rupture in the frontoparasagittal region [195], spread over the frontal and parietal lobes. As shown in Figure 32 , a Type 2 convexity ASDH, which is typically caused by arterial ruptures in the temporoparietal region [195], is located on the temporal lobe. Clinically, hematoma thickness and midline shift are used to evaluate the extent of the mass occupying

effect of the lesion. According to the surgical guidance for convexity ASDH, surgical evacuation is recommended if the convexity hematoma thickness is greater than 10 mm or the midline shift is over 5 mm [196]. For these two types of convexity ASDH, prescribed displacements of 0 mm, 5 mm, 10 mm, and 14.6 mm at a 45 degree angle into the head (Type 1) directly upon the cerebrum_arachnoid (green shell in Figure 31) towards the brain parenchyma and laterally to the head (Type 2) directly upon the cerebrum_arachnoid (green shell in Figure 32) towards the brain parenchyma were chosen to simulate different hematoma thicknesses to investigate the mass occupying effect (hematoma volume) and subsequent ischemia on ICP.

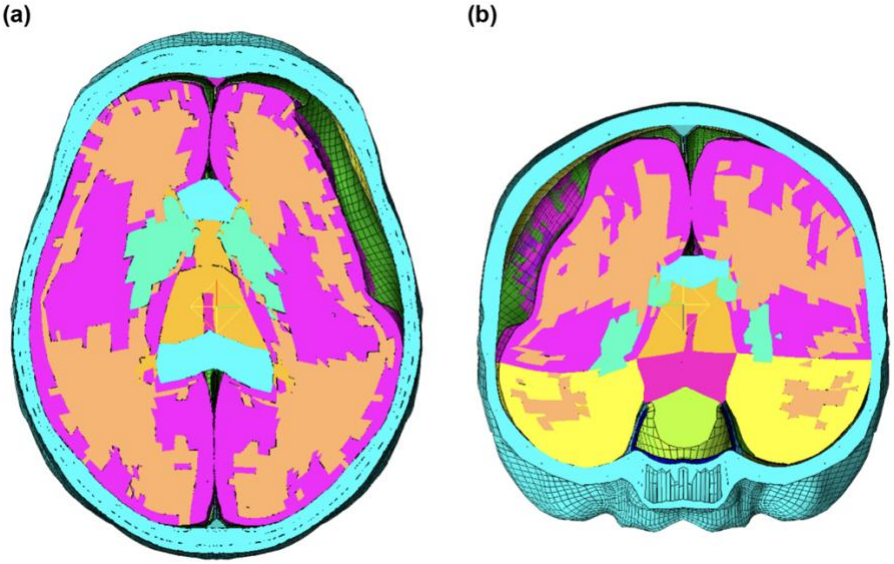

Figure 31: Type 1 convexity ASDH with 14.6 mm thickness after ischemic brain swelling. The mass occupying effect of the blood clot can be seen as a prescribed displacement of the surface of brain. (a) horizontal plane; (b) coronal plane

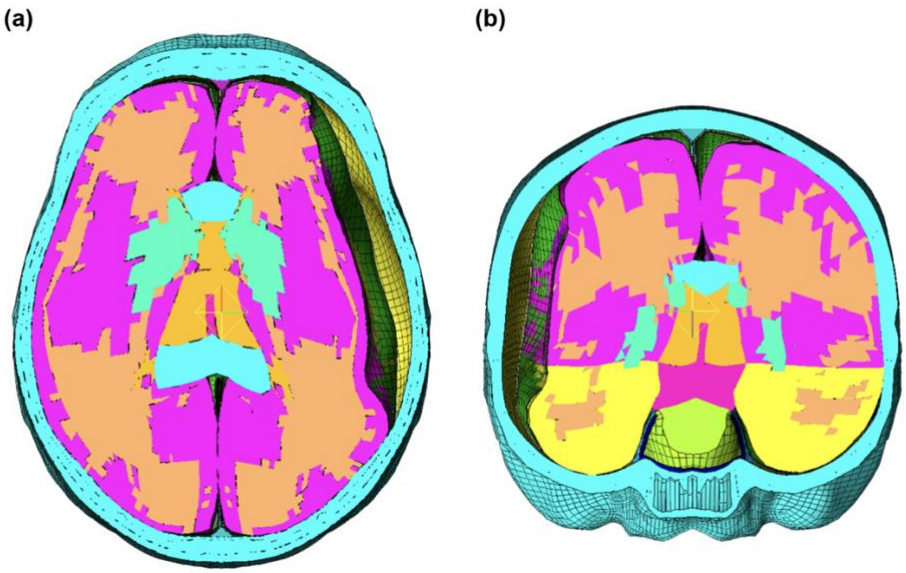

Figure 32: Type 2 convexity ASDH with 14.6 mm thickness after ischemic brain swelling. The mass occupying effect of the blood clot can be seen as a prescribed displacement of the surface of the brain. In contrast to Type 1 convexity ASDH that is located on the frontoparietal lobe, Type 2 convexity ASDH is located more inferior on the temporal lobe. (a) horizontal plane; (b) coronal plane

A traumatic interhemispheric ASDH was also modeled. As shown in Figure 33, the interhemispheric ASDH is located in the interhemispheric fissure. Although no general guidance about the surgical evacuation of traumatic interhemispheric ASDH is provided in surgical guidelines, one study has reported that an interhemispheric ASDH thickness of 12.6 mm was associated with favorable outcomes whereas an interhemispheric ASDH thickness of 15.3 mm was associated with poor outcomes. Therefore, hematoma thicknesses of 0 mm, 10 mm, and 20 mm were chosen for simulation. For all cases involving hematoma, brain swelling was simulated after prescribing displacements of the brain surface to represent the hematoma.

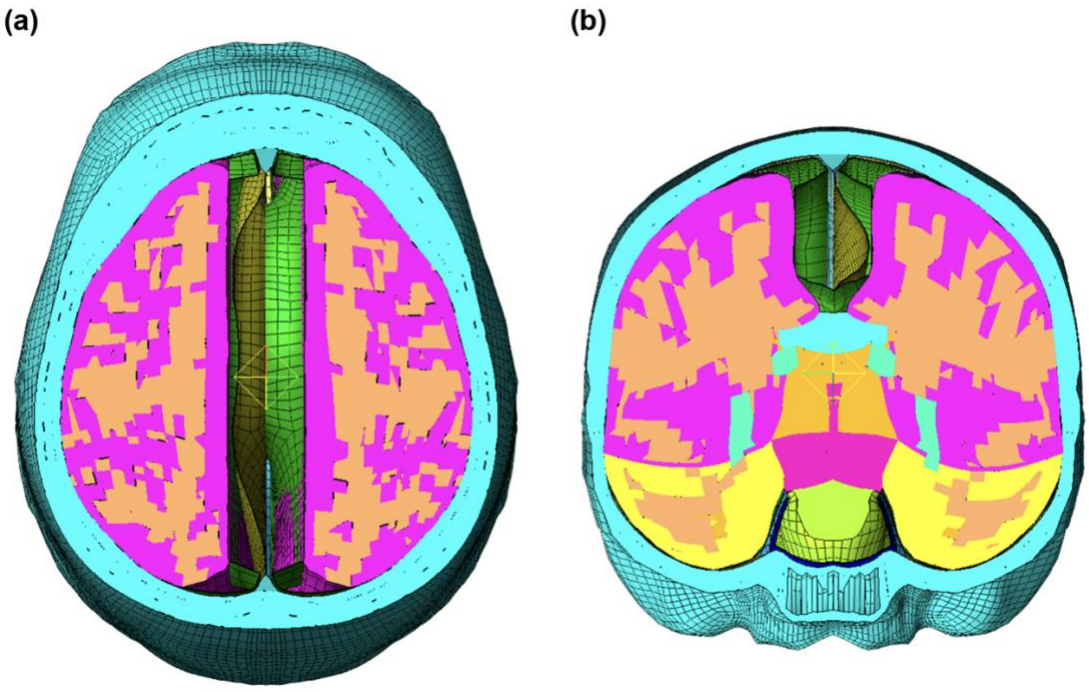

Figure 33: Interhemispheric ASDH with 20 mm thickness after ischemic brain swelling. The mass occupying effect of the blood clot can be seen as a prescribed displacement of the surface of the brain. (a) horizontal plane; (b) coronal plane

5.2.f Statistical Analysis

Because there were 8 different crash scenarios and each one represented a different injury severity, ICP was normalized to the ICP from its corresponding baseline case (0 mm hematoma without ischemic secondary injury).

For convexity ASDH, three-way ANOVA followed by Bonferroni *post hoc* testing was performed to determine the effect of convexity ASDH type, hematoma volume, and ischemia on ICP. The first main factor was convexity ASDH type (Type 1 and Type 2); the second main factor was injury type (primary injury and ischemic injury); and the last main factor was hematoma volume (no hematoma [0 mm], 5 mm, 10 mm, and 14.6 mm thick hematomas).

For interhemispheric ASDH, two-way ANOVA followed by Bonferroni *post hoc* testing was performed to determine the effect of hematoma volume and ischemia on ICP. The first main factor was injury type (primary injury and ischemic injury) and the second main factor was hematoma volume: (no hematoma [0 mm], 10 mm, and 20 mm thick hematomas).

5.2.g φ_r^s Designation

The variable φ_r^s (designated as phi0 in the FEBio input file) represents the solid volume fraction of the material. The FCD value will vary as the solid matrix deforms, and the degree of FCD variation depends on the φ_r^s value. A φ_r^s of 0 was used in our simulations to maintain consistency with the model in chapter 4 and to aid with numerical convergence. Convergence issues have since improved and models are currently being simulated with a φ_r^s of 0.2 to mimic the 20% solid matrix of brain.

5.3 Results

5.3.a Modeling CSF Domains as Elements vs. Empty Space: ICP Comparison

After the CSF elements had been removed and contact interfaces had been established and fine-tuned, we simulated the swelling simulations again to compare ICP values of the previous head model with CSF represented by solid elements present to the predicted ICP values with the CSF represented by empty space. ICP values were slightly higher when solid CSF elements were present. This was expected because the solid CSF elements would stiffen when compressed by brain tissue and therefore, available volume for swelling would be reduced. With the CSF modeled as an empty space now, there is more room for the brain to swell, causing slightly lower ICP values. The ICP differences were less for the least severe head injury cases,

perhaps because these least severe head injury cases do not lead to as much swelling into the spaces between the skull and brain. The percent change in ICP for each head injury case are shown in Table 6, with a graphical comparison shown in Figure 34. Max ICP difference among the 8 cases was ~ 5%, indicating that modeling the CSF regions either using elements with a Holmes-Mow material or empty space did not significantly alter ICP calculations.

Table 6: Percent change in ICP for each head injury case (four severe cases and four fatal cases) when cerebrum CSF and cerebellum CSF were modeled from Holmes-Mow materials to empty space

Head Injury Case	Percent Change in ICP
PEDESTRIAN_SEVERE-03	3.8%
PEDESTRIAN_SEVERE-02	3.7%
PEDESTRIAN_001_L02	3.8%
PEDESTRIAN_SEVERE-04	4.0%
PEDESTRIAN_FATAL-02	4.8%
PEDESTRIAN_FATAL-05-5	4.6%
PEDESTRIAN_FATAL-04	5.2%
PEDESTRIAN_FATAL-03	5.1%

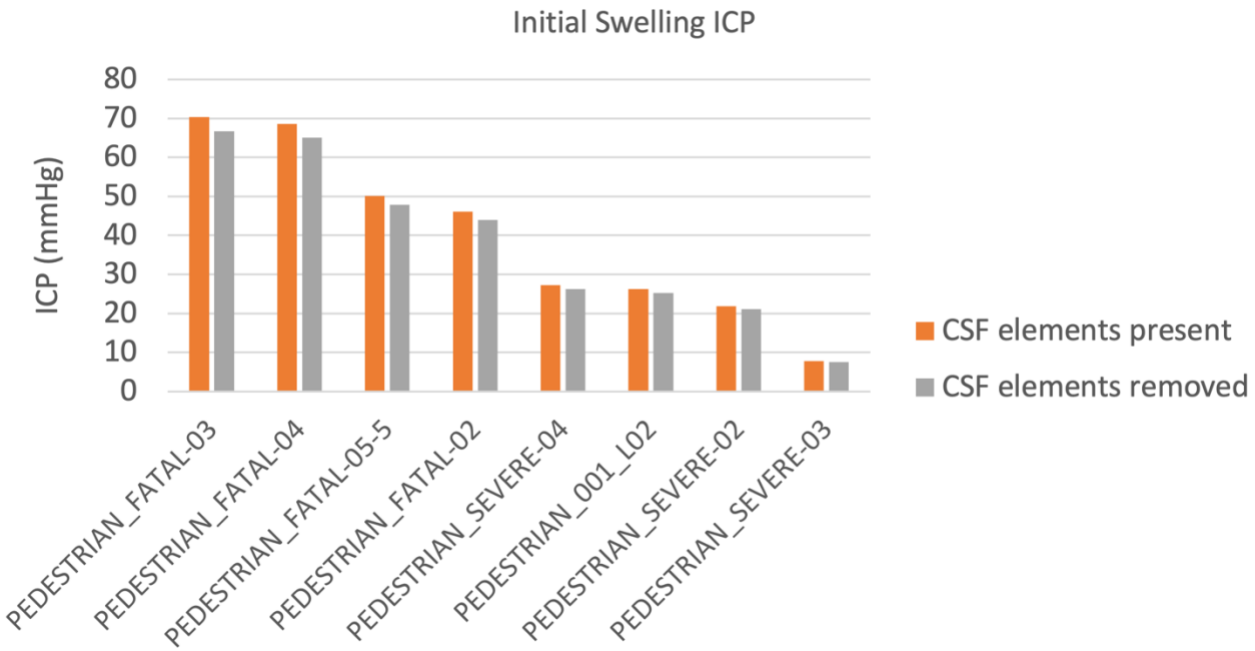

Figure 34: Comparing ICP between cases (four severe cases and four fatal cases) with solid CSF elements and simulations without CSF.

5.3.b ICP Values Plateau After Three Successive Iterations of Ischemic Swelling Simulations

Using our simulation pipeline, we determined that ICP values stopped increasing by the third round of ischemic simulation for the eight pedestrian crash scenarios without hematoma (Figure 35). ICP values also stopped increasing appreciably after the third round of ischemic swelling for all hematoma thicknesses tested. Thus, final ICP values were taken from the third round of ischemic swelling.

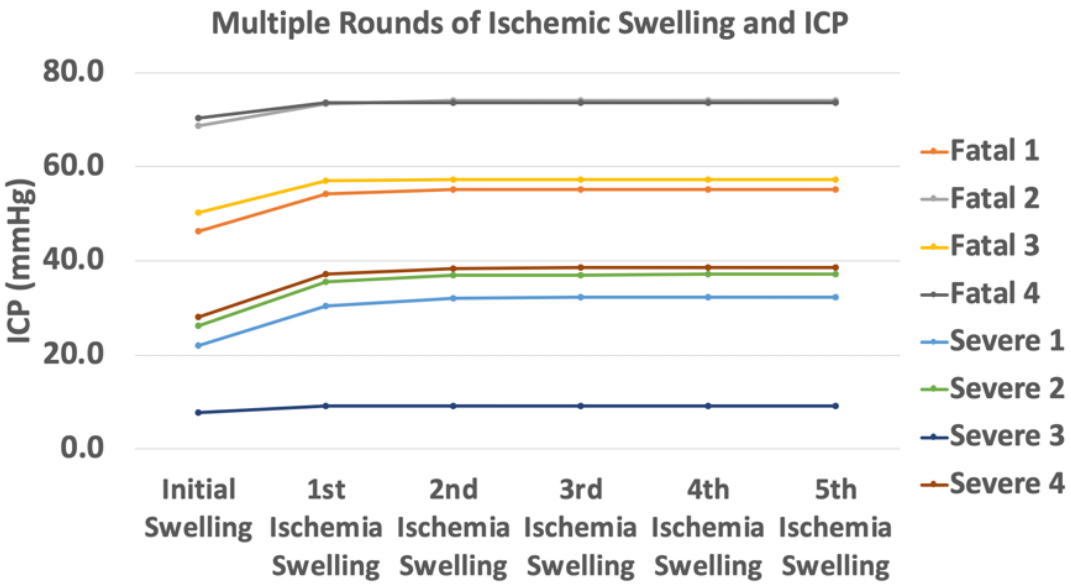

Figure 35: Effect of multiple rounds of ischemia on ICP using new parameters ($\mu = 0.305$, and $\sigma = 0.428$) on the four severe cases and four fatal cases. ICP stops increasing appreciably after the third round of ischemic swelling.

5.3.c ASDH Causes Elevated ICP Levels by Exacerbating Ischemic Injury

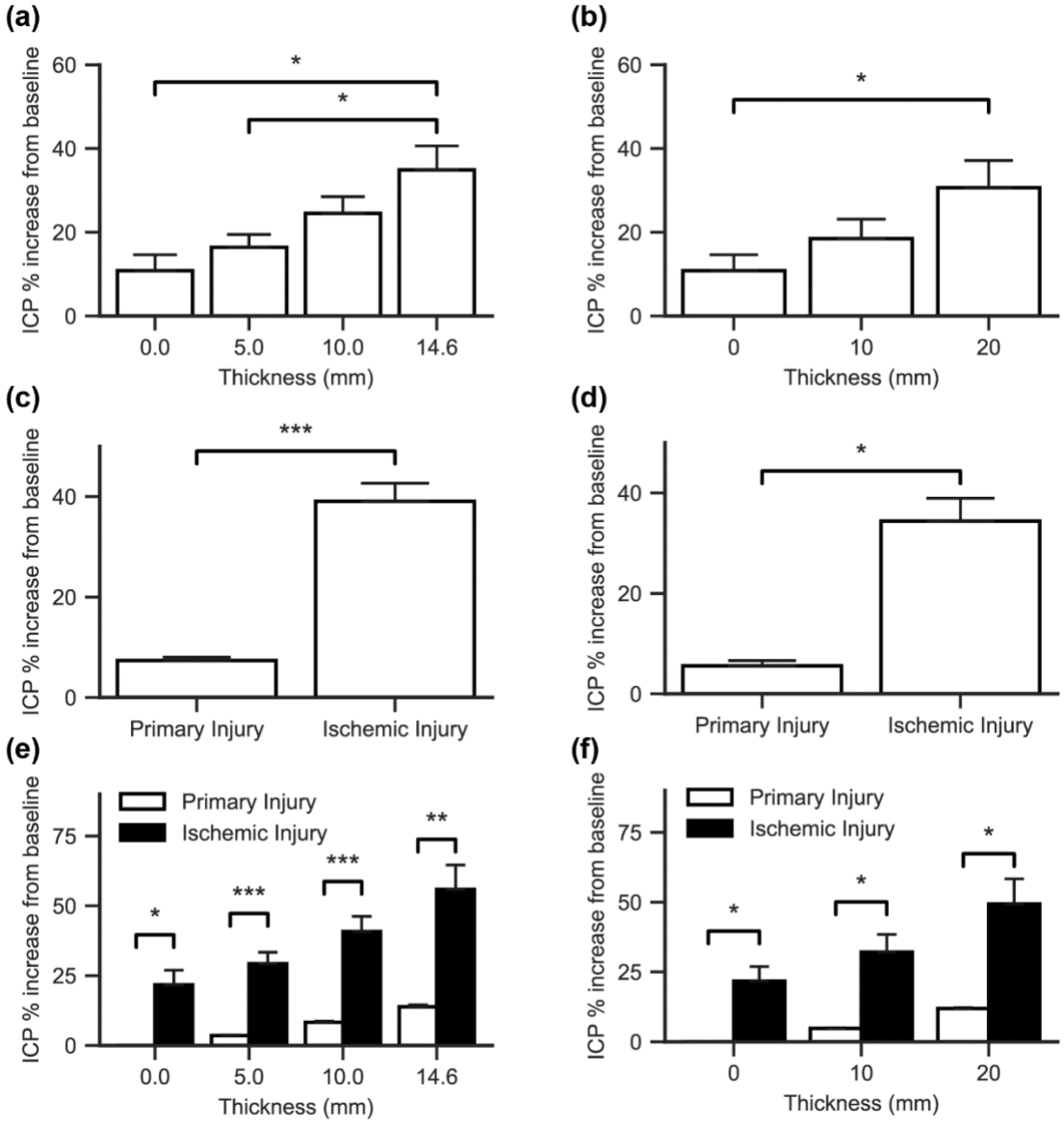

Figure 36: Simulated ICP percent increase from baseline (primary injury with a 0 mm hematoma thickness) comparing (a) the effect of hematoma volume for convexity ASDH, (b) the effect of hematoma volume for interhemispheric ASDH, (c) the effect of ischemia for convexity ASDH, (d) the effect of ischemia for interhemispheric ASDH, (e) the interaction between hematoma volume and ischemia for convexity ASDH, and (f) the interaction between hematoma volume and ischemia for interhemispheric ASDH. * $p < 0.05$, ** $p < 0.01$, *** $p < 0.001$, mean ± SEM

For convexity ASDH, as determined by the three-way ANOVA, hematoma volume and ischemic injury significantly influenced ICP, whereas the intracranial location of convexity ASDH (Type 1 vs Type 2) did not have a significant effect. The effect of hematoma volume is shown in Figure 36a. The ICP for the 14.6 mm thick hematoma was significantly greater than for both 0 mm and 5 mm thick hematomas. The effect of ischemia is shown in Figure 36c, and a closer examination of the differences between the groups in injury type and hematoma volume is shown in Figure 36e. Ischemic injury significantly increased ICP after primary injury across all hematoma thicknesses. In addition, the interaction effect of hematoma volume and ischemic injury was statistically significant. A larger hematoma volume led to worse ischemic injury.

For interhemispheric ASDH, as determined by the two-way ANOVA, both hematoma volume and ischemic injury significantly increased ICP over baseline. ICP with a 20 mm thick hematoma was significantly greater than ICP with a 0 mm thick hematoma (Figure 36b). Ischemic injury also significantly increased ICP after primary injury across all hematoma thicknesses (Figure 36d and Figure 36f). However, unlike in the case of convexity ASDH, the interaction effect of hematoma volume and ischemic injury was not statistically significant.

5.4 Discussion

The aim of this study was to determine why the presence of hematoma is associated with a higher likelihood of death. We demonstrated that convexity ASDH significantly increased ICP by exacerbating ischemic damage, which could explain how hematomas lead to increased likelihood of mortality. However, interhemispheric ASDH did not significantly exacerbate ischemia, which may explain why conservative surgical management is generally recommended for interhemispheric ASDH. Although several finite element models have been developed to

predict the occurrence of ASDH due to the rupture of bridging veins [197-199], few have examined the consequences of ASDH on subsequent secondary injury cascades such as ischemia and edema. One study created a model for ICP estimation based on the hematoma thickness and midline shift, but it only considered the immediate effect of hematoma volume on ICP [178]. However, in the clinic, it is well documented that brain swelling leads to an elevation in ICP, and the rise of ICP may be swift, occurring within 36 hours post-injury despite aggressive treatment [15]. This evolution of ICP over time emphasizes the need for a model that is capable of simulating this delayed brain swelling and the subsequent rise in ICP as brain swelling progresses. Although another study modeled cerebral edema following ischemic stroke, it was limited by the assumption that cerebral edema was assumed to be driven by an increase in blood pressure during reperfusion after thrombolytic therapy [200]. In contrast, our model simulates brain swelling by accounting for exposure of intracellular FCD due to cell death from primary injury and ischemic damage. To the best of our knowledge, this study is the first to incorporate secondary injuries such as ischemia and edema, along with a clinically accurate mass occupying effect from ASDH, to predict post-traumatic ICP.

ASDH is an acute intracranial lesion that leads to elevated ICP and is often complicated by co-existing intracranial lesions such as edema and ischemia [166]. In exercising our model, we demonstrated that the mass occupying effect of larger ASDH exacerbated ischemic damage in the surrounding tissue leading to higher ICP (Figure 36a). The importance of secondary injury processes, e.g. ischemia, is supported by an investigation of intracranial tumor growth, which reported deformation of the brain parenchyma with increased ICP [201]. Therefore, the purpose of surgery for ASDH is to prevent herniation and to reduce secondary ischemic injury [166].

In contrast to the common convexity ASDH, interhemispheric ASDH is reported to not correlate with increased ICP [202], and clinical guidelines suggest that interhemispheric ASDH may be treated conservatively in most cases, i.e. without surgical removal [169]. A more conservative approach is supported by a higher rate of functional recovery with interhemispheric ASDH than with convexity ASDH [203]. The advocated conservative surgical management for most primary interhemispheric ASDHs [168, 202] is supported by our results that the presence of an interhemispheric ASDH did not compress surrounding tissue as much as convexity ASDH to cause additional ischemic cell death or subsequent increase of ICP. The distinct effect of interhemispheric ASDH can be explained by its anatomical location which does not compress the surrounding brain tissue as much as the convexity ASDH does.

Current guidelines for surgical intervention to remove a convexity ASDH are based on the Glasgow Coma Scale score and computerized tomography (CT) findings. For example, a convexity ASDH with a thickness greater than 10 mm or a midline shift greater than 5 mm should be surgically removed [196, 204, 205]. Although midline shift was not investigated, our model did suggest that 10 mm hematoma thickness was a critical threshold for surgical evacuation (Figure 36a). The simulated ICP appreciably increased from baseline cases when hematoma thickness exceeded 10 mm. In addition to CT parameters, a patient's ICP is another indicator for surgical intervention. For comatose patients, one clinical guideline suggests that surgery should be performed if ICP exceeds 20 mmHg [206]. However, for patients with extensive primary injury, even surgical intervention may not be sufficient to reduce ICP because the contribution to elevated ICP from the hematoma (mass occupying effect and ischemia) is negligible compared to the swelling due to the cell death caused by deformation during the impact. In these situations to effectively control ICP, osmotherapy, with or without surgical

intervention, should be considered to mitigate the substantial cerebral edema resulting from the primary injury [207, 208]. Therefore, the decision for surgical intervention may depend in part on distinguishing the effect of primary injury versus secondary injury due to the hematoma and ischemic cell death on patient outcome. By simulating ischemic cell death due to hematoma with different thicknesses, our results suggest that a hematoma thickness of 10 mm is a good indicator for surgical intervention for patients with convexity ASDH. There is no comparable surgical guidance for patients with interhemispheric ASDH due to a paucity of data. However, our results suggested that an interhemispheric ASDH of 20 mm thickness should be surgically evacuated. This 20 mm threshold is supported by clinical findings that large interhemispheric ASDHs with an average hematoma thickness of 19.5 mm cause falx syndrome [203], and surgical evacuation should be performed if falx syndrome is present [209, 210].

The timing of surgery is another important factor in patient outcome. Our results suggested that prompt evacuation of the hematoma is important to rescue the brain from secondary ischemia as the progression of ischemia significantly increased ICP. Prompt removal of the hematoma is consistent with general guidance for patients with ASDH who have an indication for surgery [196, 211]. In addition, studies showed that patients who recover from injury have a shorter period between injury and surgery compared to those who have a fatal outcome, highlighting the significance of immediate evacuation of a subdural hematoma [180, 212]. However, another study reported that the timing of surgery was not statistically correlated with outcome [213]. The discrepancy could be explained by the variability in the extent of patients' primary injury. As pointed out by one study, the extent of primary injury may be substantial, making the timing of subdural blood clot removal less critical than previously thought [26]. In contrast, as also shown by our model, for those who experience less severe

primary injury, the contribution of hematoma plus ischemia is more significant, and, therefore, the timing of surgery is critical. Clinically, decompressive craniectomy is recommended when brain swelling is expected during and/or after surgery [166]. Compared to traditional craniotomy, this study showed that decompressive craniectomy significantly improved outcome in patients with refractory intracranial hypertension due to extensive contusion [214]. However, it is also worth noting that even if surgery was performed in a timely manner to suppress secondary injury from hematoma, unfavorable effects of decompressive craniectomy such as exacerbation of edema [215] or complications such as contralateral acute epidural hematoma [216] are possible risks following the removal of ASDH. Those factors could affect patient outcome and confound determining the effect of timely removal of the hematoma.

Although ASDH is a major risk factor for poor outcome, it is less clear whether the source of the hematoma, venous or arterial blood, affects patient outcome. We attempted to explore this question with the two types of convexity ASDH: Type 1 for venous rupture or Type 2 for arterial rupture. In our simulations, there was no difference in ICP between the two types of convexity ASDH modeled, suggesting that the source of blood does not affect ICP. Because the source of convexity ASDH can be determined by its location [195], we infer that there is no significant difference between convexity ASDH due to bridging vein rupture and convexity ASDH due to arterial rupture. Our simulations are supported by a study in the rat to evaluate the differences in secondary ischemic lesions caused by subdural injection of venous blood, arterial blood, or saline [210]. No difference in lesion volume or extent of brain swelling was found for arterial or venous blood [210]. Although we identified the same trend for venous and arterial convexity ASDH, our model did not take into account the physiological effect of blood constituents. Studies have shown that direct contact of blood constituents with brain cells can

induce cell death, which could contribute to a larger area of swelling and therefore ischemia [217, 218]. It was reported that thrombin, a protein involved in coagulation, is present at higher levels in tissues affected by ischemia and can have cytotoxic effects in a dose-dependent manner [217]. It was also reported that the release of carbonic anhydrase-I from damaged red blood cells can increase the permeability of the blood-brain barrier, potentially exacerbating brain swelling [218]. Therefore, future work could incorporate blood toxicity and other potential mechanisms for secondary injury such as spreading depolarization [215] into our model.

Despite the novelty of our study, there were several limitations. In our model, the size of the ASDH was based on the hematoma thickness measured from diagnostic CT scans. The geometry of the hematoma was fixed for the entire simulation including the later stage of ischemia as swelling progressed. As the brain swells, it may be possible for it to counteract the local compression by the hematoma and alter the extent of tissue displacement caused by the clot. More work will be required to investigate the interaction of forces between brain swelling and hematoma to refine our model. Another limitation of this study was the use of a maximum FCD value in the brain swelling simulation that requires more validation. The swelling pressure within an element was proportional to the amount of intracellular FCD exposed. Although our model can predict ICP, further experimental validation will be required to more precisely determine the FCD of human brain.

In summary, our model demonstrated the capability to simulate secondary injuries including cerebral edema and post-traumatic ischemia due to ASDH to predict post-traumatic ICP. We showed that the joint effect of the mass occupying effect of the blood clot and resulting ischemia contributes to elevated ICP, which could explain the underlying injury mechanism for the high mortality rate associated with traumatic ASDH.

Chapter 6: Summary and Discussion

6.1 Determining the Mechanical Properties of Brain Tissue

Traumatic brain injury (TBI) occurs when head acceleration causes large deformations of brain tissue. Computational models, which require appropriate geometry, mechanical parameters, tolerance criteria, and data validation, have been used to make predictions after injury. Prediction of the functional consequences of TBI requires accurate predictions of the distribution of stress and strain in the brain, which requires appropriate mechanical properties of the brain. The mechanical parameters necessary for populating these models, however, are lacking. In chapter 2, we sought to determine the constitutive formulation and its corresponding appropriate mechanical parameters to best model the mechanical behavior of each of the five different tested regions of the brain.

In this study, we reanalyzed data from previous work in which sections of non-sclerotic hippocampus (CA1, CA3, and dentate gyrus) and non-epileptic neocortex (cortex gray matter and cortex white matter) were taken from 11 patients of both sexes ranging in age from 4 to 58 years during surgical procedures to resect underlying epileptic foci [52]. 1 mm thick slices of tissue were indented using a cylindrical indenter with a 250 μm radius in which three consecutive indentations were performed on the sample to displacements of 40, 80, and 120 μm. During each step, the tissue sample slices were indented by 40 μm in 70 ms and held for 19.93 s to capture the stress relaxation response. A recent previous study attempted to use a quasilinear viscoelastic (QLV) model to characterize the mechanical behavior of brain tissue under large strain, but the QLV model was less optimal than the fitting of the linear viscoelastic model [53]. The limitation of this previous study, however, is that the strain used to calculate load for the

QLV model was calculated using a small strain assumption, which may not be valid for the large strains experienced in these indentation experiments. Therefore, the intent of this current study was to use an inverse FE approach and an FE solver for large nonlinear deformations, which would allow us to circumvent the small strain assumption and obtain more accurate mechanical properties.

Prior to conducting inverse FE methodology, a mesh convergence study was conducted. A mesh convergence study is required to ensure that the elements are small enough to accurately represent the spatial gradients within the mesh without introducing numerical artifacts, such as artificial stiffening of the mesh response. After determining the "ground truth" loads, we created an optimized mesh that would match the "ground truth" loads as closely as possible but with a short enough computational run time. This optimized mesh was used for all inverse FE simulations conducted in the study.

We tested the neo-Hookean, Mooney-Rivlin, and Ogden constitutive formulations to determine which of the three could model the mechanical behavior of brain tissue the best. Inverse FE simulations were conducted on experimental load data for each of the five different brain regions, and we determined that an uncoupled viscoelastic Ogden constitutive formulation best represented the mechanical behavior of brain tissue among the three constitutive formulations tested. The Ogden constitutive model has also been used to model the non-linear mechanical behavior of other soft tissues such as the liver [67], rat brain and fat tissue [68].

Functional differences in the brain tissue response as a function of sex, age, or anatomical location was assessed using optimized parameters from inverse FE simulations of each of the 73 individual experimental samples. Virtual indentations under a single large deformation were conducted using these optimized parameters, and we determined that brain anatomical region

significantly affected mechanical behavior, but age and sex did not. However, our statistical analysis was underpowered due to difficulty of obtaining sufficient human samples. In addition, we determined that cortex white matter was significantly stiffer than that of the cortex gray matter and that the CA1 was significantly stiffer than the cortex gray matter. Overall, the findings in this study may assist in improving computational FE head models by providing more accurate mechanical properties to make better predictions following TBI.

The overall purpose of this thesis was to present a new FE model and methodology to better predict patient outcome following TBI. An advantage of our model is that we can incorporate ischemic injury, cerebral edema, and ASDH into our predictions of patient outcome, in addition to studying the stresses and strains that occur in the brain during primary injury at the moment of impact. Automotive safety engineers currently only model primary injury during FE simulations of impact, which may lead to drastically inaccurate results of patient outcome following TBI. The work presented in chapter 2 of this thesis is paramount for making accurate predictions of patient outcome following TBI because the appropriate constitutive formulation for brain tissue, along with its associated mechanical parameters, not only affects the resulting strain field of the brain tissue during TBI but also affects the pattern and magnitude of the resulting cerebral edema which influences ICP. Because we predict patient mortality using ICP, accurately predicting the resulting swelling profile is necessary. Different mechanical properties would alter the MPS experienced per element for a given loading condition, which would influence how much FCD is assigned to each element. Different mechanical properties would also lead to different degrees of compression and swelling for each element, which would lead to different amounts of cell death during ischemic injury, leading to different values of FCD assigned to each element, ultimately altering the swelling profile of the brain. Therefore, we

hope that the mechanical properties determined in chapter 2 of this thesis improve current FE head models used in the automotive industry to predict stresses and strains during primary injury and lay the foundation for future work that will use the new FE head model and methodology developed in this thesis to accurately predict ICP.

However, determination of the appropriate constitutive formulation and its associated mechanical parameters for each part of the brain is not sufficient for modeling the resulting swelling profile of the brain following TBI. Because we hypothesize that the brain swelling profile is dependent upon the degree of FCD exposure that is based on the actual value of FCD content within human brain tissue, it is necessary to measure the actual value of FCD content within human brain tissue so that this value can be incorporated into the computational methodology. The actual FCD content of human brain tissue still remains uncertain. In chapter 3 of this thesis summarized in the following section, we calculated the FCD content of rat and pig brain tissue, demonstrating the possibility of calculating FCD of human brain tissue in future experiments. Determining the amount of FCD within human brain tissue is necessary for our FE model to make accurate predictions of brain swelling and resulting ICP.

6.2 Measuring the FCD of Brain Tissue

Accurate strains and accurate values of FCD are both required to correctly model the post-traumatic swelling response using our head model and novel computational methodology. The work presented in chapter 2 sought to determine the appropriate constitutive model and associated mechanical parameters of different regions of brain tissue to more accurately predict strains experienced within the brain during a loading event, while the work presented in chapter

3 sought to measure the FCD in brain tissue and provide support that cerebral edema is caused by the exposure of intercellular FCD during cell death.

We constructed a device to measure the confined swelling pressure of rat and pig brain tissue samples. Using the Gibbs-Donnan equation (Equation 1), we calculated FCD from the measured confined swelling pressure of the tissue samples. Interestingly, when we treated rat brain tissue samples with a cocktail of FCD-cleaving enzymes, the calculated maximum FCD did not significantly differ from the calculated maximum FCD without enzymes. One potential explanation is that we calculated FCD content of the sample based on its confined swelling pressure, and the enzymes were so large that they did not have adequate time to diffuse throughout the thickness of the brain tissue sample within the average time period that the brain samples reached maximum swelling pressure (usually within 1-2 hours). However, the effect of the FCD-cleaving enzymes became apparent after maximum swelling pressure was attained, especially at 16 hours after application of tare load, when swelling pressure and calculated FCD content were significantly lower after enzyme treatment.

Confined swelling experiments were also conducted on pig cortex white matter and pig cortex gray matter to compare differences in FCD. Cortex gray matter produced higher swelling pressures, indicating higher amounts of FCD within cortex gray matter compared to cortex white matter. This finding is important, as it reveals that the amount of FCD within the cortex gray matter and cortex white matter of human brain may also differ. The amount of FCD within different regions of the brain such as the thalamus, corpus callosum, cerebellum, and brain stem along with other regions might also be different. Therefore, accurate modeling of cerebral edema and accurate predictions of ICP and mortality will require determining the amount of

FCD for all parts of the human brain capable of swelling so that these values can be incorporated for each part of the brain within FE head models.

To test whether swelling and FCD exposure was due to cell death, rat brain samples were placed in Triton X-100 for at least 2 hours before measuring confined swelling pressure. The average confined swelling pressure of this group was nearly zero, indicating that the Triton X-100 must have killed all cells, exposing all intracellular FCD and preventing any further swelling from occurring once these samples were tested using our device.

Taken together, the results from this study, in addition to studies by Elkin *et al.* [20, 21], provide strong evidence that exposure of intracellular FCD due to cell death is responsible for brain swelling and that swelling can potentially be modeled using principles of triphasic mixture theory in rat brains, indicating that brain swelling of human brain tissue may occur through the same mechanism. Although only rat brain tissue and pig brain tissue were tested in this study, this work demonstrates the plausibility of using our methodology to measure the FCD content of human brain tissue in the near future, assuming that human brain also swells by the same mechanism, which will be important for accurately modeling the brain swelling profile within FE head models following TBI.

The work conducted in chapter 2 and chapter 3 of this thesis are significant in that they provide the foundation necessary for modeling cerebral edema and predicting mortality from ICP using FE head models. Chapter 2 provided the constitutive formulation and associated mechanical properties of brain that are required for accurately modeling the strain response of the brain during primary injury and the strain response of the brain due to swelling. These mechanical properties affect the strains within each element for a given loading condition. The work presented in chapter 3 demonstrated that swelling may be explained by exposure of

intracellular FCD during cell death, showing that swelling could potentially be modeled in FE head models using concepts from triphasic mixture theory. This work also showed that calculating the total amount of FCD of brain is possible if cerebral edema can be modeled using triphasic mixture theory. The cumulative results from the work conducted in these chapters demonstrate that modeling cerebral edema within an FE head model that contains triphasic material formulations is possible if strains within an element can be related to amount of cell death within that element, which would ultimately be related to the amount of exposed FCD that is assigned to that element. Thus, the work conducted in chapter 4 summarized in the following section presents our attempt to model cerebral edema within an FE head model by utilizing concepts from the prior two chapters.

6.3 Modeling Post-Traumatic Cerebral Edema in FEBio

In chapter 4, we modeled post-traumatic cerebral edema in a FE head model using FEBio. Modeling the pattern and magnitude of the resulting swelling after TBI is important, as it allows for calculation of ICP which could lead to better predictions of patient outcome after injury.

The skull and brain elements from the GHBMC model were extracted and imported into FEBio. Swelling elements in FEBio were redefined as being triphasic ("multiphasic-fcd") while matching their original GHBMC Kelvin-Maxwell viscoelastic mechanical properties. All 2D shell brain domains in FEBio were also assigned identical material properties and thickness as in the GHBMC model.

Brain swelling was modeled using the principles of triphasic mixture theory, since our work in chapter 3 along with work by Elkin *et al.* [20, 21] supports that brain swelling is caused

by the exposure of FCD during cell death. FCD was assumed to be -60 mEq/L and FCD for each element was related to cell death. In our model, cell death can be caused by either strain or ischemic damage due to compaction. To model swelling due to primary injury, we related MPS to cell death and damage using data from the literature, which in turn was related to the amount of FCD that would be assigned to the element. Swelling due to ischemic injury was modeled in a similar fashion, but by relating volume compaction of an element (measured by its volume ratio after a completed swelling simulation) to cell death using data from the literature. ICP was calculated as the volume averaged 3rd principal stress of all multiphasic elements within the model at the end of the swelling simulation. We found that ICP was directly proportional to the severity of the primary injury and that with head injury cases designated as "fatal" produced ICP values that were larger that head injury cases that were designated as "severe". We also found that swelling due to both ischemic and primary injury caused significant increases in ICP compared to ICP values produced from the primary injury alone.

Severity of impact following TBI is typically evaluated by tissue-level injury predictors such as maximum principal strain (MPS) or the cumulative strain damage measure (CSDM) [37]. Several studies have compared the injury probability predicted using this procedure to real-world injury rates determined from accident data for Abbreviated Injury Scale (AIS) 2 to 4 injuries, but none of them have evaluated its ability to predict fatality [37, 39-41]. The culmination of work conducted in chapters 2 and 3 in this thesis allowed for the development of the FE head model and computational methodology presented in chapter 4, which may aid in the ability to better predict patient outcome after TBI. The ability of our head model to simulate swelling and predict ICP coupled with injury evaluation metrics that focus on primary injury currently used in the automotive industry may lead to even better predictions of patient outcome following TBI

and lead to the development of better automotive safety systems. In chapter 5 summarized in the following section, we attempted to model hematomas, a common comorbidity in TBI, and their subsequent effects on cerebral edema and ICP using our new FE model, which, to our knowledge, has never been attempted.

6.4 Traumatic Acute Subdural Hematoma (ASDH) Exacerbates Ischemic Injury

Acute subdural hematoma (ASDH) is one of the most devastating consequences after head injury, leading to mortality rates as high as 90% [162, 170-174]. Despite ASDH's association with high mortality and its prevalence following TBI, its exact mechanism is unknown. In chapter 5, we demonstrated that convexity ASDH significantly increased ICP by exacerbating ischemic injury, but in cases where primary injury is very severe, surgical intervention to remove the clot may not effectively decrease ICP, since the major contributing factor towards increasing ICP in these cases is from the primary injury.

To conduct this study, we used the same model presented in chapter 4 with a few additional modifications. One such modification was the replacement of CSF elements, originally modeled as a strain-stiffening Holmes-Mow material, with empty space to better represent resorption of fluid over the time course of brain swelling and to facilitate modeling of ASDH. Modeling of ASDH while the CSF elements were still present caused initial convergence issues because the CSF elements were tied to both the pia and cerebrum-arachnoid, causing difficulties when attempting to displace the cerebrum-arachnoid to model a blood clot. After the CSF elements were replaced with empty space, contacts were established between the pia and cerebrum-arachnoid. Multiple additional contacts were also added to the model.

Two common types of convexity ASDH were modeled: type 1. a convexity ASDH typically caused by bridging vein rupture in the frontoparasagittal region which spreads over the frontal and parietal lobes, and type 2. a convexity ASDH typically caused by arterial ruptures in the temporoparietal region located on the temporal lobe [195]. To investigate the relationship between hematoma thickness and ICP, these two types of hematoma were modeled with prescribed displacements of 0 mm, 5 mm, 10 mm, and 14.6 mm to simulate different hematoma thicknesses. An interhemispheric ASDH was also modeled, with thicknesses of 0 mm, 10 mm, and 20 mm.

Eight different crash scenarios, each representing a different injury severity, were examined in this study. ICP was normalized to the ICP from its corresponding baseline case (0 mm hematoma without ischemic secondary injury). We found that hematoma volume and ischemic injury significantly influenced ICP, whereas the intracranial location of convexity ASDH (type 1 vs. type 2) did not have a significant effect. Ischemic injury significantly increased ICP after primary injury across all hematoma thicknesses and a larger hematoma volume led to worse ischemic injury. We also found that ischemic injury significantly increased ICP after primary injury across all interhemispheric hematoma thicknesses. However, in cases of interhemispheric ASDH, the interaction affect between hematoma thickness and ischemia was absent, indicating the convexity ASDH is more likely to increase ICP and mortality rate by exacerbating ischemic injury compared to similarly sized interhemispheric ASDH.

To the best of our knowledge, this study is the first to model ASDH, ischemia, and their subsequent effects on the pattern and magnitude of brain swelling after injury. By incorporating ASDH into our head model of swelling, we have demonstrated that ASDH leads to an increase in ICP by exacerbating ischemic damage, which may explain why mortality rates are elevated with

the presence of ASDH. This work is interesting in that it is the first study conducted using our model developed in chapter 4. Although more work is required to confirm the mechanical properties determined from our study and determine the FCD content of human brain tissue, this work is significant in that it combines the complex interactions among primary injury, ischemia, cerebral edema, and ASDH with the potential to predict patient outcome.

6.5 Limitations

The study presented in chapter 2 contains several limitations. Due to the difficulties of procuring human brain tissue, the observations made in this study were confined to a small samples size, which may have led to under-powered statistical tests. Conducting experiments on more human samples would alleviate this issue. Another limitation occurred in the procedure used to determine the dependency of human brain mechanical properties on anatomical region, sex, or age. To determine loads, a virtual indentation using optimized mechanical parameters was simulated and the load at 70 ms was extracted from each simulation for comparison. The simulated virtual indentation, however, simulated a single large deformation while optimized parameters were determined by fitting to experimental loads from a triple indentation displacement profile. Future experimental validation is needed to determine the validity of extrapolating optimized mechanical parameters from three smaller cumulative indentations to a single large deformation. Another limitation of our study is that tissue underneath the indenter was assumed to be isotropic. White matter is structurally anisotropic and may therefore also be mechanically anisotropic, meaning that extracted optimized mechanical parameters from the cortex white matter using our inverse FE methodology would need to be orientation-specific when applied to FE models, otherwise predicted strains using an FE head model would be

incorrect. Serious brain pathologies after head injury include diffuse axonal injury in which axons become strained. Orientation-specific mechanical properties of white matter are vital for predicting accurate strains in axons within the white matter that could lead to diffuse axonal injury. Therefore, conducting orientation-specific indentation tests on cortex white matter, as well as other parts of the brain, could help determine mechanical parameters that are more appropriate depending on the loading orientation upon the tissue. Another potential limitation is that the indenter was displaced at an averaged maximum Lagrange shear strain rate of 0.79 s^{-1} to 3.57 s^{-1}, but strain rates during TBI are on the order of 10 s^{-1}. Despite this seemingly low strain rate, our study still utilizes strain rates that are faster than those applied in some other studies that also measure brain mechanical properties.

In chapter 3, we constructed a device to calculate the fixed-charge density (FCD) of brain tissue by measuring confined brain swelling pressure. FCD of brain tissue was calculated using the measured maximum swelling pressure of the sample. However, the measured maximum swelling pressure might not reveal the true maximum FCD content within the tissue. We noticed that brain samples typically swelled within 1-2 hours following the application of a tare load until reaching a maximum value, but swelling pressure slowly decreased afterwards. This indicated that the measured swelling pressure was potentially due to net effect resulting from two competing phenomena: FCD exposure leading to increased swelling and FCD cleavage, possibly due to endogenous enzymes, leading to decreased swelling. Within the 1- to 2-hour time period that was required for the tissue sample to reach maximum swelling pressure, some FCD may have been cleaved by endogenous enzymes and leaked out of the tissue into the surrounding bath, indicating that the measured maximum swelling pressure used to calculate FCD content may underestimate the true FCD content within the tissue sample. One potential method to

prevent endogenous enzymatic degradation of intracellular FCD is to heat the tissue while measuring its swelling pressure using our custom device. Elevated temperatures may facilitate denaturation of endogenous enzymes that degrade intracellular FCD, which may eliminate leakage of FCD from the tissue sample that could contribute to lower swelling pressures and lower FCD measurements. Another potential solution is to use a cocktail of inhibitors to inhibit the enzymatic activity of these endogenous enzymes. Another limitation of this study is that the process of extracting rat brain and obtaining an adequately-sized sample to test using our custom device required at least 15 minutes, at best. During that time period of at least 15 minutes, brain cells began to die from lack of blood flow, which in turn caused FCD to be exposed, drawing in water intracellularly causing swelling. Extracting brain tissue from pigs required even longer periods of time compared to extraction of rat brain due to the much thicker and larger pig skulls. The time period between animal sacrifice and brain sample testing most likely reduced the amount of FCD left over to be exposed within the brain tissue, leading to swelling pressures and FCD measurements that may underestimate the true FCD content within the tissue sample. Perhaps the main limitation of this thesis is that the FCD content of human tissue was not measured, but the work in this thesis lays the necessary ground work for working with very limited samples of human tissue. Future studies are required to determine the FCD content of human brain tissue so that it can be incorporated into our FE head model.

In chapter 4, we created the first FE computational head model, to our knowledge, that simulates the pattern and magnitude of brain swelling resulting from the unique loading conditions of the primary injury. Although the results of this work are exciting, there were a few limitations in this study. Any uncertainties in reconstructing a crash-scenario associated with the accelerations used as input to the GHBMC model will affect the fidelity of our predictions.

Predictions of the resulting swelling profile, ICP, and mortality are ultimately dependent on MPS values calculated from the GHBMC model. Any uncertainties that arise from using the GHBMC model to predict strains on a per element basis would propagate into our model and ultimately affect the resulting swelling profile. Further validation of the GHBMC model itself could ultimately aid in any predictions that our model makes. Our model also makes predictions of brain swelling based on relationships between MPS and cell death and between ischemia and cell death. These relationships may require adjustment as more validation data is reported in the literature in the future. Another limitation of this work is that it does not take into account injury due to hematomas, which may drastically affect patient outcome following primary injury. However, initial incorporation of hematomas using our model is addressed in chapter 5. As mentioned before, perhaps the largest limitation of this work is that actual FCD values of human brain tissue were not incorporated into this study. Furthermore, we assumed that the maximum FCD of all brain parts within our head model was -60 mEq/L, which was another limitation because the work conducted in chapter 3 revealed that FCD content between pig cortex gray matter and cortex white matter were different. This implies that FCD content might also vary among different regions of the human brain. To our knowledge, no work has been conducted to determine the amount of FCD within human brain tissue. Experiments to determine the amount of FCD within human brain tissue is therefore necessary for future work.

In chapter 5, we incorporated hematomas into our FE head model and novel computational methodology constructed in chapter 4 to answer why the presence of hematomas is associated with a much higher likelihood of mortality. An advantage of our model is that we can observe how hematomas and cerebral edema interact to affect ICP. However, our study does have some limitations. The size of the ASDH in our model was based on hematoma thickness

measured from diagnostic CT scans, and geometry of the hematoma was fixed during the entire swelling process. CT scans are usually taken immediately after an injury. In reality, the swelling brain may counteract the local compression caused by the blood clot, reducing the extent of brain tissue compression. Further modification of our model that accounts for the competing forces between the blood clot and brain swelling should be incorporated in the future. Another limitation of this study was the use of a maximum FCD value in our brain swelling simulation that requires more validation. Because swelling pressure within an element was proportional to the amount of exposed FCD, incorporating the actual FCD value found in human brain tissue into our computational model is necessary to make accurate predictions of ICP and patient outcome. In chapter 3 of this thesis, we measured the FCD content of rat and pig brain tissue. However, the FCD content of human brain tissue may be different. Future studies elucidating the FCD content of human brain tissue is necessary, especially across different parts of the brain. Another limitation of this study is the use of using thickness as an independent variable to assess outcome and the effects of hematoma on ICP. In the clinic, hematoma thickness is usually reported because measuring hematoma volumes is difficult. In this study, we varied thickness by uniformly applying the same prescribed displacement along the entire length of the hematoma, and observed its effects on ICP. However, varying hematoma thicknesses in the clinic does not necessarily mean that the volume is proportionally changing by the same amount. A hematoma with a greater thickness at one end but a lesser thickness at the opposite end might actually have the same volume as a separate hematoma with a smaller reported thickness. This limitation needs to be considered if hematoma volume has a greater effect on ICP increase than thickness of the hematoma. Future work may need to be conducted to consider the effects of varying hematoma volumes on ICP.

6.6 Future Directions

In chapter 2, the appropriate constitutive formulation and associated mechanical properties of various parts of human brain tissue were elucidated using inverse FE methodology on prior indentation experiments conducted in our lab. However, the sample sizes in this study were low due to difficulty of procuring human brain tissue. In the future, more human brain samples should be tested to either confirm or counter our results. Indentation experimentation should also be conducted on the brain stem or other regions deep within the brain which influence patient outcome when injured following TBI. Brainstem involvement in severe TBI can lead to devastating long-term effects on patient outcome such as visual impairment, spasticity, coordination deficiency, and organic psychosis [219], while injury to deeper parts of the brain such as the thalamus may lead to deficits in executive function, attention, and memory [220]. Thus, identifying the constitutive formulation and associated mechanical parameters for the remaining parts of the brain not included in this thesis may further enhance the ability of computational FE head models to make better predictions of patient outcome following TBI. Obtaining fresh tissue samples from live patients from certain regions of the brain such as the brainstem will be difficult because removing this tissue from a patient would lead to severe complications or even death. At best, brainstem tissue samples would need to be obtained from patients who have recently died. Indentation experiments should also be conducted on human brain in multiple orientations to determine whether the mechanical response of a particular region of the brain is orientation-dependent. Assuming isotropic mechanical behavior for a part of the brain that is mechanically anisotropic may lead to inaccurate predictions of the resulting strain field within the brain after an induced load. Future studies should also be conducted to determine the validity of extrapolating experimental fitting data from three smaller cumulative

indentations to a single, large virtual indentation and to test the tissues under different loading conditions such as shear and tension to show that the material properties deduced in chapter 2 are valid under different loading conditions.

In chapter 3, the FCD content of rat and pig brain was measured, and we showed that cleavage of FCD led to a decrease in brain swelling pressure, supporting that cerebral edema is caused by the exposure of intracellular FCD and subsequent intracellular water influx during cell death. FCD was calculated by measuring the confined swelling pressure of brain tissue using our custom device. FCD content of the brain tissue sample, whether from rat or pig, was calculated using the maximum confined swelling pressure of the brain tissue sample. Maximum swelling pressure typically occurred within 1-2 hours after the sample was loaded into our custom device. We originally expected confined swelling pressure to reach a maximum value and remain sustained. However, following maximum swelling, we observed a decrease in swelling pressure, indicating that FCD was most likely degrading and diffusing out of the brain tissue sample and into the surrounding bath. Measured swelling pressure, therefore, may have actually been a net pressure generated by FCD exposure and FCD leakage. The maximum swelling pressure, and therefore, the corresponding maximum FCD calculation, was most likely not the true maximum for the brain samples tested in this study. Future experiments should include a procedure to prevent the endogenous enzymatic degradation of intracellular FCD by either heating the tissue to adequately high temperatures to denature these enzymes or by adding a cocktail of enzymatic inhibitors to prevent digestion and subsequent leakage of FCD from the tissue. If FCD leakage is successfully eliminated, then the maximum swelling pressure measurement, and hence the maximum FCD content of the brain tissue, can be determined. Experiments should also be conducted on human brain tissue in the future because FCD content of human brain tissue may

differ from rat or pig brain. Experiments should also be conducted on all parts of the human brain as well. Since we have shown that pig cortex gray matter and pig cortex white matter contain different amounts of FCD, different parts of human brain may also contain varying amounts of FCD.

In chapter 4, we created a novel computational methodology to model cerebral edema. Swelling was modeled using principles from triphasic mixture theory in which FCD exposure, dependent on cell death from either elemental MPS or volume ratio compaction, affected the osmotic pressure responsible for driving influx of water. The parameters relating MPS or volume ratio compaction to cell death should be updated as new parameters populate the literature in the future. Our FE head model simulations can further be refined in the future by incorporating hematoma following primary injury, since the presence of hematoma is associated with a significantly higher likelihood of mortality. Hematoma location is dependent upon which bridging vein exceeds its ultimate strain, so our modeling methodology will need to calculate the maximum strain for each bridging vein in the model, and apply a prescribed displacement to the region underneath the bridging vein that exceeds its ultimate strain. Hematoma size and shape should also be modeled accurately, if it can be predicted. Hematoma size could possibly be modeled by relating its predicted size to how much a particular bridging vein's ultimate strain is exceeded during the primary injury.

It is hoped that the work presented in this thesis ultimately leads to better engineered technologies to reduce to societal impact of TBI. Perhaps in the future, as more accurate mechanical parameters and FCD values are incorporated into our head model and meshing methodologies become more efficient, focus can be shifted into making our model more individualized and patient-specific by taking into account a patient's unique cranial volume,

bridging vein number and geometry, medical history, and risk factors. Once our model becomes more accurate, it could extend beyond the automotive industry and impact clinical applications as well.

References

1. Ghajar, J., *Traumatic brain injury.* The Lancet, 2000. **356**(9233): p. 923-929.

2. Bruns Jr, J. and W.A. Hauser, *The epidemiology of traumatic brain injury: a review.* Epilepsia, 2003. **44**: p. 2-10.

3. Langlois, J.A., W. Rutland-Brown, and K.E. Thomas, *Traumatic brain injury in the United States; emergency department visits, hospitalizations, and deaths.* 2006.

4. Taylor, C.A., J.M. Bell, M.J. Breiding, and L. Xu, *Traumatic Brain Injury-Related Emergency Department Visits, Hospitalizations, and Deaths-United States, 2007 and 2013.* Morbidity and mortality weekly report. Surveillance summaries (Washington, DC: 2002), 2017. **66**(9): p. 1-16.

5. van Dijck, J.T., M.D. Dijkman, R.H. Ophuis, G.C. de Ruiter, W.C. Peul, and S. Polinder, *In-hospital costs after severe traumatic brain injury: a systematic review and quality assessment.* PLoS One, 2019. **14**(5): p. e0216743.

6. Thompson, K., A. Antony, and A. Holtzman, *The costs of traumatic brain injury.* North Carolina medical journal, 2001. **62**(6): p. 376-379.

7. Brener, I., J.S. Harman, K.J. Kelleher, and K.O. Yeates, *Medical costs of mild to moderate traumatic brain injury in children.* The Journal of head trauma rehabilitation, 2004. **19**(5): p. 405-412.

8. Levin, H.S. and R.R. Diaz-Arrastia, *Diagnosis, prognosis, and clinical management of mild traumatic brain injury.* The Lancet Neurology, 2015. **14**(5): p. 506-517.

9. Graham, N.S., A. Jolly, K. Zimmerman, N.J. Bourke, G. Scott, J.H. Cole, J.M. Schott, and D.J. Sharp, *Diffuse axonal injury predicts neurodegeneration after moderate–severe traumatic brain injury.* Brain, 2020. **143**(12): p. 3685-3698.

10. Budday, S., R. Nay, R. de Rooij, P. Steinmann, T. Wyrobek, T.C. Ovaert, and E. Kuhl, *Mechanical properties of gray and white matter brain tissue by indentation.* Journal of the mechanical behavior of biomedical materials, 2015. **46**: p. 318-330.

11. MacManus, D.B., J.G. Murphy, and M.D. Gilchrist, *Mechanical characterisation of brain tissue up to 35% strain at 1, 10, and 100/s using a custom-built micro-indentation apparatus.* Journal of the mechanical behavior of biomedical materials, 2018. **87**: p. 256-266.

12. Van Dommelen, J., T. Van der Sande, M. Hrapko, and G. Peters, *Mechanical properties of brain tissue by indentation: interregional variation.* Journal of the mechanical behavior of biomedical materials, 2010. **3**(2): p. 158-166.

13. Jha, R.M., P.M. Kochanek, and J.M. Simard, *Pathophysiology and treatment of cerebral edema in traumatic brain injury.* Neuropharmacology, 2019. **145**: p. 230-246.

14. Unterberg, A., J. Stover, B. Kress, and K. Kiening, *Edema and brain trauma.* Neuroscience, 2004. **129**(4): p. 1019-1027.

15. Marmarou, A., *A review of progress in understanding the pathophysiology and treatment of brain edema.* Neurosurgical focus, 2007. **22**(5): p. 1-10.

16. Thorén, M., E. Azevedo, J. Dawson, J.A. Egido, A. Falcou, G.A. Ford, S. Holmin, R. Mikulik, J. Ollikainen, and N. Wahlgren, *Predictors for cerebral edema in acute ischemic stroke treated with intravenous thrombolysis.* Stroke, 2017. **48**(9): p. 2464-2471.

17. Bereczki, D.n., M. Liu, G.F.d. Prado, and I.n. Fekete, *Cochrane report: a systematic review of mannitol therapy for acute ischemic stroke and cerebral parenchymal hemorrhage.* Stroke, 2000. **31**(11): p. 2719-2722.

18. Wakai, A., I.G. Roberts, and G. Schierhout, *Mannitol for acute traumatic brain injury.* Cochrane Database of Systematic Reviews, 2005(4).

19. Lai, W.M., J. Hou, and V.C. Mow, *A triphasic theory for the swelling and deformation behaviors of articular cartilage.* Journal of Biomechanical Engineering, 1991. **113**(3): p. 245-258.

20. Elkin, B.S., M.A. Shaik, and B. Morrison, *Fixed negative charge and the Donnan effect: a description of the driving forces associated with brain tissue swelling and oedema.* Philosophical Transactions of the Royal Society of London A: Mathematical, Physical and Engineering Sciences, 2010. **368**(1912): p. 585-603.

21. Elkin, B.S., M.A. Shaik, and B. Morrison III, *Chondroitinase ABC reduces brain tissue swelling in vitro.* Journal of neurotrauma, 2011. **28**(11): p. 2277-2285.

22. Monson, K.L., M.I. Converse, and G.T. Manley, *Cerebral blood vessel damage in traumatic brain injury.* Clinical biomechanics, 2019. **64**: p. 98-113.

23. Parikh, S., M. Koch, and R.K. Narayan, *Traumatic brain injury.* International anesthesiology clinics, 2007. **45**(3): p. 119-135.

24. Gennarelli, T.A. and L.E. Thibault, *Biomechanics of acute subdural hematoma.* The Journal of trauma, 1982. **22**(8): p. 680-686.

25. Alagoz, F., A. Yildirim, M. Sahinoglu, M. Korkmaz, M. Secer, H. Celik, C. Yel, Y. Guvenc, O. Uckun, and F. Narin, *Traumatic acute subdural hematomas: analysis of outcomes and predictive factors at a single center.* Turkish neurosurgery, 2017. **27**(2).

26. Wilberger, J.E., M. Harris, and D.L. Diamond, *Acute subdural hematoma: morbidity, mortality, and operative timing.* Journal of neurosurgery, 1991. **74**(2): p. 212-218.

27. McLaurin, R.L. and F.T. Tutor, *Acute subdural hematoma: review of ninety cases.* Journal of Neurosurgery, 1961. **18**(1): p. 61-67.

28. Hlatky, R., A.B. Valadka, J.C. Goodman, and C.S. Robertson, *Evolution of brain tissue injury after evacuation of acute traumatic subdural hematomas.* Neurosurgery, 2004. **55**(6): p. 1318-1324.

29. Gennarelli, T.A., G.M. Spielman, T.W. Langfitt, P.L. Gildenberg, T. Harrington, J.A. Jane, L.F. Marshall, J.D. Miller, and L.H. Pitts, *Influence of the type of intracranial lesion on outcome from severe head injury: a multicenter study using a new classification system.* Journal of neurosurgery, 1982. **56**(1): p. 26-32.

30. Fell, D.A., S. Fitzgerald, R.H. Moiel, and P. Caram, *Acute subdural hematomas: Review of 144 cases.* Journal of neurosurgery, 1975. **42**(1): p. 37-42.

31. Sándor, J., M. Szücs, I. Kiss, I. Ember, G. Csepregi, J. Futó, L. Vimláti, J. Pál, A. Büki, and T. Dóczi, *Risk factors for fatal outcome in subdural hemorrhage.* Ideggyogyaszati szemle, 2003. **56**(11-12): p. 386-395.

32. Depreitere, B., C. Van Lierde, J. Vander Sloten, R. Van Audekercke, G. Van Der Perre, C. Plets, and J. Goffin, *Mechanics of acute subdural hematomas resulting from bridging vein rupture.* Journal of neurosurgery, 2006. **104**(6): p. 950-956.

33. Pierre, L. and N.P. Kondamudi, *Subdural Hematoma.* StatPearls [Internet], 2020.

34. Sucu, H.K., F. Gelal, M. Gökmen, F.D. Özer, and Ş. Tektaş, *Can midline brain shift be used as a prognostic factor to predict postoperative restoration of consciousness in patients with chronic subdural hematoma?* Surgical neurology, 2006. **66**(2): p. 178-182.

35. Hossmann, K.-A., *Pathophysiology and therapy of experimental stroke.* Cellular and molecular neurobiology, 2006. **26**(7-8): p. 1055-1081.

36. Ayata, C. and A.H. Ropper, *Ischaemic brain oedema.* Journal of Clinical Neuroscience, 2002. **9**(2): p. 113-124.

37. Takahashi, Y., T. Yanaoka, H. Sugaya, A.V. Basilio, P. Xu, G. Ateshian, and B. Morrison III, *Prediction of probability of fatality due to brain injury in traffic accidents.* Traffic injury prevention, 2019. **20**(sup1): p. S27-S31.

38. Takhounts, E.G., M.J. Craig, K. Moorhouse, J. McFadden, and V. Hasija, *Development of brain injury criteria (BrIC)*. 2013, SAE Technical Paper.

39. Laituri, T.R., S. Henry, K. Pline, G. Li, M. Frankstein, and P. Weerappuli, *New risk curves for NHTSA's brain injury criterion (BrIC): derivations and assessments*. 2016, SAE Technical Paper.

40. Mueller, B., A. MacAlister, J. Nolan, and D. Zuby. *Comparison of HIC and BrIC head injury risk in IIHS frontal crash tests to real-world head injuries*. in *Proceedings of the 24th International Technical Conference On The Enhanced Safety of Vehicles*. 2015.

41. Prasad, P., D. Dalmotas, and A. German, *The field relevance of NHTSA's oblique research moving deformable barrier tests.* Stapp. Car Crash J, 2014. **58**: p. 175-195.

42. Greve, M.W. and B.J. Zink, *Pathophysiology of traumatic brain injury.* Mount Sinai Journal of Medicine: A Journal of Translational and Personalized Medicine: A Journal of Translational and Personalized Medicine, 2009. **76**(2): p. 97-104.

43. Balestreri, M., M. Czosnyka, P. Hutchinson, L.A. Steiner, M. Hiler, P. Smielewski, and J.D. Pickard, *Impact of intracranial pressure and cerebral perfusion pressure on severe disability and mortality after head injury.* Neurocritical care, 2006. **4**(1): p. 8-13.

44. Badri, S., J. Chen, J. Barber, N.R. Temkin, S.S. Dikmen, R.M. Chesnut, S. Deem, N.D. Yanez, and M.M. Treggiari, *Mortality and long-term functional outcome associated with intracranial pressure after traumatic brain injury.* Intensive care medicine, 2012. **38**(11): p. 1800-1809.

45. Control, C.f.D. and Prevention, *Report to congress on traumatic brain injury in the United States: epidemiology and rehabilitation.* National Center for Injury Prevention and Control, 2015. **2**: p. 1-72.

46. Riggio, S. and M. Wong, *Neurobehavioral sequelae of traumatic brain injury.* Mount Sinai Journal of Medicine: A Journal of Translational and Personalized Medicine: A Journal of Translational and Personalized Medicine, 2009. **76**(2): p. 163-172.

47. Walker, W.C. and T.C. Pickett, *Motor impairment after severe traumatic brain injury: A longitudinal multicenter study.* Journal of Rehabilitation Research & Development, 2007. **44**(7).

48. McAllister, T.W. and D. Arciniegas, *Evaluation and treatment of postconcussive symptoms.* NeuroRehabilitation, 2002. **17**(4): p. 265-283.

49. Elkin, B.S., A.I. Ilankovan, and B. Morrison III, *A detailed viscoelastic characterization of the P17 and adult rat brain.* Journal of neurotrauma, 2011. **28**(11): p. 2235-2244.

50. Elkin, B.S., A. Ilankovan, and B. Morrison III, *Age-dependent regional mechanical properties of the rat hippocampus and cortex.* Journal of Biomechanical Engineering, 2010. 132(1)

51. Finan, J.D., B.S. Elkin, E.M. Pearson, I.L. Kalbian, and B. Morrison, *Viscoelastic properties of the rat brain in the sagittal plane: effects of anatomical structure and age.* Annals of biomedical engineering, 2012. **40**(1): p. 70-78.

52. Finan, J.D., S.N. Sundaresh, B.S. Elkin, G.M. McKhann II, and B. Morrison III, *Regional mechanical properties of human brain tissue for computational models of traumatic brain injury.* Acta biomaterialia, 2017. **55**: p. 333-339.

53. Sundaresh, S.N., J.D. Finan, B.S. Elkin, A.V. Basilio, G.M. McKhann, and B. Morrison, *Region-Dependent Viscoelastic Properties of Human Brain Tissue Under Large Deformations.* Annals of Biomedical Engineering, 2022. **50**(11): p. 1425-1460.

54. Garo, A., M. Hrapko, J. Van Dommelen, and G. Peters, *Towards a reliable characterisation of the mechanical behaviour of brain tissue: the effects of post-mortem time and sample preparation.* Biorheology, 2007. **44**(1): p. 51-58.

55. Maas, S.A., B.J. Ellis, G.A. Ateshian, and J.A. Weiss, *FEBio: finite elements for biomechanics.* Journal of biomechanical engineering, 2012. **134**(1).

56. Ateshian, G.A., S. Maas, and J.A. Weiss, *Multiphasic finite element framework for modeling hydrated mixtures with multiple neutral and charged solutes.* Journal of biomechanical engineering, 2013. **135**(11).

57. M.I.A Lourakis. *levmar: Levenberg-Marquardt nonlinear least squares algorithms in {C}/{C}++*. 2004 [cited 2023; Available from: http://users.ics.forth.gr/~lourakis/levmar/.

58. Menichetti, A., D.B. MacManus, M.D. Gilchrist, B. Depreitere, J. Vander Sloten, and N. Famaey, *Regional characterization of the dynamic mechanical properties of human brain tissue by microindentation.* International Journal of Engineering Science, 2020. **155**: p. 103355.

59. Jin, X., F. Zhu, H. Mao, M. Shen, and K.H. Yang, *A comprehensive experimental study on material properties of human brain tissue.* Journal of biomechanics, 2013. **46**(16): p. 2795-2801.

60. Bayly, P., L. Taber, and C. Kroenke, *Mechanical forces in cerebral cortical folding: a review of measurements and models.* Journal of the mechanical behavior of biomedical materials, 2014. **29**: p. 568-581.

61. Christ, A.F., K. Franze, H. Gautier, P. Moshayedi, J. Fawcett, R.J. Franklin, R.T. Karadottir, and J. Guck, *Mechanical difference between white and gray matter in the rat cerebellum measured by scanning force microscopy.* Journal of biomechanics, 2010. **43**(15): p. 2986-2992.

62. Green, M.A., L.E. Bilston, and R. Sinkus, *In vivo brain viscoelastic properties measured by magnetic resonance elastography.* NMR in Biomedicine: An International Journal

Devoted to the Development and Application of Magnetic Resonance In vivo, 2008. **21**(7): p. 755-764.

63. Daugherty, A.M., H.D. Schwarb, M.D. McGarry, C.L. Johnson, and N.J. Cohen, *Magnetic resonance elastography of human hippocampal subfields: CA3-dentate gyrus viscoelasticity predicts relational memory accuracy.* Journal of cognitive neuroscience, 2020. **32**(9): p. 1704-1713.

64. Takhounts, E.G., S.A. Ridella, V. Hasija, R.E. Tannous, J.Q. Campbell, D. Malone, K. Danelson, J. Stitzel, S. Rowson, and S. Duma, *Investigation of traumatic brain injuries using the next generation of simulated injury monitor (SIMon) finite element head model.* Stapp car crash journal, 2008. **52**: p. 1.

65. Laksari, K., M. Shafieian, and K. Darvish, *Constitutive model for brain tissue under finite compression.* Journal of biomechanics, 2012. **45**(4): p. 642-646.

66. Prange, M. and D.F. Meaney, *Defining brain mechanical properties: effects of region, direction, and species*. 2000, SAE Technical Paper.

67. Hu, T. and J.P. Desai. *Characterization of soft-tissue material properties: large deformation analysis*. in *International Symposium on Medical Simulation*. 2004. Springer.

68. Mihai, L.A., L. Chin, P.A. Janmey, and A. Goriely, *A comparison of hyperelastic constitutive models applicable to brain and fat tissues.* Journal of The Royal Society Interface, 2015. **12**(110): p. 20150486.

69. Gennatas, E.D., B.B. Avants, D.H. Wolf, T.D. Satterthwaite, K. Ruparel, R. Ciric, H. Hakonarson, R.E. Gur, and R.C. Gur, *Age-related effects and sex differences in gray matter density, volume, mass, and cortical thickness from childhood to young adulthood.* Journal of Neuroscience, 2017. **37**(20): p. 5065-5073.

70. Gur, R.C. and R.E. Gur, *Complementarity of sex differences in brain and behavior: From laterality to multimodal neuroimaging.* Journal of neuroscience research, 2017. **95**(1-2): p. 189-199.

71. Gur, R.C., B.I. Turetsky, M. Matsui, M. Yan, W. Bilker, P. Hughett, and R.E. Gur, *Sex differences in brain gray and white matter in healthy young adults: correlations with cognitive performance.* Journal of Neuroscience, 1999. **19**(10): p. 4065-4072.

72. Chatelin, S., J. Vappou, S. Roth, J.-S. Raul, and R. Willinger, *Towards child versus adult brain mechanical properties.* Journal of the mechanical behavior of biomedical materials, 2012. **6**: p. 166-173.

73. Elkin, B.S. and B. Morrison, *Viscoelastic properties of the P17 and adult rat brain from indentation in the coronal plane.* Journal of biomechanical engineering, 2013. **135**(11).

74. Thibault, K.L. and S.S. Margulies, *Age-dependent material properties of the porcine cerebrum: effect on pediatric inertial head injury criteria.* Journal of biomechanics, 1998. **31**(12): p. 1119-1126.

75. Witelson, S., H. Beresh, and D. Kigar, *Intelligence and brain size in 100 postmortem brains: sex, lateralization and age factors.* Brain, 2006. **129**(2): p. 386-398.

76. Eskandari, F., M. Shafieian, M.M. Aghdam, and K. Laksari, *Structural anisotropy vs. mechanical anisotropy: the contribution of axonal fibers to the material properties of brain white matter.* Annals of Biomedical Engineering, 2021. **49**(3): p. 991-999.

77. Sahoo, D., C. Deck, and R. Willinger, *Brain injury tolerance limit based on computation of axonal strain.* Accident Analysis & Prevention, 2016. **92**: p. 53-70.

78. Margulies, S.S. and L.E. Thibault, *An analytical model of traumatic diffuse brain injury.* Journal of Biomechanical Engineering, 1989. **111**(3): p. 241-249.

79. Zhou, C., T.B. Khalil, and A.I. King, *A new model comparing impact responses of the homogeneous and inhomogeneous human brain.* SAE transactions, 1995: p. 2999-3015.

80. Claessens, M., F. Sauren, and J. Wismans, *Modeling of the human head under impact conditions: a parametric study.* SAE transactions, 1997: p. 3829-3848.

81. Zhang, L., K.H. Yang, and A.I. King, *A proposed injury threshold for mild traumatic brain injury.* J. Biomech. Eng., 2004. **126**(2): p. 226-236.

82. Kruse, S.A., G.H. Rose, K.J. Glaser, A. Manduca, J.P. Felmlee, C.R. Jack Jr, and R.L. Ehman, *Magnetic resonance elastography of the brain.* Neuroimage, 2008. **39**(1): p. 231-237.

83. Prange, M.T. and S.S. Margulies, *Regional, directional, and age-dependent properties of the brain undergoing large deformation.* Journal of biomechanical engineering, 2002. **124**(2): p. 244-252.

84. Gefen, A. and S.S. Margulies, *Are in vivo and in situ brain tissues mechanically similar?* Journal of biomechanics, 2004. **37**(9): p. 1339-1352.

85. Velardi, F., F. Fraternali, and M. Angelillo, *Anisotropic constitutive equations and experimental tensile behavior of brain tissue.* Biomechanics and modeling in mechanobiology, 2006. **5**(1): p. 53-61.

86. Feng, Y., C.-H. Lee, L. Sun, S. Ji, and X. Zhao, *Characterizing white matter tissue in large strain via asymmetric indentation and inverse finite element modeling.* Journal of the mechanical behavior of biomedical materials, 2017. **65**: p. 490-501.

87. Tiesman, H.M., S. Konda, and J.L. Bell, *The epidemiology of fatal occupational traumatic brain injury in the US.* American journal of preventive medicine, 2011. **41**(1): p. 61-67.

88. Rutland-Brown, W., J.A. Langlois, K.E. Thomas, and Y.L. Xi, *Incidence of traumatic brain injury in the United States, 2003.* The Journal of head trauma rehabilitation, 2006. **21**(6): p. 544-548.

89. Ray, S., C. Dixon, and N. Banik, *Molecular mechanisms in the pathogenesis of traumatic brain injury.* Histology and histopathology, 2002. **17**(4): p. 1137-1152

90. Davis, A.E., *Mechanisms of traumatic brain injury: biomechanical, structural and cellular considerations.* Critical care nursing quarterly, 2000. **23**(3): p. 1-13.

91. Stokum, J.A., V. Gerzanich, and J.M. Simard, *Molecular pathophysiology of cerebral edema.* Journal of Cerebral Blood Flow & Metabolism, 2016. **36**(3): p. 513-538.

92. Feickert, H.-J., S. Drommer, and R. Heyer, *Severe head injury in children: impact of risk factors on outcome.* Journal of Trauma and Acute Care Surgery, 1999. **47**(1): p. 33-38.

93. Donkin, J.J. and R. Vink, *Mechanisms of cerebral edema in traumatic brain injury: therapeutic developments.* Current opinion in neurology, 2010. **23**(3): p. 293-299.

94. Forsyth, L.L., X. Liu-DeRyke, D. Parker Jr, and D.H. Rhoney, *Role of hypertonic saline for the management of intracranial hypertension after stroke and traumatic brain injury.* Pharmacotherapy: The Journal of Human Pharmacology and Drug Therapy, 2008. **28**(4): p. 469-484.

95. White, H., D. Cook, and B. Venkatesh, *The use of hypertonic saline for treating intracranial hypertension after traumatic brain injury.* Anesthesia & Analgesia, 2006. **102**(6): p. 1836-1846.

96. Diringer, M.N., M.T. Scalfani, A.R. Zazulia, T.O. Videen, R. Dhar, and W.J. Powers, *Effect of mannitol on cerebral blood volume in patients with head injury.* Neurosurgery, 2012. **70**(5): p. 1215.

97. Shawkat, H., M.-M. Westwood, and A. Mortimer, *Mannitol: a review of its clinical uses.* Continuing education in anaesthesia, critical care & pain, 2012. **12**(2): p. 82-85.

98. Fink, M.E., *Osmotherapy for intracranial hypertension: mannitol versus hypertonic saline.* CONTINUUM: Lifelong Learning in Neurology, 2012. **18**(3): p. 640-654.

99. Kolias, A.G., E. Viaroli, A.M. Rubiano, H. Adams, T. Khan, D. Gupta, A. Adeleye, C. Iaccarino, F. Servadei, and B.I. Devi, *The current status of decompressive craniectomy in traumatic brain injury.* Current trauma reports, 2018. **4**: p. 326-332.

100. Stiver, S.I., *Complications of decompressive craniectomy for traumatic brain injury.* Neurosurgical focus, 2009. **26**(6): p. E7.

101. Tasker, R.C. and C.L. Acerini, *Cerebral edema in children with diabetic ketoacidosis: vasogenic rather than cellular?* Pediatric diabetes, 2014. **15**(4): p. 261-270.

102. Rungta, R.L., H.B. Choi, J.R. Tyson, A. Malik, L. Dissing-Olesen, P.J. Lin, S.M. Cain, P.R. Cullis, T.P. Snutch, and B.A. MacVicar, *The cellular mechanisms of neuronal swelling underlying cytotoxic edema.* Cell, 2015. **161**(3): p. 610-621.

103. Marmarou, A., S. Signoretti, G. Aygok, P. Fatouros, and G. Portella. *Traumatic brain edema in diffuse and focal injury: cellular or vasogenic?* in *Brain Edema XIII*. 2006. Springer.

104. Portella, G., A. Beaumont, F. Corwin, P. Fatouros, and A. Marmarou. *Characterizing edema associated with cortical contusion and secondary insult using magnetic resonance spectroscopy*. in *Brain Edema XI: Proceedings of the 11th International Symposium, Newcastle-upon-Tyne, United Kingdom, June 6–10, 1999*. 2000. Springer.

105. Liang, D., S. Bhatta, V. Gerzanich, and J.M. Simard, *Cytotoxic edema: mechanisms of pathological cell swelling.* Neurosurgical focus, 2007. **22**(5): p. 1-9.

106. Lu, X.L., C. Miller, F.H. Chen, X.E. Guo, and V.C. Mow, *The generalized triphasic correspondence principle for simultaneous determination of the mechanical properties and proteoglycan content of articular cartilage by indentation.* Journal of biomechanics, 2007. **40**(11): p. 2434-2441.

107. Azeloglu, E.U., M.B. Albro, V.A. Thimmappa, G.A. Ateshian, and K.D. Costa, *Heterogeneous transmural proteoglycan distribution provides a mechanism for regulating residual stresses in the aorta.* American Journal of Physiology-Heart and Circulatory Physiology, 2008. **294**(3): p. H1197-H1205.

108. Westheimer, F.H., *Why nature chose phosphates.* Science, 1987. **235**(4793): p. 1173-1178.

109. Kurbel, S., *Are extracellular osmolality and sodium concentration determined by Donnan effects of intracellular protein charges and of pumped sodium?* Journal of Theoretical Biology, 2008. **252**(4): p. 769-772.

110. Sarrazin, S., W.C. Lamanna, and J.D. Esko, *Heparan sulfate proteoglycans.* Cold Spring Harbor perspectives in biology, 2011. **3**(7): p. a004952.

111. Dyck, S.M. and S. Karimi-Abdolrezaee, *Chondroitin sulfate proteoglycans: key modulators in the developing and pathologic central nervous system.* Experimental neurology, 2015. **269**: p. 169-187.

112. Yao, H. and W.Y. Gu, *The effects of porosity and fixed charge density on hydraulic permeability of cartilage.* 2003 Summer Bioengineering Conference.

113. Zhao, R.-R. and J.W. Fawcett, *Combination treatment with chondroitinase ABC in spinal cord injury—breaking the barrier.* Neuroscience bulletin, 2013. **29**: p. 477-483.

114. Boyce, A. and G. Walsh, *Production, characteristics and applications of microbial heparinases.* Biochimie, 2022. **198**: p. 109-140.

115. Herculano-Houzel, S., B. Mota, and R. Lent, *Cellular scaling rules for rodent brains.* Proceedings of the National Academy of Sciences, 2006. **103**(32): p. 12138-12143.

116. Aquino, D., R. Margolis, and R. Margolis, *Immunocytochemical localization of a chondroitin sulfate proteoglycan in nervous tissue. I. Adult brain, retina, and peripheral nerve.* The Journal of cell biology, 1984. **99**(3): p. 1117-1129.

117. Margolis, R., M. Thomas, C. Crockett, and R. Margolis, *Presence of chondroitin sulfate in the neuronal cytoplasm.* Proceedings of the National Academy of Sciences, 1979. **76**(4): p. 1711-1715.

118. Lundgaard, I., M.J. Osório, B. Kress, S. Sanggaard, and M. Nedergaard, *White matter astrocytes in health and disease.* Neuroscience, 2014. **276**: p. 161-173.

119. Bailey, D.M., *Oxygen and brain death; back from the brink.* Experimental Physiology, 2019. **104**(12): p. 1769-1779.

120. Lee, J.-M., M.C. Grabb, G.J. Zipfel, and D.W. Choi, *Brain tissue responses to ischemia.* The Journal of clinical investigation, 2000. **106**(6): p. 723-731.

121. DeSai, C. and A. Hays Shapshak, *Cerebral Ischemia*. 2022: StatPearls Publishing, Treasure Island (FL).

122. Hou, S.T. and J.P. MacManus, *Molecular mechanisms of cerebral ischemia-induced neuronal death.* International review of cytology, 2002. **221**: p. 93-148.

123. Fritz, J., E.B. Cooper, S. Gaudet, P.K. Sorger, and S.R. Manalis, *Electronic detection of DNA by its intrinsic molecular charge.* Proceedings of the National Academy of sciences, 2002. **99**(22): p. 14142-14146.

124. Basilio, A.V., P. Xu, Y. Takahashi, T. Yanaoka, H. Sugaya, G.A. Ateshian, and B. Morrison III, *Simulating cerebral edema and delayed fatality after traumatic brain injury using triphasic swelling biomechanics.* Traffic injury prevention, 2019. **20**(8): p. 820-825.

125. Langlois, J.A., W. Rutland-Brown, and M.M. Wald, *The epidemiology and impact of traumatic brain injury: a brief overview.* The Journal of head trauma rehabilitation, 2006. **21**(5): p. 375-378.

126. Arun, M.W., J.R. Humm, N. Yoganandan, and F.A. Pintar. *Biofidelity evaluation of a restrained whole body finite element model under frontal impact using kinematics data from PMHS sled tests*. in *IRCOBI Conference Proceedings*. 2015.

127. Talebanpour, A. and L. Smith. *A Comparison between Simulated and Measured Human Brain Response under Mild Acceleration*. in *IRCOBI Conference Proceedings*. 2017.

128. Marmarou, A., R.L. Anderson, J.D. Ward, S.C. Choi, H.F. Young, H.M. Eisenberg, M.A. Foulkes, L.F. Marshall, and J.A. Jane, *Impact of ICP instability and hypotension on outcome in patients with severe head trauma.* Journal of Neurosurgery, 1991. **75**: p. S59-S66.

129. Fahlstedt, M., B. Depreitere, P. Halldin, J. Vander Sloten, and S. Kleiven, *Correlation between injury pattern and Finite Element analysis in biomechanical reconstructions of Traumatic Brain Injuries.* J Biomech, 2015. **48**(7): p. 1331-5.

130. Kleiven, S., *Predictors for traumatic brain injuries evaluated through accident reconstructions.* Stapp Car Crash Journal, 2007. **51**: p. 81-114.

131. Mao, H., L. Zhang, B. Jiang, V.V. Genthikatti, X. Jin, F. Zhu, R. Makwana, A. Gill, G. Jandir, A. Singh, and K.H. Yang, *Development of a finite element human head model partially validated with thirty five experimental cases.* J Biomech Eng, 2013. **135**(11): p. 111002.

132. Ji, S., H. Ghadyani, R.P. Bolander, J.G. Beckwith, J.C. Ford, T.W. McAllister, L.A. Flashman, K.D. Paulsen, K. Ernstrom, S. Jain, R. Raman, L. Zhang, and R.M. Greenwald, *Parametric comparisons of intracranial mechanical responses from three validated finite element models of the human head.* Ann Biomed Eng, 2014. **42**(1): p. 11-24.

133. Czosnyka, M., J. Pickard, and L. Steiner, *Principles of intracranial pressure monitoring and treatment.* Handbook of clinical neurology, 2017. **140**: p. 67-89.

134. MacGregor, D.G., M.V. Avshalumov, and M.E. Rice, *Brain edema induced by in vitro ischemia: causal factors and neuroprotection.* Journal of Neurochemistry, 2003. **85**(6): p. 1402-1411.

135. Overbeek, J.T., *The Donnan equilibrium.* Prog Biophys Biophys Chem, 1956. **6**: p. 57-84.

136. Bilston, L.E., *Brain tissue mechanical properties*, in *Biomechanics of the brain*. 2011, Springer. p. 69-89.

137. Ewing, C.L., D.J. Thomas, L. Lustic, G.C. Willems, W.H. Muzzy, E.B. Becker, and M.E. Jessop, *Dynamic response of human and primates head and neck to +Gy impact acceleration*. 1978, National Highway Traffic Safety Administration, US Department of Transportation: Washington, DC.

138. Drake, A.M., E.G. Takhounts, and V. Hasija, *Investigation of parameters affecting brain model validation and brain strains using the SIMon finite element head model.* IRCOBI Conference Proceedings, 2017.

139. Bain, A.C. and D.F. Meaney, *Tissue-level thresholds for axonal damage in an experimental model of central nervous system white matter injury.* J. Biomech. Eng., 2000. **122**(6): p. 615-622.

140. Cargill, R.S. and L.E. Thibault, *Acute alterations in [Ca2+] i in NG108-15 cells subjected to high strain rate deformation and chemical hypoxia: an in vitro model for neural trauma.* Journal of neurotrauma, 1996. **13**(7): p. 395-407.

141. Cater, H.L., L.E. Sundstrom, and B. Morrison III, *Temporal development of hippocampal cell death is dependent on tissue strain but not strain rate.* Journal of biomechanics, 2006. **39**(15): p. 2810-2818.

142. Elkin, B.S. and B. Morrison III, *Region-specific tolerance criteria for the living brain.* Stapp Car Crash Journal, 2007. **51**: p. 127-138.

143. Galbraith, J., L. Thibault, and D. Matteson, *Mechanical and electrical responses of the squid giant axon to simple elongation.* Journal of Biomechanical Engineering, 1993. **115**(1): p. 13-22.

144. Geddes, D.M. and R.S. Cargill, *An in vitro model of neural trauma: device characterization and calcium response to mechanical stretch.* Journal of Biomechanical Engineering, 2001. **123**(3): p. 247-255.

145. Geddes, D.M., R.S. Cargill, and M.C. LaPlaca, *Mechanical stretch to neurons results in a strain rate and magnitude-dependent increase in plasma membrane permeability.* Journal of neurotrauma, 2003. **20**(10): p. 1039-1049.

146. Geddes, D.M., M.C. LaPlaca, and R.S. Cargill II, *Susceptibility of hippocampal neurons to mechanically induced injury.* Experimental neurology, 2003. **184**(1): p. 420-427.

147. LaPlaca, M.C., D.K. Cullen, J.J. McLoughlin, and R.S. Cargill II, *High rate shear strain of three-dimensional neural cell cultures: a new in vitro traumatic brain injury model.* Journal of biomechanics, 2005. **38**(5): p. 1093-1105.

148. LaPlaca, M.C., V.M.-Y. LEE, and L.E. Thibault, *An in vitro model of traumatic neuronal injury: loading rate-dependent changes in acute cytosolic calcium and lactate dehydrogenase release.* Journal of neurotrauma, 1997. **14**(6): p. 355-368.

149. Lusardi, T.A., J.A. Wolf, M.E. Putt, D.H. Smith, and D.F. Meaney, *Effect of acute calcium influx after mechanical stretch injury in vitro on the viability of hippocampal neurons.* Journal of neurotrauma, 2004. **21**(1): p. 61-72.

150. Morrison III, B., H.L. Cater, C.D. Benham, and L.E. Sundstrom, *An in vitro model of traumatic brain injury utilising two-dimensional stretch of organotypic hippocampal slice cultures.* Journal of neuroscience methods, 2006. **150**(2): p. 192-201.

151. Morrison III, B., H.L. Cater, C.B. Wang, F.C. Thomas, C.T. Hung, G.A. Ateshian, and L.E. Sundstrom, *A tissue level tolerance criteria for living brain developed with an in vitro model of traumatic mechanical loading.* Stapp Car Crash Journal, 2003. **47**: p. 93-105.

152. Shreiber, D.I., A.C. Bain, and D.F. Meaney, *In vivo thresholds for mechanical injury to the blood-brain barrier.* SAE transactions, 1997: p. 3792-3806.

153. Heilig, C.W., M.E. Stromski, J.D. Blumenfeld, J.P. Lee, and S.R. Gullans, *Characterization of the major brain osmolytes that accumulate in salt-loaded rats.* Am.J.Physiol, 1989. **257**(6 Pt 2): p. F1108-F1116.

154. Kawamata, T., T. Mori, S. Sato, and Y. Katayama, *Tissue hyperosmolality and brain edema in cerebral contusion.* Neurosurgical focus, 2007. **22**(5): p. 1-8.

155. Tomita, M., F. Gotoh, and M. Kobari, *Colloid osmotic pressure of cat brain homogenate separated from autogenous CSF by a copper ferrocyanide membrane.* Brain Research, 1988. **474**(1): p. 165-173.

156. Baron, J.-C., *Perfusion thresholds in human cerebral ischemia: historical perspective and therapeutic implications.* Cerebrovascular Diseases, 2001. **11**(Suppl. 1): p. 2-8.

157. Zhang, L., K.H. Yang, and A.I. King, *Comparison of brain responses between frontal and lateral impacts by finite element modeling.* Journal of neurotrauma, 2001. **18**(1): p. 21-30.

158. Yao, J., J. Yang, and D. Otte, *Investigation of head injuries by reconstructions of real-world vehicle-versus-adult-pedestrian accidents.* Safety science, 2008. **46**(7): p. 1103-1114.

159. Takahashi, Y. and T. Yanaoka. *A Study of Injury Criteria for Brain Injuries in Traffic Accidents*. in *25th International Technical Conference on the Enhanced Safety of Vehicles (ESV) National Highway Traffic Safety Administration*. 2017.

160. Gong, C., N. Boulis, J. Qian, D.E. Turner, J.T. Hoff, and R.F. Keep, *Intracerebral hemorrhage-induced neuronal death.* Neurosurgery, 2001. **48**(4): p. 875-883.

161. Moussa, W.M.M., W.M. Khedr, and A.H. Elwany, *Prognostic significance of hematoma thickness to midline shift ratio in patients with acute intracranial subdural hematoma: a retrospective study.* Neurosurgical review, 2018. **41**: p. 483-488.

162. de Souza, M.R., C.F. Fagundes, D.J.F. Solla, G.C.L. da Silva, R.B. Barreto, M.J. Teixeira, R.L.O. de Amorim, A.G. Kolias, D. Godoy, and W.S. Paiva, *Mismatch between midline shift and hematoma thickness as a prognostic factor of mortality in patients sustaining acute subdural hematoma.* Trauma Surgery & Acute Care Open, 2021. **6**(1): p. e000707.

163. Xian, L., C. Wang, W. Wang, L. Wei, Y. Zhang, W. Chen, and S. Wang, *The construction of an improved model of acute subdural hematoma in rats.* Journal of Neuroscience Methods, 2021. **351**: p. 109075.

164. Yanagawa, T., K. Yamashita, Y. Harada, T. Hatayama, and T. Kono, *Location of hemorrhage with nontraumatic acute subdural hematoma due to ruptured microaneurysm.* Surgical Neurology International, 2021. **12**.

165. Lim, M., S. Kheok, K. Lim, N. Venkatanarasimha, J. Small, and R. Chen, *Subdural haematoma mimics.* Clinical Radiology, 2019. **74**(9): p. 663-675.

166. Karibe, H., T. Hayashi, T. Hirano, M. Kameyama, A. Nakagawa, and T. Tominaga, *Surgical management of traumatic acute subdural hematoma in adults: a review.* Neurologia medico-chirurgica, 2014: p. cr. 2014-0204.

167. Bartels, R.H., W.I. Verhagen, M.J. Prick, and J.E. Dalman, *Interhemispheric subdural hematoma in adults: case reports and a review of the literature.* Neurosurgery, 1995. **36**(6): p. 1210-1214.

168. Fruin, A.H., G.L. Juhl, and C. Taylon, *Interhemispheric subdural hematoma: Case report.* Journal of neurosurgery, 1984. **60**(6): p. 1300-1302.

169. Takeuchi, S., Y. Takasato, H. Masaoka, T. Hayakawa, H. Yatsushige, and T. Sugawara, *Traumatic interhemispheric subdural haematoma: Study of 35 cases.* Journal of Clinical Neuroscience, 2010. **17**(12): p. 1527-1529.

170. AbdelFatah, M.A.R., *Prognosis of acute subdural hematoma greater than 10 mm in thickness in head injury patients with an extension or no motor response to pain after resuscitation.* Egyptian Journal of Neurosurgery, 2019. **34**(1): p. 1-5.

171. Bartels, R.H., F.J. Meijer, H. van der Hoeven, M. Edwards, and M. Prokop, *Midline shift in relation to thickness of traumatic acute subdural hematoma predicts mortality.* BMC neurology, 2015. **15**(1): p. 1-6.

172. D'amato, L., O. Piazza, L. Alliata, G. Sabia, G. Zito, L. Frassanito, F. Della Corte, and R. Tufano, *post-traumatic subdural haematoma.* J Neurosurg Sci, 2007. **51**: p. 00-00.

173. Ozpinar, A. and B. Jankowitz, *Clinical Aspects of Subdural Hemorrhage (SDH)*, in *Primer on Cerebrovascular Diseases*. 2017, Elsevier. p. 467-471.

174. Vega, R.A. and A.B. Valadka, *Natural history of acute subdural hematoma.* Neurosurgery Clinics, 2017. **28**(2): p. 247-255.

175. Davis, M., Larry E, M. Pirio Richardson, Assistant Professor, Sarah, L.E. Davis, and S. Pirio Richardson, *Traumatic Brain Injury and Subdural Hematoma.* Fundamentals of Neurologic Disease, 2015: p. 225-233.

176. Hamahata, N.T. and K. Nakagawa, *Regional cerebral hypoperfusion from acute subdural hematoma.* Neurocritical care, 2020. **32**(2): p. 633-635.

177. Kiyohira, M., E. Suehiro, Y. Fujiyama, and M. Suzuki, *Predictive factors of intracranial pressure elevation in patients with severe acute subdural hematoma.* No Shinkei geka. Neurological Surgery, 2019. **47**(7): p. 753-760.

178. Liao, C.-C., H.-C. Liao, F. Lai, and F. Xiao, *A nomogram for estimating intracranial pressure using acute subdural hematoma thickness and midline shift.* Scientific Reports, 2020. **10**(1): p. 21787.

179. Miller, J.D., R. Bullock, D.I. Graham, J.F. Soustiel, and G.M. Teasdale, *Ischemic brain damage in a model of acute subdural hematoma.* Neurosurgery, 1990. **27**(3): p. 433-439.

180. Seelig, J.M., D.P. Becker, J.D. Miller, R.P. Greenberg, J.D. Ward, and S.C. Choi, *Traumatic acute subdural hematoma: major mortality reduction in comatose patients treated within four hours.* New England Journal of Medicine, 1981. **304**(25): p. 1511-1518.

181. Thirugnanachandran, T., H. Ma, S. Singhal, L.-A. Slater, S.M. Davis, G.A. Donnan, and T. Phan, *Refining the ischemic penumbra with topography.* International Journal of Stroke, 2018. **13**(3): p. 277-284.

182. Pulli, B., P.W. Schaefer, R. Hakimelahi, Z.A. Chaudhry, M.H. Lev, J.A. Hirsch, R.G. González, and A.J. Yoo, *Acute ischemic stroke: infarct core estimation on CT angiography source images depends on CT angiography protocol.* Radiology, 2012. **262**(2): p. 593-604.

183. Heiss, W.-D. and R. Graf, *The ischemic penumbra.* Current opinion in neurology, 1994. **7**(1): p. 11-19.

184. Lee, D.H., D.-W. Kang, J.S. Ahn, C.G. Choi, S.J. Kim, and D.C. Suh, *Imaging of the ischemic penumbra in acute stroke.* Korean journal of radiology, 2005. **6**(2): p. 64-74.

185. Guadagno, J.V., P.S. Jones, T.D. Fryer, O. Barret, F.I. Aigbirhio, T.A. Carpenter, C.J. Price, J.H. Gillard, E.A. Warburton, and J.-C. Baron, *Local relationships between*

restricted water diffusion and oxygen consumption in the ischemic human brain. Stroke, 2006. **37**(7): p. 1741-1748.

186. Chiu, F.-Y., D.-P. Kuo, Y.-C. Chen, Y.-C. Kao, H.-W. Chung, and C.-Y. Chen, *Diffusion tensor-derived properties of benign oligemia, true "at risk" penumbra, and infarct core during the first three hours of stroke onset: a rat model.* Korean journal of radiology, 2018. **19**(6): p. 1161-1171.

187. Koike, M.A., K.N. Green, M. Blurton-Jones, and F.M. LaFerla, *Oligemic hypoperfusion differentially affects tau and amyloid-β.* The American journal of pathology, 2010. **177**(1): p. 300-310.

188. Schlaug, G., A. Benfield, A. Baird, B. Siewert, K. Lövblad, R. Parker, R. Edelman, and S. Warach, *The ischemic penumbra: operationally defined by diffusion and perfusion MRI.* Neurology, 1999. **53**(7): p. 1528-1528.

189. Rami, A. and D. Kögel, *Apoptosis meets autophagy-like cell death in the ischemic penumbra: Two sides of the same coin?* Autophagy, 2008. **4**(4): p. 422-426.

190. Mies, G., S. Ishimaru, Y. Xie, K. Seo, and K.-A. Hossmann, *Ischemic thresholds of cerebral protein synthesis and energy state following middle cerebral artery occlusion in rat.* Journal of Cerebral Blood Flow & Metabolism, 1991. **11**(5): p. 753-761.

191. Hossmann, K.A., *Viability thresholds and the penumbra of focal ischemia.* Annals of Neurology: Official Journal of the American Neurological Association and the Child Neurology Society, 1994. **36**(4): p. 557-565.

192. Heiss, W.D., *The ischemic penumbra: how does tissue injury evolve?* Annals of the New York Academy of Sciences, 2012. **1268**(1): p. 26-34.

193. Li, Y., C. Powers, N. Jiang, and M. Chopp, *Intact, injured, necrotic and apoptotic cells after focal cerebral ischemia in the rat.* Journal of the neurological sciences, 1998. **156**(2): p. 119-132.

194. Lipton, P., *Ischemic cell death in brain neurons.* Physiological reviews, 1999. **79**(4): p. 1431-1568.

195. Maxeiner, H. and M. Wolff, *Pure subdural hematomas: a postmortem analysis of their form and bleeding points.* Neurosurgery, 2002. **50**(3): p. 503-509.

196. Bullock, M.R., R. Chesnut, J. Ghajar, D. Gordon, R. Hartl, D.W. Newell, F. Servadei, B.C. Walters, and J.E. Wilberger, *Surgical management of acute subdural hematomas.* Neurosurgery, 2006. **58**(suppl_3): p. S2-16-S2-24.

197. Costa, J.M., F.A. Fernandes, and R.J.A. de Sousa, *Prediction of subdural haematoma based on a detailed numerical model of the cerebral bridging veins.* Journal of the Mechanical Behavior of Biomedical Materials, 2020. **111**: p. 103976.

198. Cui, Z.Y., N. Famaey, B. Depreitere, J. Ivens, S. Kleiven, and J. Vander Sloten, *On the assessment of bridging vein rupture associated acute subdural hematoma through finite element analysis.* Computer methods in biomechanics and biomedical engineering, 2017. **20**(5): p. 530-539.

199. Migueis, G., F. Fernandes, M. Ptak, M. Ratajczak, and R.A. de Sousa, *Detection of bridging veins rupture and subdural haematoma onset using a finite element head model.* Clinical Biomechanics, 2019. **63**: p. 104-111.

200. Chen, X., T.I. Józsa, and S.J. Payne, *Computational modelling of cerebral oedema and osmotherapy following ischaemic stroke.* Computers in Biology and Medicine, 2022. **151**: p. 106226.

201. Ahmed, A., M.U. UlHaq, Z. Mustansar, A. Shaukat, and L. Margetts, *How growing tumour impacts intracranial pressure and deformation mechanics of brain.* Royal Society open science, 2021. **8**(9): p. 210165.

202. Wu, C., Y. Liu, and C. Yang, *Unusual cause of interhemispheric subdural hematoma: A case report.* Neurosurgery Quarterly, 2015. **25**(4): p. 436-438.

203. Tonetti, D.A., W.J. Ares, D.O. Okonkwo, and P.A. Gardner, *Management and outcomes of isolated interhemispheric subdural hematomas associated with falx syndrome.* Journal of Neurosurgery, 2019. **131**(6): p. 1920-1925.

204. Mathew, P., D. Oluoch-Olunya, B. Condon, and R. Bullock, *Acute subdural haematoma in the conscious patient: outcome with initial non-operative management.* Acta neurochirurgica, 1993. **121**: p. 100-108.

205. Wong, D.K., F. Lurie, and L.L. Wong, *The effects of clopidogrel on elderly traumatic brain injured patients.* Journal of Trauma and Acute Care Surgery, 2008. **65**(6): p. 1303-1308.

206. Servadei, M.N., G. Giuliani, A. Maria Cremonini, P. Cenni, D. Zappi, GS Taylor, F, *CT prognostic factors in acute subdural haematomas: the value of the'worst'CT scan.* British journal of neurosurgery, 2000. **14**(2): p. 110-116.

207. Hays, A.N., C. Lazaridis, R. Neyens, J. Nicholas, S. Gay, and J.A. Chalela, *Osmotherapy: use among neurointensivists.* Neurocritical care, 2011. **14**: p. 222-228.

208. Larive, L.L., D.H. Rhoney, D. Parker, W.M. Coplin, and R. Carhuapoma, *Introducing hypertonic saline for cerebral edema: an academic center experience.* Neurocritical care, 2004. **1**: p. 435-440.

209. Shankar, A., M. Joseph, and M. Chandy, *Interhemispheric subdural hematoma: an uncommon sequel of trauma.* Neurology India, 2003. **51**(1): p. 63.

210. Wajima, D., H. Yokota, Y. Ida, and H. Nakase, *Spinal Subdural Hematoma Associated With Traumatic Intracranial Interhemispheric Subdural Hematoma—Case Report—.* Neurologia medico-chirurgica, 2012. **52**(9): p. 636-639.

211. Shima, K., T. Aruga, T. Onuma, and M. Shigemori, *JSNT-Guidelines for the management of severe head injury (Abridged edition).* Asian journal of neurosurgery, 2010. **5**(1): p. 15.

212. Tien, H.C., V. Jung, R. Pinto, T. Mainprize, D.C. Scales, and S.B. Rizoli, *Reducing time-to-treatment decreases mortality of trauma patients with acute subdural hematoma.* Annals of surgery, 2011. **253**(6): p. 1178-1183.

213. Massaro, F., M. Lanotte, G. Faccani, and C. Triolo, *One hundred and twenty-seven cases of acute subdural haematoma operated on: Correlation between CT scan findings and outcome.* Acta neurochirurgica, 1996. **138**: p. 185-191.

214. Jiang, J.-Y., W. Xu, W.-P. Li, W.-H. Xu, J. Zhang, Y.-H. Bao, Y.-H. Ying, and Q.-Z. Luo, *Efficacy of standard trauma craniectomy for refractory intracranial hypertension with severe traumatic brain injury: a multicenter, prospective, randomized controlled study.* Journal of neurotrauma, 2005. **22**(6): p. 623-628.

215. Dreier, J.P., S. Major, A. Manning, J. Woitzik, C. Drenckhahn, J. Steinbrink, C. Tolias, A.I. Oliveira-Ferreira, M. Fabricius, and J.A. Hartings, *Cortical spreading ischaemia is a novel process involved in ischaemic damage in patients with aneurysmal subarachnoid haemorrhage.* Brain, 2009. **132**(7): p. 1866-1881.

216. Laaidi, A., A. Rafiq, Y. Tahrir, S. Hilmani, and A. Lakhdar, *Contralateral epidural hematoma after decompressive surgery: Case report and systematic literature review.* Annals of Medicine and Surgery, 2022. **74**: p. 103233.

217. Fujimoto, S., H. Katsuki, M. Ohnishi, M. Takagi, T. Kume, and A. Akaike, *Plasminogen potentiates thrombin cytotoxicity and contributes to pathology of intracerebral hemorrhage in rats.* Journal of Cerebral Blood Flow & Metabolism, 2008. **28**(3): p. 506-515.

218. Gao, B.-B., A. Clermont, S. Rook, S.J. Fonda, V.J. Srinivasan, M. Wojtkowski, J.G. Fujimoto, R.L. Avery, P.G. Arrigg, and S.-E. Bursell, *Extracellular carbonic anhydrase mediates hemorrhagic retinal and cerebral vascular permeability through prekallikrein activation.* Nature medicine, 2007. **13**(2): p. 181-188.

219. Wedekind, C. and M. Lippert-Grüner, *Long-term outcome in severe traumatic brain injury is significantly influenced by brainstem involvement.* Brain Injury, 2005. **19**(9): p. 681-684.

220. Little, D., M. Kraus, J. Joseph, E. Geary, T. Susmaras, X. Zhou, N. Pliskin, and P. Gorelick, *Thalamic integrity underlies executive dysfunction in traumatic brain injury.* Neurology, 2010. **74**(7): p. 558-564.

Appendix: Publications

Peer-reviewed publications

Six publications including four first-authored publications either in preparation, under review, or accepted

Published

1. **Basilio, A.V.**, P. Xu, Y. Takahashi, T. Yanaoka, H. Sugaya, G.A. Ateshian, and B. Morrison, *Simulating cerebral edema and delayed fatality after traumatic brain injury using triphasic swelling biomechanics.* Traffic Injury Prevention, 2019. **20**(8): p. 820-825.

2. Takahashi, Y., T. Yanaoka, H. Sugaya, **A.V. Basilio**, P. Xu, G. Ateshian, and B. Morrison, *Prediction of probability of fatality due to brain injury in traffic accidents.* Traffic Injury Prevention, 2019. **20**(sup1): p. S27-S31.

3. Sundaresh, S.N., J.D. Finan, B.S. Elkin, **A.V. Basilio**, G.M. McKhann, and B. Morrison, *Region-Dependent Viscoelastic Properties of Human Brain Tissue Under Large Deformations.* Annals of Biomedical Engineering, 2022. **50**(11): p. 1452-1460.

Under Review

1. **Basilio, A. V.,** Zeng, D., Pichay, L. A., Maas, S. A., Sundaresh, S. N., Finan, J. D., Elkin, B. S., McKhann, G. M., Ateshian, G. A., Morrison III, B. (2023). Region-

dependent mechanical properties of human brain tissue under large deformations using inverse finite element modeling.

In Preparation

1. **Basilio, A. V.,** Zeng, D., Pichay, L. A., Xu, P., Maas, S. A., Ateshian, G. A., Morrison III, B. (2023). Simulating cerebral edema and ischemia after traumatic acute subdural hematoma using triphasic swelling biomechanics.

2. **Basilio, A. V.**, Zeng, D., Pichay, L. A., Hansen, O. S., Romanov, A., Gunzel, E. R., Ateshian, G. A., Morrison III, B. (2023). Fixed charge density measurements of brain tissue using confined swelling pressure methodology.

Abstracts

Three abstracts and conference proceedings including oral presentations

1. **Basilio, A. V.,** Xu P., Takahashi Y., Yanaoka, T., Sugaya, H., Ateshian, G. A., Morrison III, B., *Simulating cerebral edema and delayed fatality after traumatic brain injury using triphasic swelling biomechanics*. Enhanced Safety of Vehicles (ESV), Eindhoven, Netherlands, June 10-13, 2019.

2. **Basilio, A. V.,** Xu P., Takahashi Y., Yanaoka, T., Sugaya, H., Ateshian, G. A., Morrison III, B., *Simulating cerebral edema and delayed fatality after traumatic brain injury using triphasic swelling biomechanics*. Computer Methods in

Biomechanics and Biomedical Engineering (CMBBE), New York, New York, August 14-16, 2019.

3. **Basilio, A. V.,** Xu P., Takahashi Y., Yanaoka, T., Sugaya, H., Ateshian, G. A., Morrison III, B., *Improvements for Simulating cerebral edema and delayed fatality after traumatic brain injury using triphasic swelling biomechanics*. International Research Council on the Biomechanics of Injury (IRCOBI), Munich, Germany, 2020.